DC RESISTIVITY MODELLING AND SENSITIVITY ANALYSIS IN ANISOTROPIC MEDIA

by

Mark S. Greenhalgh
B.Sc.

Department of Physics
The University of Adelaide
SA 5005, Australia

Submitted in fulfilment of the requirements for
the degree of Doctor of Philosophy

August 2008

Chapter 1
Introduction

1.1 The Resistivity Method

1.1.1 Basic Concept and Applications

The electrical resistivity method is one of the principal electrical methods used in geophysical exploration. There are several excellent texts devoted to the subject (Keller and Frishknecht, 1966; Kunetz, 1966; Van Nostrand and Cook, 1966; Bhattacharya and Patra, 1968; Orellana, 1972; Mooney, 1980; Telford *et al.*, 1990; Nabighian, 1998). The method uses an artificial DC power source to create an electric field in the subsurface by injecting current into the ground between two metallic electrodes. By measuring and analysing the potential (voltage) response on the ground surface or underground (in boreholes or in a mine), one can obtain a resistivity distribution map of the subsurface. This map is then used with other information to help identify and delineate geological structures.

The relative simplicity of the method, the low equipment cost and ease of use combine to make electrical imaging a useful prospecting technique, and highly competitive with alternative methods like gravity and magnetics, electromagnetics, and seismic exploration. The method has proven very popular for shallow (near-surface) investigations in connection with groundwater search/hydrology (Barker and Moore, 1998; Kenna *et al.*, 2002), geotechnical appraisal/mining engineering (Panthulu *et al.*, 2001; Roth *et al.*, 2002), cavity detection (Peng and Ziaie, 1991;Van Schoor, 2002), mapping of pollution plumes (Binley *et al.*, 1997; Olivar *et al.*, 1998), environmental work (Van *et al.*, 1991; Daily and Ramirez, 1995; archaeological investigations (Arslan *et al.*, 1999; Shaaban and Shaaban; 2001), and assorted geological studies. Although there are differences in the nature of the target and its depth (which strongly affects detection and resolution capability) the resistivity method (and its close cousin, the induced polarisation method) has also found important application in coal mining and metalliferous mineral exploration.

1.1.2 Resistivities of Earth Materials

The electrical resistivity method is based on the fact that resistivities of earth materials vary widely, more than any other physical property. The range is up to 12 orders of magnitude. Resistivity depends on a number of factors: the mineralogical composition, the porosity and degree of water saturation, the salinity of the connate water, the structure and texture of the rock, as well as temperature and pressure. Apart from metallic minerals, where electronic conduction is important, ionic (electrolytic) conduction is the dominant mode of passing electricity through the ground.

Dense rocks with few voids, little moisture and negligible amounts of dissolved salts (free ions) will have high resistivity. Soft saturated clay will have a low resistivity, particularly if any decomposed organic matter or soluble salts are present. An extensive tabulation of the resistivities of earth materials is given by Parkhomenko (1967). The article by Keller (1998) also provides a comprehensive treatment on the electrical properties of rocks and minerals. Igneous rocks have high resistivity, typically above 1000 ohm-m. Sedimentary rocks like sandstone and shale have lower resistivity (100 – 200 ohm-m). Coal is an unusual material and is characterised by moderately high resistivity (300 – 600 ohm-m). Overburden materials, especially below the water table, have relatively low resistivity (e.g. 30 – 60 ohm-m). Massive sulphide ore deposits have extremely low resistivity (less than 0.01 ohm-m). Resistivity contrast and target size are the key factors which determine detectability of a target. Unless the geological unit is quite thick, comparable to the depth, it is often difficult to detect (and especially delineate) such buried resistivity anomalies from the surface. This relates to the limited depth of current penetration, and problems of electrical equivalence and suppression (see Keller and Frischknect, 1966). Basically, targets must get progressively larger with depth to see them from the surface. Often only the tops, and not the base of targets, can be delineated.

Mineralogical and geochemical changes, such as oxidation, weathering and alteration, can have a profound effect on resistivities of earth materials, as can moisture content. Oxidation and salinity lower the resistivity appreciably.

1.2. Electrical Resistivity Imaging

1.2.1. Field Procedures and Electrode Arrays

Resistivity surveying is carried out using various field procedures and electrode configurations. The reader is referred to standard textbooks for a full discussion. The basic data collection strategies involve use of four collinear electrodes (two current, two potential) which can be classified into rather standard array types, like Wenner, Schlumberger, dipole-dipole, pole-dipole etc . In *resistivity sounding*, the electrode spacing interval is changed while maintaining a fixed location for the centre of the electrode spread. Since depth of investigation increases in a general way with increasing electrode spacing, resistivity sounding is the preferred approach when we wish to learn how resistivity varies with depth. In *resistivity profiling*, the location of the spread is changed while maintaining a fixed electrode spacing interval. Since the depth of investigation will remain roughly unchanged from one reading to the next, resistivity profiling is the preferred approach when we wish to learn how resistivity varies in a horizontal direction. For example, our goal might be to locate the positions of faults, dykes, gravel deposits or ore bodies.

One extension of the profiling method is to repeat the traverse with one or more different values for the electrode spacing. A comparison of the results can provide some control over depth.

Another extension is to run profiles along parallel lines, thus providing coverage of an area rather than a line. The field quantities can then be compiled into a contour map or image.

1.2.2. Concept of Apparent Resistivity

In either procedure the idea is to convert the field measurement of voltage into a quantity called the *apparent resistivity* ρ_a which corrects for the current strength and the electrode geometry. If the earth is perfectly uniform then the apparent resistivity is equal to the true resistivity. Changes in apparent resistivity show departures of the earth from being uniform. It is a useful way to display and interpret field data.

1.2.3. Imaging and Tomography

Sounding and/or profiling was the usual way resistivity surveys were conducted up until about the early 1990s. With greater computer power made available in recent years, in combination with multi-electrode cables and computer-controlled acquisition, plus increasing interest based on geophysical inversion theory, the natural progression has been to resistivity imaging. It has involved combining sounding with profiling through use of multiple electrode data acquisition in which apparent resistivities are obtained for various electrode spacings at each horizontal location along the traverse, thus yielding a 2-D picture of vertical and horizontal resistivity variations in the subsurface. Electrical resistivity imaging (ERI) is now routinely practised. It has even been extended into areal distributions of electrodes and 3-D surveys.

A number of articles have appeared on 2-D and 3-D resistivity imaging using *surface array* scanning pole-pole, Wenner, bipole-bipole and other electrode configurations (Smith and Vozoff, 1984; Park and Van, 1991; Li and Oldenburg, 1992; Ellis and Oldenburg, 1994; Dabas *et al.*, 1994; Sasaki, 1994; Zhang *et al.*, 1995; Loke and Barker, 1995, 1996). Xu and Noel (1993) discussed some independent measurements of the surface surveys using two-, three- and four- electrode configurations for 2-D and 3-D resistivity imaging.

Crosshole DC electrical surveying, in which the source electrode (current injection point) and the potential electrode (measuring point) are placed downhole in two horizontally separated boreholes and moved over a range of depths, is able to yield detailed information on the variation of electrical conductivity between the boreholes (Daniels, 1977, 1984; Shima, 1992). Such crosshole measurements permit the detection of and delineation of interesting geological conditions between various transmitter and receiver locations. They offer potential advantages for greatly improving the effectiveness of a test boring program by locating targets more accurately. Furthermore, the downhole electric measurements greatly extend the anomaly detection capability beyond the performance limits of surface electric surveying. Owen (1983) discussed cross-hole bipole-bipole electric surveying to search for buried caves and tunnels. Daniels and Dyck (1984) demonstrated a variety of potential applications of borehole resistivity measurements to mineral exploration, but did not present any case histories as such.

In recent years, there has been great interest in developing crosshole DC electrical surveying so as to image the 2-D and 3-D structure of the earth. Crosshole resistivity imaging or tomography (Daily and Owen, 1991; Shima, 1992; Zhou and Greenhalgh, 2000) is used to reconstruct the conductivity structure of the earth using crosshole scanning and profiling data. In theory, the technique is no more than a geophysical inversion procedure with various electrode array data. With the merits of crosshole measurements, it is possible to image the targets between the boreholes.

Some rather interesting applications of crosshole electric inversion to hydrology and environmental studies have been reported by Daily and Ramiriez (1995), Slater *et al.* (1996, 2000), Spies and Ellis (1995), Middleton and Binley (2001) and Greenhalgh *et al.* (2003). For example, Daily and Ramirez (1995) used 2-D resistivity tomography to monitor in-situ remediation processes for removal of volatile organic compounds from subsurface water and soil. Five boreholes, at separations of 20 m, and extending over a depth extent of 60 m were used for the experiment. In addition they used four electrodes on the surface. Air sparging and water infiltration both changed the subsurface resistivity sufficiently to be imaged by electrical resistivity tomography. Spies and Ellis (1995) successfully employed 3-D DC crosshole tomography to monitor the melting and solidification process of an in-situ vitrification experiment with six boreholes on the circumference of a circle of radius 6.5 m. The resistivity contrast in their experiment was very high, over 1000 times.

Zhou and Greenhalgh (1999) have analysed the different effects (sensitivity patterns and anomaly amplitudes) from a variety of common electrode configurations by means of 2.5-D numerical resistivity modelling and inversion. They concluded that the bipole-bipole and pole-bipole arrays performed best. Their models included faulted and dipping conductors. The boreholes were separated by a distance comparable to the borehole depth over which "measurements" could be taken. Resolution was expected to degrade as the borehole separation increases.

1.3. Electrical Anisotropy and Its Importance

1.3.1. Micro-anisotropy and Macro-anisotropy

Apart from resistivity heterogeneity, a further complication which often arises in electrical prospecting is that of anisotropy. It refers to the situation in which the ground resistivity (or

conductivity), and hence the measured voltage (or apparent resistivity) is a function of the direction of measurement, even in homogeneous media. Such directional dependence is common in materials like shale, slate and clay which have a distinct lineation or platey fabric. It also exists in certain minerals. This is referred to as intrinsic anisotropy or microanisotropy; it depends on the crystal symmetry or texture of the material. Anisotropy may also occur on a macroscopic scale whereby a series of layers or bands of dissimilar isotropic materials behave as a single, equivalent anisotropic unit. Fracturing, jointing and rock cleavage can also produce this type of structural anisotropy, in which case the "layers" have alternating resistivities (rock and joint fill). Such pseudo-anisotropy arises when the thickness of the individual isotropic bands or units is small relative to the electrode separation used for the measurement.

1.3.2. Transversely Isotropic Materials and Magnitude of Anisotropy

In general, the resistivity must be described by a second rank tensor and the anisotropy by the tensor ellipsoid. This is described in detail in chapter 3, but for present purposes the simple model of a transversely isotropic (TI) medium will suffice. It is a very popular model in which resistivity is constant (isotropic) within a specific plane eg plane of stratification, fracture plane, but different in all other directions outside that plane. Resistivity values tend to be large (up to ten times) when measured perpendicular to this plane (referred to as the transverse resistivity ρ_t) compared to values parallel to the plane (referred to as the longitudinal resistivity ρ_l). The converse holds for the reciprocal quantity, electrical conductivity. It is often a maximum parallel to the foliation or fracturing and a minimum in the transverse direction, because of the presence of water and dissolved salts (or the preferred mineral alignment) along the plane, where permeability is greater.

For the TI medium the average resistivity (geometric mean) can be defined as $\rho_m = \sqrt{\rho_t \rho_l}$ and the coefficient of anisotropy as $\lambda = \sqrt{\rho_t / \rho_l}$. Typical values of λ for shales and slates are 1.2 to 3 (see Parkhomenko, 1967; Keller and Frischknecht, 1966). Shale and sandstone interbeds have values in the range 1.05 –1.15, while interbedded anhydrite and shale have reported values of 4.0–7.5. Even alluvium may have anisotropy factors of 1.02-1.1. Igneous and metamorphic rocks can also have significant anisotropy (Hill, 1972, Asten, 1974).

1.3.3. Effects of Anisotropy on Field Measurements

If anisotropy exists in the ground but is ignored, then the true ground resistivities and the geologic structure that are interpreted from measured apparent resistivity may be incorrect. Papers which deal with the effects of anisotropy on surface resistivity measurements include Habberjam (1972, 1975), Matias and Habberjam (1986) and Matias (2002). The borehole resistivity measurment problem has been considered by Kunz and Noran (1958), Asten (1974) and Moran and Gianzero (1979).

When the axis of symmetry of the TI medium is vertical, such as for horizontal bedding, then for normal resistivity surveys carried out at the surface, there is no way to tell the difference between resistivity measured vertically and resistivity measured horizontally. The measurement is invariant in all horizontal directions. Such anisotropy is therefore undetectable at the surface. If such anisotropy exists, depth estimates will be in error by a factor of λ. This follows from the Principle of Equivalence. It can be illustrated as follows. Consider current flow in the longitudinal direction in an anisotropic layer of thickness *h*, and of unit length in the two perpendicular directions. The longitudinal conductance *s* (inverse of resistance $R = \rho_l l / A$ where *l* is the length and A = cross sectional area; here *l* = 1 and A = h.1) is given by $s = h.1/\rho_l = \lambda h/\rho_m$. Now consider current flow in the transverse direction across the layer. In this case A = 1.1 and *l* = h, so transverse resistance is $t = \rho_t.h/1.1. = \lambda h \rho_m$. Therefore an anisotropic layer of thickness *h* and having resistivities ρ_t and ρ_l will be indistinguishable from an isotropic layer of thickness λ*h* and resistivity ρ_m.

As stated earlier, a sequence of thin isotropic layers can appear as a single macro-anisotropic layer. The effective longitudinal resistivity of the sequence is obtained by considering it to behave like a parallel resistor network, in which current can distribute itself through the layers and each layer can be replaced by the resistor $R_i = \rho_i.1/h_i.1 = \rho_i/h_i = 1/s_i$. The equivalent total resistance is therefore given by:

$$R_{eq} = 1/\sum s_i = \rho_l.l/A = \rho_l 1/\sum h_i$$

yielding an effective longitudinal resistivity:

$$\rho_l = \sum h_i / \sum s_i \text{ , where } s_i = h_i / \rho_i \text{ .} \qquad (1.1)$$

Now consider current flow in the transverse direction through the layer stack, which behaves like a series resistor network in which each layer can be replaced by its resistance $R_i = \rho_i l / A = \rho_i h_i / 1.1 = t_i$. The total equivalent resistance is:

$$R_{eq} = \sum t_i = \rho_t l / A = \rho_t . (\sum h_i) / 1.1. = \rho_t \sum h_i \text{ ,}$$

yielding an effective transverse resistivity:

$$\rho_t = \sum t_i / \sum h_i \text{ , where } t_i = \rho_i h_i \text{ .} \qquad (1.2)$$

For example, a sequence of 20 layers each 2 metres thick, alternating in resistivity from 5 to 100 ohm-m, has the following effective parameters: $\rho_l = 9.7$; $\rho_t = 52.5$; $\rho_m = 22.6 \Omega m$; λ =2.32; h = 92.8 m. It follows that errors in interpreted depths can be appreciable; the true depth in this example is 40 metres, while the apparent depth is 92.8 m.

Let us now turn to the situation where the axis of symmetry of the TI medium is almost horizontal, e.g. steeply dipping beds or fractures. In this case the resistivity measured with electrodes oriented in one direction will be different to that measured using the same electrode array oriented in a different direction. As shown in chapter 3, the apparent resistivity measured for steeply dipping beds (if there is no overburden) is counter intuitive. One might expect that the measured resistivity (like the true resistivity) would be lowest parallel to strike since current tends to flow along paths of least resistance. In fact, the measured resistivity is higher along strike because of increased current density parallel to the survey line (apparent resistivity calculations assume uniform current density in three directions). When current density is higher than it would be in a uniform isotropic ground the measured potential difference is higher for the given current source, resulting in higher apparent resistivity. In fact, the apparent resistivity is equal to ρ_m, as shown mathematically in section 3.4.2. Conversely, the apparent resistivity measured perpendicular to strike is not equal to the transverse resistivity ρ_t at all, but takes on its minimum value and is equal to that of the true

longitudinal resistivity (see section 3.4.2). This is referred to as the Paradox of Anisotropy (see Maillet, 1947; Keller and Frischknecht, 1966; Bhattaycharia and Patra, 1968).

1.3.4. Detecting Anisotropy

Two principal field techniques have been advocated to detect and characterise electrical anisotropy: (1) azimuthal resitivity measurements in which linear arrays of electrodes are used to measure apparent resistivity in a variety of directions, say every ten degrees (Taylor and Fleming, 1988, Ritzi and Andolsek,1992, Busby, 2000), and (2) square array techniques pioneered by Habberjam and co-workers (Habberjam and Watkins, 1967; Habberjam, 1972 ;1975; Matias and Habberjam, 1986). The square array is claimed to offer greater sensitivity over standard co-linear arrays, because three sets of measurements are made in different direction at each point (along the diagonal of the square as well as along the two orthogonal sides). This technique has been further developed in recent years by Matia (2002). Watson and Barker (1999) advocated that with the offset Wenner system it is possible to distinguish anisostropy from dipping layers and lateral changes in resistivity, which can influence the square array measurements. They caution that many of the reported cases of anisotropy in the literature have most likely been misinterpreted.

Numerous resistivity field studies have been performed linking electrical anisotropy with fractures, joints and other features. For example, in England Nunn *et al.* (1983) measured the fracture anisotropy in chalk while Busby and Jackson (2006) used time lapse measurements for the prediction of coastal cliff failure. In the USA surveys have been reported by Ritzi and Andolsek (1992), Wishart (2006), among others, for hydrological assessment. Electrical characterisation of jointed and faulted systems by azimuthal anisotropy have also been published for Australia (Wilson *et al.*, 2001), Germany (Hagrey, 1994), and France (Nguyen *et al.*, 2007). Electrical anisotropy is also important in crustal MT studies (Wannamaker, 2005; Hamilton *et al.*, 2006) and in shallow EM investigations (Slater *et al.*, 1998; Linde and Pederson, 2004).

Anisotropy can be more readily detected using cross-hole and borehole-to-surface techniques than with simple surface measurements, especially when the axis of symmetry is sub-vertical. The emerging trend is for tensor measurements, in which the impressed electric field (from the current electrodes) is sequentially applied in two orthogonal directions, and the voltage measurements made on two orthogonal sets of potential electrodes.

1.4 Resistivity Modelling

Resistivity modelling refers to the process of calculating, usually by some numerical technique, the theoretical electric response of the earth for a given situation (conductivity model) and particular electrode configuration. It is an indispensable aid to interpretation, and an essential part of resistivity inversion. For the latter, one attempts to obtain the conductivity distribution by fitting the observed data to a suitable theoretical model. This generally involves iterative model adjustment and forward computations until the misfit is reduced to some acceptable error tolerance, subject to certain regularisation procedure, often involving smoothing, damping and constraints. An essential part of inversion is choosing the appropriate degree of model complexity. For many years one-dimensional conductivity distributions (layered earth models) were about as sophisticated as one could get. These days two-dimensional models, in which the conductivity can vary in two spatial directions, and even three-dimensional models, are commonplace. The various modelling procedures, which include boundary integral, finite difference and finite element, will be reviewed in sections 2.4 and 2.5.

The interpretation of anisotropic resistivity data is still problematic. It is often only semi-quantitative, principally to delineate fracture and joint orientation. Very few researchers have developed resistivity imaging and inversion codes to quantitatively handle anisotropic situations. The computer programs that have been developed (Pain *et al.*, 2003; LaBreque *et al.*, 2004; Herwanger *et al.*, 2004 and Kim *et al.*, 2006) are largely based on simplified forms of the conductivity tensor. Part of the problem is that the mathematical problem is quite complex. There are very few analytic solutions available for resistivity problems and then only for the simplest of situations, like a half-space. Even idealised models like spheres, cylinders, and cuboids embedded in a half space do not lend themselves to easy theoretical analysis, especially if the background medium is anisotropic.

Apart from its utility in resistivity interpretation, forward modelling is a very useful aid to survey design, to know what type of electric response to expect and which electrode geometry is likely to perform best. Modelling also helps to understand questions of detection and resolution, whether certain targets can be delineated, and what the likely anomaly effect is. It is also an integral part of sensitivity analysis, so important in any geophysical inversion. This will be taken up in chapter 6.

1.5 Thesis Objectives

The main objective of this thesis research was to develop a new numerical technique for 2.5-D / 3-D DC resistivity modelling in heterogeneous, anisotropic media having arbitrary surface topography. Most of the available algorithms (finite difference, finite element) do not incorporate anisotropy and have difficulty handling irregular surface topography. The new method, based on Gaussian quadrature grids, is particularly well designed for handling the above-mentioned complexities. It differs from the spectral method, popular in areas like hydrodynamics, but retains all the main advantages of the advanced numerical method. The new Gaussian Quadrature Grid (GQG) method could be considered as a modified version of the spectral element method in which we discretize the model domain with the Gaussian quadrature abscissae rather than the constant elements, then employ local cardinal functions to calculate the unknown potentials values and their gradients at the abscissae. Like the standard FE method and the spectral element method, it leads to a sparse and symmetric linear equation system to solve. The main advantages of the new method are no requirements of the element mesh matching the surface topography, nor for an element integration so that it makes complex forward modelling much easier.

The subsidiary aims of the thesis are to make use of the new modelling program to better understand effects of anisotropy on resistivity measurements, and to develop expressions for the Fréchet derivatives (sensitivity functions) in 3-D heterogeneous, anisotropic media. The special case of a homogeneous tilted transversely isotropic medium is investigated in some detail, to see how the various derivatives differ from each other and from the isotropic case.

The thesis also sets out to analyse the properties of the resistivity tensor and how the various elements relate to the principal values and the angles defining the axis of symmetry. Explicit expressions are developed for the derivatives of the tensor elements with respect to the principal values, which lie at the heart of the sensitivity equations.

Chapter 2
Resistivity Modelling: Theory and Previous Approaches

2.1. Basic Electromagnetic Theory

Electromagnetic theory, on which the electrical and electromagnetic (EM) methods of exploration are based, is treated in many physics books, at all levels. The texts by Smythe (1950) and Stratton (1941) are classics and will suffice for our purposes. Here I give only the briefest of treatments. The purpose is to show the special form of Maxwell's equations in the DC case, and to introduce the idea of electric potential and to review Ohm's Law and the Equation of Continuity. These two equations, together with the boundary conditions for the electric field, are the basis for solving for current flow (and electric potential) in arbitrary media.

2.1.1 Maxwell's Equations and the Electrical Properties of Matter

The following quantities describe the bulk electrical properties of a medium in which we wish to measure the electromagnetic field:

$\varepsilon =$ permittivity (or dielectric constant $\kappa = \varepsilon / \varepsilon_0$, where ε_0 is the free space value)

$\mu =$ magnetic permeability

$\sigma =$ electrical conductivity (or its reciprocal resistivity $\rho = 1/\sigma$)

In a uniform medium, these quantities are scalar constants. In an isotropic but inhomogeneous medium, they are scalar functions of position. In anisotropic media, they are second rank tensors.

The electric and magnetic fields in the medium, which are often the quantities we wish to compute, may be described by:

$\vec{E} =$ electric field intensity [V.m^{-1}]

$\vec{B} =$ magnetic induction [W.m^{-2}]

$\vec{D} =$ electric displacement [C.m^{-2}]

$\vec{H} =$ magnetic field intensity [A-turn.m^{-1}]

These vector quantities are related to

$\rho =$ electric charge density [C.m^{-3}] , and

$\vec{J} =$ electric current density [A.m^{-2}]

through the four Maxwell Equations

$$\vec{\nabla} \times \vec{E} + \partial \vec{B} / \partial t = 0 \qquad \text{(Faraday's law)} \qquad (2.1)$$

$$\vec{\nabla} \times \vec{H} - \partial D / \partial t = \vec{J} \qquad \text{(Ampere's Law)} \qquad (2.2)$$

$$\vec{\nabla} \cdot \vec{B} = 0 \qquad \text{(Solenoidal property of B)} \qquad (2.3)$$

$$\vec{\nabla} \cdot \vec{D} = \rho \qquad \text{(Coulomb's Law)} \qquad (2.4)$$

These are fundamental equations which show the inter-dependence of the field quantities $\vec{D}, \vec{E}, \vec{B}$ and $\vec{H}$. They do not directly yield expressions for these quantities, although they permit the computation of one from the other. Most texts on electromagnetic theory say more or less about the derivation of these equations.

An auxiliary equation, which may be derived from Maxwell's equations, is the Equation of Continuity, which along with Ohm's Law, is the theoretical basis for DC resistivity prospecting:

$$\vec{\nabla} \cdot \vec{J} + \partial \rho / \partial t = 0 \qquad (2.5)$$

It is a statement of conservation of charge and says that away from sources, the current density is divergence free $\left(\nabla \cdot \vec{J} = 0\right)$.

2.1.2 Measurable Quantities and Boundary Conditions

The measurable EM quantities in physics/geophysics are:

1. Total current flow through a cross –sectional area A:

$$I = \left(\left| \vec{J} \right| + \left| \partial \vec{D} / \partial t \right| \right) \cdot A$$

The second term is Maxwell's displacement current and for DC: $\partial \vec{D} / \partial t \to 0$

2. Voltage developed between two points A and B

$$V = \int_{A}^{B} \vec{E} \cdot d\vec{l}$$

3. Magnetic field intensity $\left| \vec{H} \right|$.

Boundary conditions are also required in solving problems in electromagnetism. They serve to connect the EM field quantities from one region to another. The four boundary conditions can be stated as follows:

1. The tangential component of $\vec{E}$ is continuous
2. The normal component of $\vec{B}$ is continuous
3. The normal component of $\vec{D}$ differs across the boundary by the density of surface charge ω.
4. The tangential component of $\vec{H}$ differs across the boundary by the density of surface current $\vec{K}$.

The surface current density $\vec{K}$ is only required for very good conductors, and it may normally be ignored. In that case, tangential $\vec{H}$ is continuous.

2.1.3 Electric Potential and Ohm's Law

The resistivity method operates in the absence of a field of induction and is based on observations of an electric field maintained by direct current. This means that we may set all time dependence equal to zero, except that we permit stationary currents to exist. We are now

considering electric and magnetic fields associated with stationary (DC) currents; the two fields are decoupled and we may consider either one independently. Equations (2.1) and (2.2) become:

$$\nabla \times \vec{E} = 0 , \qquad \nabla \times \vec{B} = 0 \tag{2.6}$$

It is the electric field which is important in the resistivity method. We do not consider the magnetic field associated with the stationary current flow. The zero curl (irrotational) property specified by equation (2.6) shows that the electric field $\vec{E}$ is conservative and so it can be expressed as the gradient of a scalar potential *U*, i.e.

$$\vec{E} = -\vec{\nabla} U \tag{2.7}$$

Ohm's Law provides the connection between current density $\vec{J}$ and the electric field $\vec{E}$:

$$J_i = \sigma_{ij} E_j \qquad i, j = x, y, z \tag{2.8}$$

where σ is the conductivity described by a 2nd rank tensor (see chapter 3). Summation is implied in the above equation through repetition of subscript *j*, so that each component of the current density is a linear combination of each component of the electric field. Similar linear equations exist linking the other field quantities:

$$\begin{aligned} D_i &= \varepsilon_{ij} E_j \\ B_i &= \mu_{ij} H_j \end{aligned} \tag{2.9}$$

For isotropic media, the medium properties are defined simply as the ratios of the magnitudes of the various field quantities:

$$\varepsilon = D/E , \quad \mu = B/H , \quad \sigma = J/E \tag{2.10}$$

2.1.4 The 3-D Poisson Equation for Electric Potential

Combining equations (2.5), (2.7) and (2.8) results in the differential equation:

$$\vec{\nabla} \cdot \sigma_{ij} \vec{\nabla} U = I\delta\left(\vec{r} - \vec{r}_s\right) \quad \vec{r}, \vec{r}_s \in \Omega \tag{2.13}$$

where we have made the replacement from equation (2.5) that the current strength $I = \frac{\partial \rho}{\partial t}$. Here $\vec{r}_s = \left(x_s, y_s, z_s\right)$ is the location of the current electrode in Ω. Equation (2.13) involves a dyadic product (see Appendix A) between the conductivity tensor and the gradient of the potential. Or stated another way in this particular case, we form the matrix product between the 3x3 conductivity matrix and the 3x1 electric field vector , and then take the divergence of the resulting 3x1 vector (current density).

Within uniform and isotropic sub-volumes of the medium we see that the above equation can be written as:

$$\vec{\nabla}^2 U = \frac{I}{\sigma}\delta(\vec{r} - \vec{r}_s) \tag{2.14}$$

which is recognised as the more usual (simplified version) form of Poisson's equation. Away from sources $(\vec{r} \neq \vec{r}_s)$ the equation reduces to Laplace's equation:

$$\nabla^2 U = 0\,. \tag{2.15}$$

Analytic solutions to equation (2.13) may be developed for a particular model by selecting a coordinate system to match the geometry and imposing appropriate boundary conditions. The basic solution of equation (2.13) for a uniform, isotropic full-space medium ($\sigma =$ constant) has the simple expression:

$$U\left(r_s, r\right) = \frac{I}{4\pi\left|r - r_s\right|}\,. \tag{2.16}$$

In a half space with the current source at the surface we simply replace the "4π" factor in the above equation by "2π" since the current flows radially out through a hemispherical surface and not a full sphere. For more complicated media (variable conductivity), one has to solve equation (2.13) in conjunction with the boundary conditions by some numerical method. The *boundary conditions* in the DC case reduce to:

(1) continuity of voltage across the interface,
(2) continuity of the normal component of current density across the interface.

Obviously, at the Earth's free surface, the latter condition leads to zero component of current density at the surface (current flow is entirely tangential). From Ohm's Law, this is equivalent to requiring that the normal derivative of the potential is zero (Neumann condition). There is also the radiation condition that at infinity the potential is zero (Dirichlet condition).

2.2. The 2.5-D Approximation

In many geophysical applications the 2.5-D approximation is the natural treatment. It refers to the situation in which the current electrode is assumed to be a point-source, and the conductivity σ model is considered to be 2-D, that is, the variation of the conductivity depends upon only the x- and z- coordinates: $\sigma_{ij} = \sigma_{ij}(x,z)$ in equation (2.13). To remove the y-coordinate, we set the source at $(x_s, 0, z_s)$ and take the Fourier-cosine transform with respect to the y-coordinate, which transforms equation (2.13) into:

$$\vec{\nabla}\cdot\sigma_{ij}\vec{\nabla}\bar{U} - k_y^2\sigma_{ij}\bar{U} = -\frac{I}{2}\delta(\vec{x}-\vec{x}_s)\delta(\vec{z}-\vec{z}_s) \quad (x,x_s),(z,z_s)\in\Omega \tag{2.17}$$

where we use $\nabla = (\partial_x, \partial_z)$ for the 2-D gradient in the (x,z) plane and

$$\bar{U}(x,z,k_y) = \int_0^\infty U(x,y,z)\cos(k_y y)\,dy\,. \tag{2.18}$$

2.2.1 Helmholtz Equation

Inspecting equation (2.17), it is recognised to be the Helmholtz equation. In its more general form, applicable to electromagnetic or seismic wave propagation, it is given by:

$$\nabla\cdot\left[a\left(x,z\right)\nabla\bar{\Phi}\right]+k_a^2\left(a\left(x,z\right),b\left(x,z\right),k_y\right)\bar{\Phi}=0, \qquad (2.19)$$

where $\nabla=\left(\partial_x,\partial_z\right)$, $\bar{\Phi}$ is the Fourier cosine transform of Φ (the 3-D physical field, i.e. electric potential) and $a\left(x,z\right)$ and $b\left(x,z\right)$ are two arbitrary model functions that represent the physical properties of the medium defined in the $\left(x,z\right)$-plane, e.g. the electrical conductivity $\sigma\left(x,z\right)$.

The quantity k_y is the y component of the 3-D wavenumber, and k_a may be called the apparent wavenumber in the $\left(x,z\right)$ plane. The apparent wavenumber is generally a function of the model parameters $a\left(x,z\right)$, $b\left(x,z\right)$ and wavenumber k_y. Obviously, equation (2.19) is a general form of the ordinary Helmholtz equation and it arises from the 2.5-D approximation. So, we call it the 2.5-D Helmholtz equation with which the following problem may be defined when including a point-source and a mixed boundary condition:

$$\begin{cases}\nabla\cdot\left[a\nabla\bar{\Phi}\right]+k_a^2\left(a,b,k_y\right)\bar{\Phi}=-\dfrac{S}{2}\delta\left(x-x_s\right)\delta\left(z-z_s\right), & x,z\in\Omega\\ \dfrac{\partial\bar{\Phi}}{\partial\vec{n}}+B\bar{\Phi}=0 & x,z\in\Gamma\end{cases} \qquad (2.20)$$

Here S is the magnitude of the source located at the point $\left(x_s,0,z_s\right)$, the factor $1/2$ comes from the Fourier-cosine transform of $\delta\left(y-0\right)$, B is a boundary operator and $\vec{n}$ is the unit normal vector for the boundary Γ enclosing Ω. It can be seen that the Helmholtz equation (2.20) represents the DC electric potential field. The forward problem of modelling, entails solving equation (2.20) for the physical quantity $\bar{\Phi}$ at some specified spatial positions, with given model parameters $a\left(x,z\right)$ and $b\left(x,z\right)$. From equation (2.18), the spectrum $\bar{U}\left(x,z,k_y\right)$ is the wavenumber domain form of the 3-D electric potential and is a real valued function.

Then equation (2.17) becomes the governing equation for the DC electric potential computation with the 2.5-D approximation. Comparing with equation (2.20), it is obviously the specified form of the 2.5-D Helmholtz equation with ($a = \sigma_{ij}(x,z)$, $b =$ constant, $k_a^2 = -k_y^2\sigma_{ij}(x,z)$ and S = I).

In numerical simulations, only a limited computational range Ω is employed so that some artificial boundary condition must be introduced in the modelling. In general, the boundary condition may be expressed by a mixed-boundary condition that includes Dirichlet and Neumann boundary conditions. So, the defined partial differential equation problem for DC resistivity measurements becomes:

$$\begin{cases} \vec{\nabla}\cdot\sigma_{ij}\vec{\nabla}\bar{U} - k_y^2\sigma_{ij}\bar{U} = -\dfrac{I}{2}\delta(\vec{x}-\vec{x}_s)\delta(\vec{z}-\vec{z}_s) & (x,x_s),(z,z_s)\in\Omega \\ \dfrac{\partial\bar{U}}{\partial n} + B\bar{U} = 0 & (x,z)\in\partial\Omega \end{cases} \tag{2.21}$$

where the boundary operator B will be given later in chapter 4.

2.2.2 The 2.5-D and 3-D Green's Functions

The 2.5-D Helmholtz equation Green's function allows us to skip the consideration of the source properties, e.g. current magnitude I. It is the potential resulting from a delta function current source of unit amplitude. In following chapters it is the basic quantity for calculating the synthetic data in modelling, and evaluating the Fréchet and second derivatives. The 2.5-D Green's functions may be defined by

$$\bar{G}^{2.5D}(x,k_y,z) = 2\int_0^\infty G^{3D}(x,y,z)\cos(k_y y)\,dy \tag{2.22}$$

where $G(x,y,z)$ is the 3-D Green's functions for the DC electric potential field. The factor 2 is to remove the ½ factor resulting from the Fourier-cosine transform of $\delta(y-0)$. Obviously, the Green's functions satisfy the DC resistivity equation:

$$\begin{cases} \vec{\nabla}\cdot\sigma_{ij}\vec{\nabla}\bar{G}^{2.5D} - k_y^2\sigma_{ij}\bar{G}^{2.5D} = \delta\left(\vec{x}-\vec{x}_s\right)\delta\left(\vec{z}-\vec{z}_s\right) & \left(x,x_s\right),\left(z,z_s\right)\in\Omega \\ \dfrac{\partial\bar{G}^{2.5D}}{\partial n} + B\bar{G}^{2.5D} = 0 & \left(x,z\right)\in\Gamma \end{cases} \tag{2.23}$$

According to the definitions, when $k_y = 0$ the Green's function reduces to the 2-D one (response of a line source). Comparing equation (2.19) with (2.17), the general 2.5-D response to a point source S = I can be obtained by convolution, or frequency domain multiplication, using the relation:

$$U\left(x,y,z\right) = \frac{I}{2}\cdot F_c^{-1}\left\{\bar{G}^{2.5D}\left(x,k_y,z\right)\right\} \tag{2.24}$$

In the 3-D case:

$$U(x,y,z) = I.G^{3D}(x,y,z) \tag{2.25}$$

where G^{3D} now satisfies the Poisson equation:

$$\vec{\nabla}.\sigma_{ij}\vec{\nabla}G = \delta(r-r_s) \tag{2.26}$$

2.2.3. Reciprocity

An important property of the 2.5-D Green's functions is that of reciprocity:

$$G^{2.5D}\left(k_y,r_s,r_p\right) = G^{2.5D}\left(k_y,r_p,r_s\right) \tag{2.27}$$

where r_s and r_p represent the positions of the current source and potential electrode. This equation states that the equivalent values of the 2.5-D Green's function can be obtained by exchange of the positions of source and receiver. The same holds true for the 3D Green's functions. From equations (2.24) and (2.25), it also follows that the electric potential *U* exhibits the reciprocity property:

$$U\left(r_s,r_p\right) = U\left(r_p,r_s\right) \tag{2.28}$$

Thus identical voltage measurements will be obtained if current and potential electrodes are interchanged in an arbitrary medium.

2.3 Numerical Forward Modelling Approaches

It has been shown that the DC electrical resistivity model may be reduced to a boundary value problem of the 3-D Poisson equation (2.13) or the 2.5-D Helmholtz equation (2.17). To solve the defined partial differential equation for an arbitrary medium, some numerical technique must be employed.

There are three principal techniques of DC resistivity modelling which have been reported in the literature: finite-difference methods (FDM), finite element methods (FEM) and integral equation methods. Each technique has its own advantages and is specifically suitable for some model geometries. In this section we will briefly review the different approaches.

2.3.1 Finite Difference and Finite Element Methods

The FDM applies difference operators to approximate the vector calculus gradient and divergence operators in the governing equation (Mufti 1976; Dey and Morrison 1979a, 1979b; Mundry 1984; James 1985; Spitzer 1995). The FEM converts the partial differential equations into integral equations by a Variational Principle or Galerkin method, then carries out a numerical integration (Coggon 1971; Fox *et al.* 1980; Pridmore *et al.* 1981; Holcombe and Jirack 1984; Querlat *et al.* 1991; Zhou and Greenhalgh 2001).

In many applications of 2-D or 3-D resistivity imaging, we often encounter a geological model that has a complex topography, such as small cliffs, steep hills and large trenches. Such natural conditions pose a difficulty for numerical modelling with the FD method. To deal with these cases, most researchers prefer the FEM in which some powerful 2-D/3-D grid generators, such as TetGen (3-D) and Delaunay Triangulator (2-D), are applied to the finite element mesh which fit the complex topography (Loke 2000; Shewchuk 2002; Rucker *et al.* 2005; Kerry & Weiss 2006). However, employing such grid generators, one hardly in advance knows where the grid nodes are and it results in an irregular parameterization for forward modelling and inversion. We desire to develop a new numerical method that can handle a complex topography without the grid generator and control the node distribution of

model parameterization in forward modelling and inversion, as well as being suitable for the anisotropic model when thin layered, fractured or cleaved rocks are present.

Both the FDM and the FEM improve accuracy by employing dense nodes of the mesh (especially near the current sources where potential varies rapidly) or by decreasing the size of the element. Singularity removal techniques (Lowry *et al.* 1989; Zhao and Yedlin 1996) have been developed to overcome numerical problems at the source, and infinite element methods (Blome and Maurer 2007) have been introduced as a means of overcoming limitations of artificial boundary conditions (combined Neumann and Dirichlet condition, see Dey and Morrison 1979a,b) under the earth.

2.3.2. Boundary Integral Methods

The integral equation methods (Dieter *et al.*, 1969; Lee, 1975; Snyder, 1976; Okabe, 1981; Das and Paransis, 1987; Xu *et al.*, 1988) are based on the integral form of solution of the DC resistivity problem (directly using the Green's function of a uniform medium). They are sometimes referred to as boundary element methods (BEM) and deal well with complex topography. Such methods are particularly suitable for simple model geometries such as several homogeneous sub-regions. They have been typically applied to the problem of embedded regular shaped bodies in an otherwise homogeneous or layered half space. The main advantage is the lower cost of computer resources than for other methods in computing the 3-D potential response. However the BEM is not well suited for modelling of arbitrary media. A comprehensive treatment of integral equation methods as applied to the geoelectric problem is given in the book by Eskola (1992).

2.4 Solutions for Anisotropic Models

Few researchers have incorporated anisotropy into the numerical modelling (Yin and Wiedelt, 1999; Pain *et al.*, 2005; Li and Spitzer, 2005; Pervago *et al.*, 2006; Kim *et al.*, 2006; LaBrecque *et al.* 2004). As shown earlier, it involves a dyadic product (see appendix A) between the conductivity tensor and the gradient of the potential (or Green's function). Most treatments have been based on a finite element solution to the partial differential equation. The integral equation approach was used by Pal and Dasgupta (1984) who studied the electric potential due to a surface point source over an inhomogeneous anisotropic half-space of the simple vertical transversely isotropic (VTI) type. An extension of this was made by Pal and

Mukherjee (1986) who dealt with a layered conducting earth with dipping anisotropy. Eloranta (1988) modelled mise a la masse anomalies in a TI medium containing prismatic conductors, while Eskola and Hongisto (1997) considered an anisotropic body located in an isotropic environment. Flykt *et al.* (1996) calculated the potential anomalies caused by a conducting body in an anisotropic conducting half-space. Li and Uren (1997a,b) gave analytic solutions for the point source potential in an anisotropic 3-D half space, comprising either two horizontal layers or two vertical boundary planes. In another paper (Li and Uren, 1998) they applied image theory to derive the solution for the potential from a buried current source in an arbitrary anisotropic half space, and showed how the image source is laterally displaced from the true source horizontal position. Li and Stagnitti (2000) studied the problem of direct current electric potential in an anisotropic half-space with a vertical contact and containing a conductive 3D body.

Chapter 3
Anisotropy and the Electrical Conductivity Tensor

3.1 The Conductivity Tensor

The conductivity tensor $\boldsymbol{\sigma}$, which relates the current density $\vec{J}$ to the electric field $\vec{E}$ through the Ohm's law relation (section 2.1.3):

$$J_i = \sigma_{ij} E_j \qquad i, j = x, y, z \tag{3.1}$$

is of rank 2, and for the most general anisotropic medium can be described by 6 independent components. (See Appendix A for a more detailed overview). Writing it out as a 3 x 3 symmetric matrix in the cartesian co-ordinate or recording frame, we have:

$$\boldsymbol{\sigma} = \begin{pmatrix} \sigma_{xx} & \sigma_{xy} & \sigma_{xz} \\ \sigma_{xy} & \sigma_{yy} & \sigma_{yz} \\ \sigma_{xz} & \sigma_{yz} & \sigma_{zz} \end{pmatrix} \tag{3.2}$$

The matrix can be diagonalised to produce the three eigenvalues $\sigma_1, \sigma_2, \sigma_3$ which yield the principal conductivities in the directions of the three principal axes (or eigenvectors $\hat{x}, \hat{y}, \hat{z}$).

$$\boldsymbol{\sigma}' = \begin{pmatrix} \sigma_{x'x'} & 0 & 0 \\ 0 & \sigma_{y'y'} & 0 \\ 0 & 0 & \sigma_{z'z'} \end{pmatrix} = \begin{pmatrix} \sigma_1 & 0 & 0 \\ 0 & \sigma_2 & 0 \\ 0 & 0 & \sigma_3 \end{pmatrix} \tag{3.3}$$

These orthogonal directions refer to the natural frame of the rock and reflect symmetry axes or the actual rock structure/fabric. In these directions, $\vec{J}$ is parallel to $\vec{E}$, but for all other directions, the current density and electric field are in different directions to each other. The three Euler angles, which permit a rotation from the Cartesian frame into the principal directions, together with the three eigenvalues, constitute an alternative set of the six independent components of the tensor to those given in equation (3.2).

3.2 The Representation Quadric and Tensor

For second rank symmetric tensors like the conductivity tensor, there is a simple geometrical representation referred to as the representation quadric:

$$\sigma_{ij} x_i x_j = 1 \tag{3.4}$$

or expanding out into the various components:

$$\sigma_{xx} x^2 + \sigma_{yy} y^2 + \sigma_{zz} z^2 + 2\sigma_{xy} xy + 2\sigma_{xz} xz + 2\sigma_{yz} yz = 1 \tag{3.5}$$

This is the equation of an ellipsoid, centred at the origin, in the Cartesian co-ordinate frame. The axes of the ellipsoid are tilted in the directions of the principal directions mentioned above (see Fig 3.1a). By a co-ordinate rotation, the cross terms (or off-diagonal elements) in the above equation are eliminated, yielding, in the natural rock frame x', y', z':

$$\sigma_1 (x')^2 + \sigma_2 (y')^2 + \sigma_3 (z')^2 = 1 \tag{3.6}$$

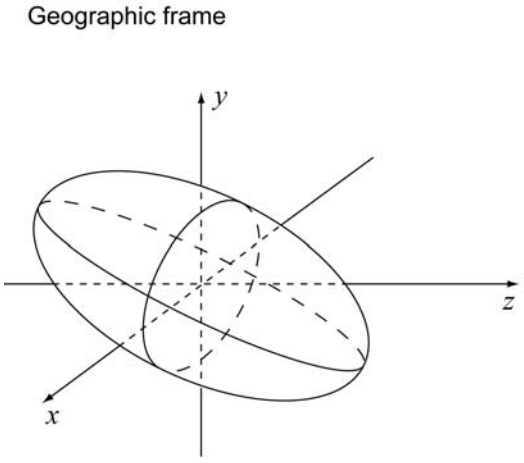

Fig. 3.1a The conductivity tensor ellipsoid in the geographic co-ordinate frame x,y,z.

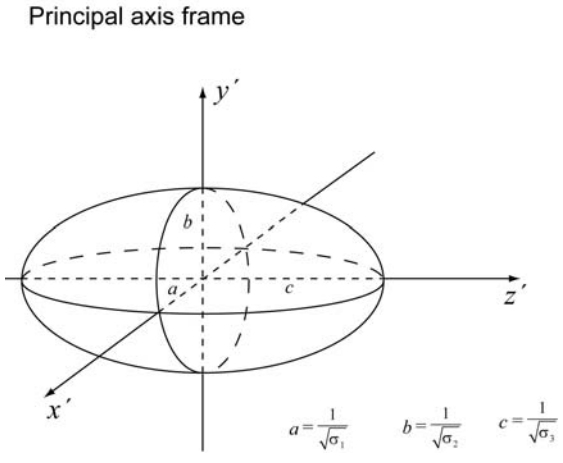

Fig. 3.1b The conductivity tensor ellipsoid in the principal axis frame (or natural rock frame) x',y',z'

The semi –major axis lengths of the ellipsoid are equal to the inverse of the square roots of the eigenvalues or principal conductivities (see Fig 3.1b). If we choose to work with the

resistivity tensor, $\boldsymbol{\rho} = \boldsymbol{\sigma}^{-1}$, then the semi-axes are equal in length to the square roots of the principal resistivities: $\rho_1 = 1/\sigma_1, \quad \rho_2 = 1/\sigma_2, \quad \rho_3 = 1/\sigma_3$.

For an electric field oriented in an arbitrary direction $\hat{n}$ from the centre of the ellipsoid to the surface of the ellipsoid, the radius *r* (or distance along this line) gives the square root of the resistivity in that direction (see Fig 3.2). The normal to the tangent at P gives the direction of the current density vector (Fig 3.2). Obviously, for an isotropic medium the ellipsoid reduces to a sphere and the radius is normal to the surface, so that $\vec{J}$ is parallel to $\vec{E}$. The current density in the direction $\hat{n}$ of the electric field is given by

$$J_n = \vec{J} \cdot \hat{n} = \sigma_n E = E/r^2 \tag{3.7}$$

with $E = \left|\vec{E}\right|$, r is distance from the centre of the ellipsoid to the point on its surface intersected by the electric field $\vec{E}$ and σ_n is the conductivity in direction $\hat{n}$, given by:

$$\sigma_n = \sigma_{ij} n_i n_j \tag{3.8}$$

Summation is implied by the repeated subscripts and the unit vector is determined by $\vec{n} = \vec{E}/E$.

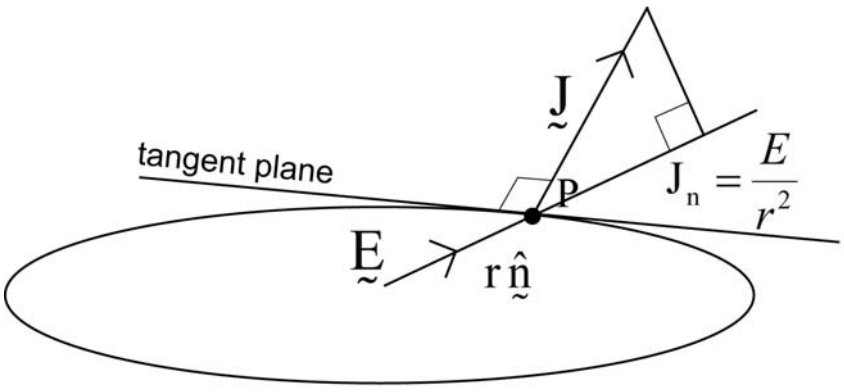

Fig. 3.2 The relationship between the electric field vector $\underset{\sim}{E}$ and the current density vector $\underset{\sim}{J}$. The E field is in direction $\hat{\underset{\sim}{n}}$ whereas the $\underset{\sim}{J}$ vector is orthogonal to the tangent plane where the line $r\hat{\underset{\sim}{n}}$ meets the surface of the ellipsoid. The current density in direction $\hat{\underset{\sim}{n}}$ is simply E/r^2 where *r* is length of line from centre of ellipsoid to its surface in direction $\hat{\underset{\sim}{n}}$.

The long axis of the conductivity ellipsoid $\hat{z}'$, which represents the direction of the dominant principal resistivity, often co-incides with the normal to the major rock lineation. It is referred to as the transverse direction. It is characterised by polar angles θ_0 and φ_0, which give the inclination (dip) and azimuth (bearing) respectively in spherical co-ordinates. It has components:

$$\hat{z}' = \left(\cos\varphi_0 \sin\theta_0, \sin\varphi_0 \sin\theta_0, \cos\theta_0\right) \tag{3.9}$$

The other two principal directions lie in the plane perpendicular to this direction. The third (Euler) angle is the amount of tilt rotation about the $\hat{z}'$ axis to fix the orientation of $\hat{x}'$ in the plane perpendicular to $\hat{z}'$. Alternatively, it can be expressed as the azimuth swing (call it ε) of $\hat{x}'$ from that of $\hat{z}'$. A special case is that in which ε = 0 so that direction $\hat{x}'$ is obtained simply by adding 90 degrees to θ_0:

$$\hat{x}' = \left(\cos\varphi_0 \cos\theta_0, \sin\varphi_0 \cos\theta_0, -\sin\theta_0\right) \tag{3.10}$$

The third unit vector $\hat{y}'$ is obtained from the orthogonality property by taking the cross-product:

$$\hat{y}' = \hat{z}' \times \hat{x}' = \left(-\sin\varphi_0, \cos\varphi_0, 0\right) \tag{3.11}$$

So defining as the rotation matrix

$$R = \begin{pmatrix} \hat{x}' \\ \hat{y}' \\ \hat{z}' \end{pmatrix} = \begin{pmatrix} \cos\varphi_0 \cos\theta_0 & \sin\varphi_0 \cos\theta_0 & -\sin\theta_0 \\ -\sin\varphi_0 & \cos\varphi_0 & 0 \\ \cos\varphi_0 \sin\theta_0 & \sin\varphi_0 \sin\theta_0 & \cos\theta_0 \end{pmatrix} \tag{3.12}$$

we can now compute the conductivity matrix in the cartesian or recording frame as the product of the three matrices: $\boldsymbol{\sigma} = R^T \boldsymbol{\sigma}' R$ where the diagonal eigenvalue matrix σ' is given by equation (3.3).

The six components of the conductivity tensor can now be written out as follows in terms of the principal conductivities and the two polar angles defining the direction of dominant eigenvector:

$$\begin{pmatrix} \sigma_{xx} \\ \sigma_{xy} \\ \sigma_{xz} \\ \sigma_{yy} \\ \sigma_{yz} \\ \sigma_{zz} \end{pmatrix} = \begin{pmatrix} \sigma_1 \cos^2\theta_0 \cos^2\varphi_0 + \sigma_2 \sin^2\varphi_0 + \sigma_3 \sin^2\theta_0 \cos^2\varphi_0 \\ 0.5\left(\sigma_1 \cos^2\theta_0 \sin 2\varphi_0 - \sigma_2 \sin 2\varphi_0 + \sigma_3 \sin^2\theta_0 \sin 2\varphi_0\right) \\ 0.5\left(\sigma_3 - \sigma_1\right)\cos\varphi_0 \sin 2\theta_0 \\ \sigma_1 \cos^2\theta_0 \sin^2\varphi_0 + \sigma_2 \cos^2\varphi_0 + \sigma_3 \sin^2\theta_0 \sin^2\varphi_0 \\ 0.5\left(\sigma_3 - \sigma_1\right)\sin\varphi_0 \sin 2\theta \\ \sigma_1 \sin^2\theta_0 + \sigma_3 \cos^2\theta_0 \end{pmatrix} \tag{3.13}$$

For the 2.5-D situation, one principal axis is taken to be parallel to strike i.e. $y \| \hat{y}'$. The conductivity components are obtained by letting the azimuth angle $\phi_0 = 0$.

$$\begin{pmatrix} \sigma_{xx} \\ \sigma_{xz} \\ \sigma_{yy} \\ \sigma_{zz} \end{pmatrix} = \begin{pmatrix} \sigma_1 \cos^2\theta_0 + \sigma_3 \sin^2\theta_0 \\ 0.5\left(\sigma_3 - \sigma_1\right)\sin 2\theta_0 \\ \sigma_2 \\ \sigma_1 \sin^2\theta_0 + \sigma_3 \cos^2\theta_0 \end{pmatrix} \tag{3.14}$$

Note that in both cases, the trace of the conductivity tensor $\left(Tr\left\{\boldsymbol{\sigma}\right\} = \sigma_{xx} + \sigma_{yy} + \sigma_{zz}\right)$ is equal to the sum of the eigenvalues $\sigma_1 + \sigma_2 + \sigma_3$. The above model, involving just 5 parameters in the 3-D case, is slightly less complex than the most general anisotropic case (3 angles, 3 principal values) but when there is isotropy in the plane of stratification, which is frequently the situation, there is no need to concern oneself with eigenvector $\left(\hat{x}, \hat{y}\right)$ orientation in the plane perpendicular to $\hat{z}$. This particular class of practical model will now be considered.

3.3 The Tilted Transversely Isotropic (TTI) Medium

A special 3-D situation where azimuth is still important, and finds widespread application, is that in which the two principal conductivities in the plane orthogonal to $\hat{z}'$ are equal. $\sigma_1 = \sigma_2$. This is referred to as a transversely isotropic (TI) medium and was discussed in section 1.3.2. The medium anisotropy is then characterised by just four parameters: the longitudinal resistivity $\rho_l = 1/\sigma_1 = 1/\sigma_2$, the transverse resistivity $\rho_t = 1/\sigma_3$, the dip angle θ_0 and azimuth

angle φ_0 which define the arbitrary axis of symmetry which lies normal to the plane of stratification (eg bedding plane, fracture plane, cleavage plane). This plane is characterised in terms of strike angle $\beta = \varphi_0 + \pi/2$ and the dip angle from the horizontal $\alpha = \theta_0$ (see Fig 3.3). Resistivity is constant at ρ_l for any direction within the bedding plane, but different in all other directions, reaching its maximum value ρ_t along the symmetry axis or transverse direction (ϕ_0, θ_0). The tensor ellipsoid for this special case of TI media has circular cross section perpendicular to the long axis.

As an alternative to ρ_l and ρ_t, we introduce two auxiliary quantities:

$$\rho_m = \sqrt{\rho_l \rho_t} \qquad\qquad \lambda = \sqrt{\rho_t / \rho_l} \tag{3.15}$$

The quantity λ is called the coefficient of anisotropy, typically in the range 1 to 3 (see section 1.3.2), while ρ_m is the geometric mean of the two principal resistivities. It is sometimes referred to as the equivalent isotropic medium resistivity. Replacing σ_1, σ_2 with σ_l and σ_3 with σ_t in equation (3.13), the TTI tensor becomes:

$$\begin{pmatrix} \sigma_{xx} \\ \sigma_{xy} \\ \sigma_{xz} \\ \sigma_{yy} \\ \sigma_{yz} \\ \sigma_{zz} \end{pmatrix} = \begin{pmatrix} \sigma_l \left(\cos^2\theta_0 \cos^2\varphi_0 + \sin^2\varphi_0 \right) + \sigma_t \sin^2\theta_0 \cos^2\varphi_0 \\ 0.5\left(\sigma_l \left(\cos^2\theta_0 \sin 2\varphi_0 - \sin 2\varphi_0 \right) + \sigma_t \sin^2\theta_0 \sin 2\varphi_0 \right) \\ 0.5\left(\sigma_t - \sigma_l \right) \cos\varphi_0 \sin 2\theta_0 \\ \sigma_l \left(\cos^2\theta_0 \sin^2\varphi_0 + \cos^2\varphi_0 \right) + \sigma_t \sin^2\theta_0 \sin^2\varphi_0 \\ 0.5\left(\sigma_t - \sigma_l \right) \sin\varphi_0 \sin 2\theta \\ \sigma_l \sin^2\theta_0 + \sigma_t \cos^2\theta_0 \end{pmatrix} \tag{3.16}$$

For an isotropic case, $\sigma_l = \sigma_t = \sigma$, all diagonal elements σ_{ii} reduce to the same scalar value σ, and the off-diagonal elements vanish. For the general 2.5-D case with no azimuthal dependence, we obtain:

$$\begin{pmatrix} \sigma_{xx} \\ \sigma_{xz} \\ \sigma_{yy} \\ \sigma_{zz} \end{pmatrix} = \begin{pmatrix} \sigma_l \cos^2\theta_0 + \sigma_t \sin^2\theta_0 \\ 0.5\left(\sigma_t - \sigma_l \right) \sin 2\theta_0 \\ \sigma_l \\ \sigma_l \sin^2\theta_0 + \sigma_t \cos^2\theta_0 \end{pmatrix} \tag{3.17}$$

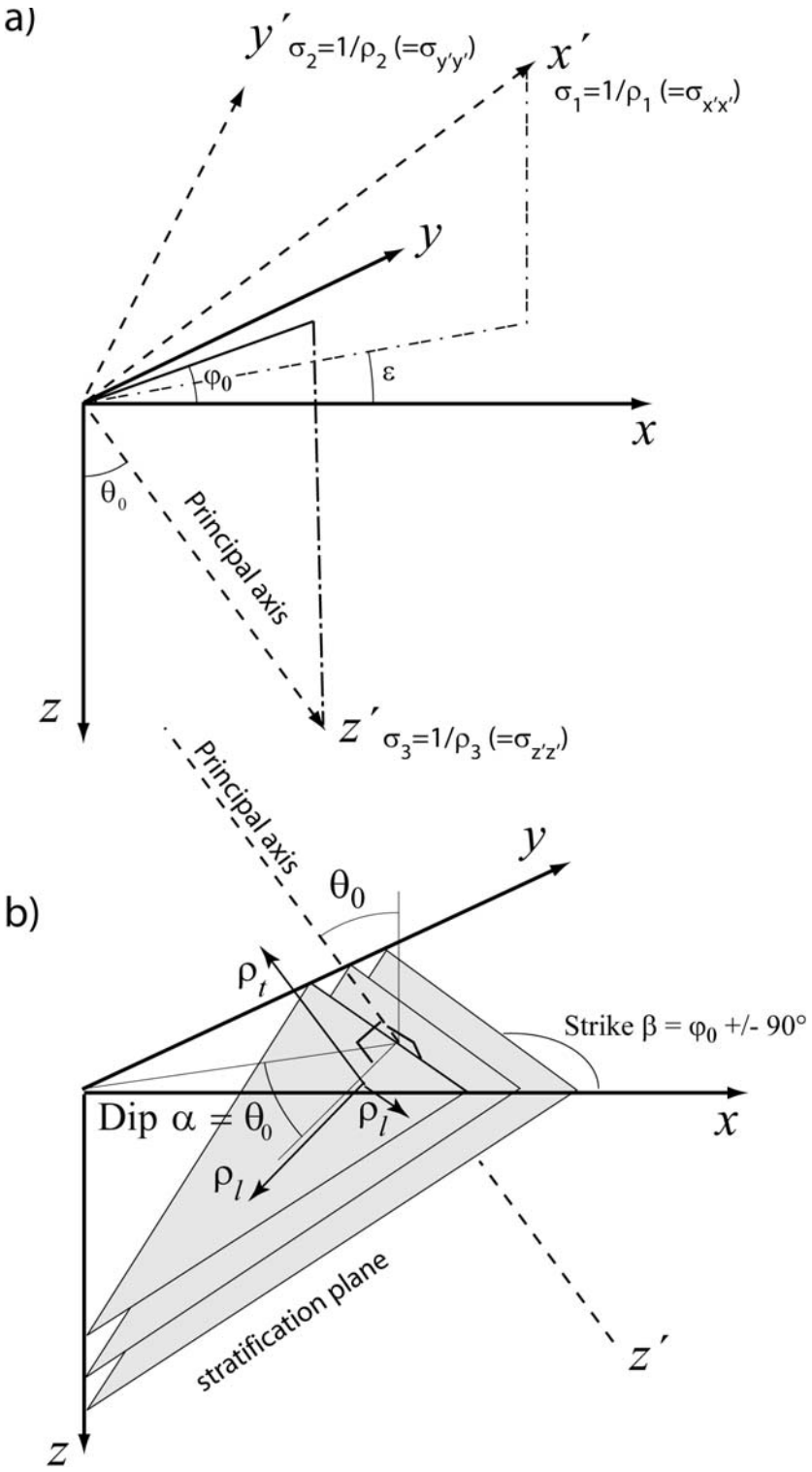

Figure 3.3. (a) Geographic recording frame (*x*,*y*,*z*) and the rotated or natural rock frame (*x'*,*y'z'*) which defines the principal conductivity directions. The symmetry axis is in the *z'* direction (or σ_3 direction), specified by polar angles φ_0, θ_0. This is the minimum conductivity (maximum resistivity) direction. If the azimuth of the *x'* axis, *ε*, is equal to that of the *z'* axis, φ_0, then the number of independent components of the conductivity tensor reduces from 6 to 5 (3 principal values - $\sigma_1, \sigma_2, \sigma_3$ - and two polar angles φ_0, θ_0). (b) Special case of tilted transversely isotropic media showing plane of stratification (foliation) having strike β = $\varphi_0 \pm 90°$ and dip from horizontal α = θ_0. The longitudinal conductivity, in the plane of stratification, is σ_l and the transverse conductivity, in the direction of the symmetry axis (normal to the plane of stratification) is σ_t. The longitudinal and transverse resistivities are $\rho_l = 1/\sigma_l$ and $\rho_t = 1/\sigma_t$.

3.4 Electric Potential and Current Density in a Uniform Medium

3.4.1 VTI Medium

Keller and Frischknecht (1970) show for a medium having a vertical symmetry axis (i.e horizontally layered or VTI medium) the potential *U* at some arbitrary point *P(x,y,z)* in the medium due to a current source I on the surface at the origin is given by:

$$U(x,y,z) = \frac{I\rho_l\lambda}{2\pi\sqrt{x^2+y^2+\lambda^2z^2}} \tag{3.18a}$$

The equipotential surfaces are then given by:

$$x^2 + y^2 + \lambda^2 z^2 = C \tag{3.18b}$$

where C is a constant. i.e., they are ellipsoids of revolution about the z-axis. The components of the current density $\vec{J}$ are given by:

$$J_x = -\frac{1}{\rho_l}\frac{\partial U}{\partial x}, \quad J_y = -\frac{1}{\rho_l}\frac{\partial U}{\partial y}, \quad J_z = -\frac{1}{\rho_t}\frac{\partial U}{\partial z} \tag{3.19}$$

Now we can recast these results entirely in terms of the distance $R = \sqrt{x^2+y^2+z^2}$ to the point of measurement and the angle of inclination ψ from the symmetry axis (in this case vertical) using:

$$\begin{aligned} x^2 + y^2 &= R^2\sin^2\psi \\ z^2 &= R^2\cos^2\psi \end{aligned} \tag{3.20}$$

Note that for a vertical axis of symmetry the situation is axisymmetric, i.e., has azimuthal symmetry. Therefore there is no dependence of the potential on the azimuth angle to point P.

Therefore $U = \frac{I\lambda\rho_l}{2\pi R\sqrt{1+\left(\lambda^2-1\right)\cos^2\psi}}$ (3.21)

Differentiating and substituting equation (3.21) into the current density equations (3.19) provides the current density in the alternative co-ordinates. The component of current density in the direction of the symmetry axis $\left(J_{\parallel} = J_z\right)$ is:

$$J_{\parallel} = \frac{I\lambda\cos\psi}{2\pi R^2\left(1+\left(\lambda^2-1\right)\cos^2\psi\right)^{3/2}} \tag{3.22}$$

and that in the orthogonal direction $\left(J_{\perp} = \sqrt{J_x^2 + J_y^2}\right)$ is:

$$J_{\perp} = \frac{I\lambda\sin\psi}{2\pi R^2\left(1+\left(\lambda^2-1\right)\cos^2\psi\right)^{3/2}} \tag{3.23}$$

3.4.2 TTI Medium

Now we want to translate these results into situations where the axis of symmetry is tilted in some arbitrary direction. For such a TTI medium let the axis of symmetry have azimuth ϕ_0 (from the x axis) and inclination angle θ_0 (from the vertical or z axis, see Fig. 3.4). The unit vector $\hat{z}'$ defining this direction has Cartesian components given by equation (3.9). The point P at which we want to compute the potential and the current density has spherical co-ordinates $\left(R,\phi,\theta\right)$. The unit vector defining this direction has Cartesian components:

$$\hat{n} = \left(\sin\theta\cos\phi, \sin\theta\sin\phi, \cos\theta\right) \tag{3.24}$$

The cosine of the incident angle ψ measured relative to the symmetry axis is found by taking the dot product between the unit vectors $\hat{z}'$ and $\hat{n}$:

$$\cos\psi = \hat{z}'\cdot\hat{n} = \sin\theta_0\sin\theta\cos\left(\phi-\phi_0\right) + \cos\theta_0\cos\theta \tag{3.25}$$

If we now substitute for $\cos\psi$ from equation (3.25) into equation (3.21) we find the potential at any interior point $P\left(R,\phi,\theta\right)$ for a rotated symmetry axis, in the geographic frame.

Similarly, it is possible to find the current density $\vec{J}$ for a tilted axis of symmetry in terms of the original co-ordinate system:

$$\begin{aligned} J_x &= J_{\|}\cos\phi_0\sin\theta_0 + J_{\perp}\cos\phi_0\cos\theta_0 \\ J_y &= J_{\|}\sin\phi_0\sin\theta_0 + J_{\perp}\sin\phi_0\cos\theta_0 \\ J_z &= J_{\|}\cos\theta_0 - J_{\perp}\sin\theta_0 \end{aligned} \qquad (3.26)$$

where $J_{\|}, J_{\perp}$ are given by equations (3.22) and (3.23) and illustrated in (Fig. 3.4).

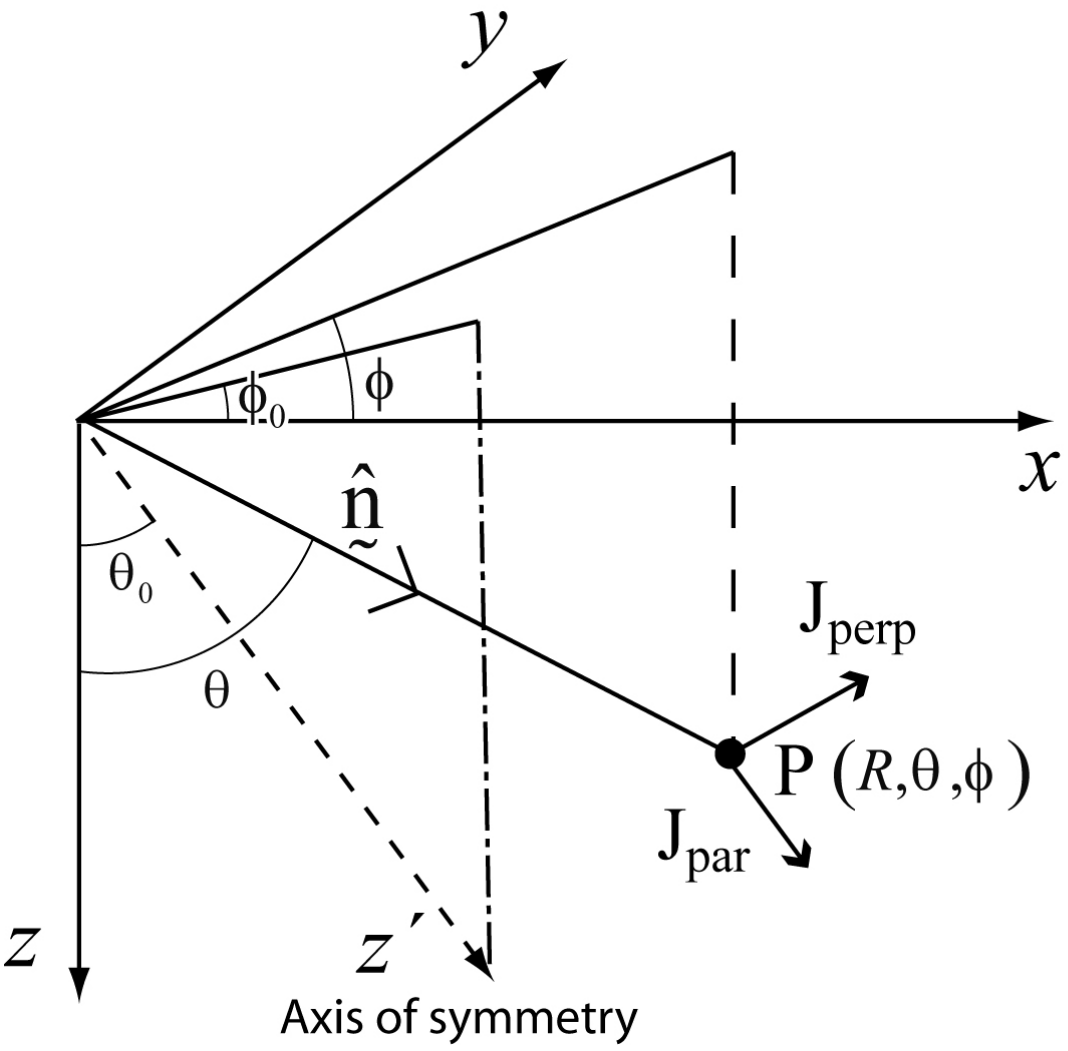

Fig. 3.4 Point P(R, ϕ, θ) inside an anisotropic medium having tilted axis of symmetry (defined by angles ϕ_0, θ_0) at which potential *U* and current density $\vec{J}$ are to be computed.

We will now consider some **special cases**.

For a *vertical axis of symmetry*, with $\theta_0 = 0$, $\cos\psi = \cos\theta$ and $\psi = \theta$, the general solution equation (3.21) reverts to the earlier expression for the VTI medium, with no azimuthal dependence:

$$U\left(R,\phi,\theta\right) = \frac{I\rho_m}{2\pi R\sqrt{1+\left(\lambda^2-1\right)\cos^2\theta}} \tag{3.27}$$

where $\rho_m = \lambda\rho_l$. For vertically dipping beds, or a *horizontal axis of symmetry* $\theta_0 = 90^0$ we have

$$\cos\psi = \sin\theta\cos(\phi-\phi_0) \tag{3.28}$$

and the potential is given by:

$$U(R,\phi,\theta) = \frac{I\rho_m}{2\pi R(1+(\lambda^2-1)\sin^2\theta\cos^2(\phi-\phi_0))^{1/2}} \tag{3.29}$$

Consider now a point P *on the surface* of the Earth. Here z = 0, or θ = 90 and equation (3.25):

$$\cos\psi = \sin\theta_0\cos(\phi-\phi_0) \tag{3.30}$$

Substituting into equation (3.21) we find that the surface potential is given by:

$$U(x,y,0) = U(r,\phi,0) = \frac{I\rho_m}{2\pi r(1+(\lambda^2-1)\cos^2(\phi-\phi_0)\sin^2\theta_0)^{1/2}} \tag{3.31}$$

where $r^2 = x^2 + y^2$. This is the same as the result given by Bhattacharya and Patra (1968, p.18) although they expressed it in terms of the bedding plane strike $\left(\beta = \phi_0 - \phi + 90\right)$ and dip $\left(\alpha = \theta_0\right)$ from the horizontal. They do not give expressions for potential in the subsurface. For a vertical axis of symmetry $\theta_0 = 0$ (bedding plane dip of zero), the potential is:

$$U = \frac{I\rho_m}{2\pi r} \tag{3.32}$$

with no azimuthal dependence. The apparent resistivity for a pole-pole array is:

$$\rho_a = 2\pi r.\frac{U}{I} = \rho_m = \lambda\rho_l \tag{3.33}$$

This is the case of a profile oriented in a direction parallel to the layering or in the longitudinal resistivity direction. However, the apparent resistivity is greater than the longitudinal resistivity by a factor equal to the coefficient of anisotropy.

Next consider the case of *vertically dipping beds* i.e., horizontal axis of symmetry $\theta_0 = 90$ and again with observations at the Earth's surface. Consider a profile in the same direction as the strike of the bedding plane, $\phi = \phi_0$. From equation (3.29) we find that

$$U(r,\phi,90) = \frac{I\rho_m}{2\pi r.\lambda} = \frac{I\rho_l}{2\pi r} \tag{3.34}$$

and the apparent resistivity for a pole-pole array is $\rho_a = \rho_l$. Note that this is the case of a profile oriented in a direction perpendicular to the layering or in the transverse resistivity direction, yet the apparent resistivity is equal to the longitudinal resistivity, not the transverse resistivity. This is referred to as the Paradox of Anisotropy, and was introduced in section 1.3.3.

For profiles parallel to the strike of the bedding plane, the apparent resistivity is again equal to ρ_m. There is a clear azimuthal dependence in the apparent resistivity, with values ranging between ρ_l and ρ_m.

3.4.3 Illustrative Example

Figure 3.5a shows the equipotential and current density patterns in the subsurface for a surface current electrode over a uniform isotropic medium having a conductivity of 0.1 S/m. The diagram is for a single vertical slice through the current electrode which is located to position (0,0). Note the circular equipotential patterns and the constant magnitude of the current density vectors (indicated by arrows) at a fixed radial distance from the current electrode. There is no angular variation of the current density. Both the potential and the current density fall off inversely with distance. Note also that the current density vectors are everywhere orthogonal to the equipotential contours.

By contrast, Fig. 3.5b shows the corresponding patterns for a current electrode on the surface above a uniform, anisotropic TI medium having a longitudinal conductivity of 0.1S/m, a transverse conductivity of 0.025 S/m and a dipping axis of symmetry of tilt angle 45 degrees. The azimuth of the axis of symmetry is ϕ_0 = 0 degrees. The cross section is at an azimuth of ϕ = 0 degrees and passes through the current source. We now observe a pronounced asymmetry in the equipotential patterns (elliptical) with the long axis of the ellipse in the longitudinal direction (i.e parallel to the bedding plane). The current density now not only falls off with increasing distance from the current source but there is also a pronounced angular variation, with maximum current density in the longitudinal (most conductive) direction (i.e parallel to the plane of stratification) and minimum current density in the transverse conductivity direction (parallel to the bedding plane normal). Also we observe that the current density vectors are no longer perpendicular to the equipotential contours, except along the axes of the ellipse.

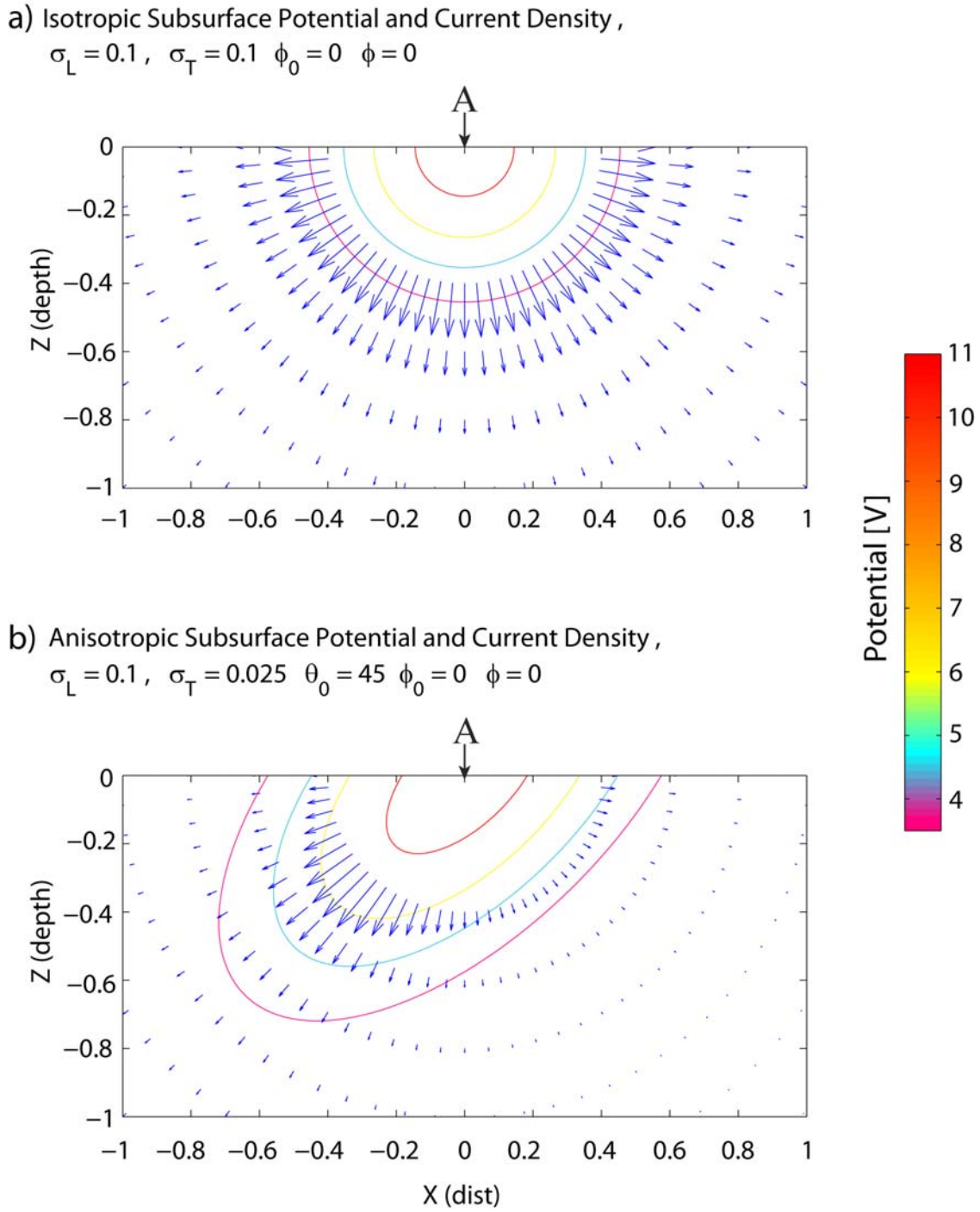

Figure 3.5 The equipotential and current density patterns in the subsurface for a surface current electrode

Chapter 4
New Gaussian Quadrature Grid Method for Resistivity Modelling

It has been shown that the spectral method (Trefethen 2000) and the spectral element method (Komatitsch and Tromp 1999) have more attractive features than the two traditional FDM and FEM numerical methods used in resistivity modelling (as reviewed in section 2.3). The main advantages lie in the capability to simulate complex physical models and the exponential power convergence. They have been successfully applied to fluid flow dynamic modelling (Boyd 1989), seismic wave simulations (Komatitsch and Tromp 1999) and electromagnetic computations (Martinec 1999).

The spectral method uses some global series of orthogonal functions to present the unknown solution at the irregular collocation points, subject to boundary conditions. The resulting linear system matrix is full. The spectral element method combines the spectral method and the finite element method, and it possesses the main advantages of each. This includes the capability to handle various model shapes, the sparse matrix format of the FEM and the exponential power convergence of the spectral method.

In this chapter I develop and present the theory for a new method of 3-D/2.5-D DC resistivity modelling in heterogeneous, anisotropic media having arbitrary surface topography. The scheme is based on Gaussian Quadrature Grids (GQG). It was inspired by the spectral element approach, but does not require a constant element mesh matching the surface topography (avoiding the 2-D/3-D mesh generator), or the resistivity tensor to be constant within the element integrations. It is particularly well suited for handling arbitrary surface topography and easily accommodates general anisotropy of the medium. This new method makes complex forward modelling much easier.

4.1 Variational Principle

The Variational Principle is the basis for the method. For completeness, I give a brief introduction here. More details can be found in Graham and Oden's book (1983. p96). The Variational Principle states that the following boundary-value problem of a partial differential equation:

$$\begin{cases} Du = f, & r \in \Omega \\ \dfrac{\partial u}{\partial n} + \nu u = 0, & r \in \Gamma \end{cases} \tag{4.1}$$

may be solved by minimizing the following functional

$$\Psi(u) = \frac{1}{2}\langle u, Du\rangle - \langle u, f\rangle \tag{4.2}$$

incorporating the boundary condition, provided that the differential operator D is linear and self-adjoint. This means that the following equations are satisfied for arbitrary differentiable functions u, v, w and a constant λ:

$$\begin{aligned} \langle w, Du\rangle &= \langle u, Dw\rangle \\ \langle w, D(u+\lambda v)\rangle &= \langle w, Du\rangle + \lambda\langle w, Dv\rangle \end{aligned} \tag{4.3}$$

Here, the angular bracket represents the integral over the domain Ω:

$$\langle f, g\rangle = \int_{\Omega} f(r)\, g(r) d\Omega \tag{4.4}$$

The principle is based on the variational analysis for an arbitrary small change δu, which gives rise to:

$$\begin{aligned} \delta\Psi &= \frac{1}{2}\left[\langle \delta u, Du\rangle + \langle u, D\delta u\rangle\right] - \langle \delta u, f\rangle \\ &= \frac{1}{2}\left[\langle \delta u, Du\rangle + \langle \delta u, Du\rangle\right] - \langle \delta u, f\rangle \\ &= \langle \delta u, Du - f\rangle = 0 \end{aligned} \tag{4.5}$$

Equation (4.5) shows that $\delta\Psi$ vanishes if and only if $Du = f$, $\forall \delta u$, which is the governing equation in the boundary-value problem (4.1). The Variational Principle may be applied to 2.5-D and 3-D resistivity anisotropic forward modelling, in which the governing equations are:

$$\text{2.5D: } \begin{cases} \vec{\nabla}\cdot\left(\boldsymbol{\sigma}\cdot\vec{\nabla}\bar{G}\right)+k_y^2\sigma_{yy}\bar{G}=-\dfrac{1}{2}\delta\left(r-r_s\right) & r=\left(x,z\right)\in\Omega \\ \left(\boldsymbol{\sigma}\cdot\vec{\nabla}\bar{G}\right)\cdot\vec{n}+v\bar{G}=0 & r=\left(x,z\right)\in\Gamma \end{cases} \tag{4.6}$$

$$\text{3D: } \begin{cases} \vec{\nabla}\cdot\left(\boldsymbol{\sigma}\cdot\vec{\nabla}G\right)=-\delta\left(r-r_s\right) & r=\left(x,y,z\right)\in\Omega \\ \left(\boldsymbol{\sigma}\cdot\vec{\nabla}G\right)\cdot\vec{n}+vG=0 & r=\left(x,y,z\right)\in\Gamma \end{cases} \tag{4.7}$$

Here $\boldsymbol{\sigma}$ is in general a 2 × 2 or 3×3 symmetric conductivity matrix in the 2.5-D or 3-D case, $\vec{n}$ is the unit normal vector to the boundary Γ, v is a known function of the spatial coordinates and the conductivity, which specifies the mixed boundary condition derived in the next section, r_s is the current point-source location, and $\bar{G}$ or G is the Green's function (the potential response to a unit current injection) in the wavenumber (Fourier transformed with respect to the strike or y direction) or spatial domain, respectively.

Chapter 3 examined the conductivity tensor in some detail. It was shown that if the medium has elliptical anisotropy, i.e. defined by the three principal values $\left(\sigma_{x'x'},\sigma_{y'y'},\sigma_{z'z'}\right)$ and with the symmetry-axis in the $\hat{z}$ direction defined by the orientation angles $\left(\varphi_0,\theta_0\right)$, the conductivity tensor $\boldsymbol{\sigma}$ has components:

$$\text{2.5D: } \begin{pmatrix}\sigma_{xx}\\ \sigma_{xz}\\ \sigma_{yy}\\ \sigma_{zz}\end{pmatrix}=\begin{pmatrix}\sigma_{x'x'}\cos^2\theta_0+\sigma_{z'z'}\sin^2\theta_0\\ 0.5\left(\sigma_{z'z'}-\sigma_{x'x'}\right)\sin 2\theta_0\\ \sigma_{y'y'}\\ \sigma_{x'x'}\sin^2\theta_0+\sigma_{z'z'}\cos^2\theta_0\end{pmatrix} \tag{4.8}$$

$$\text{3D: } \begin{pmatrix}\sigma_{xx}\\ \sigma_{xy}\\ \sigma_{xz}\\ \sigma_{yy}\\ \sigma_{yz}\\ \sigma_{zz}\end{pmatrix}=\begin{pmatrix}\sigma_{x'x'}\cos^2\theta_0\cos^2\varphi_0+\sigma_{y'y'}\sin^2\varphi_0+\sigma_{z'z'}\sin^2\theta_0\cos^2\varphi_0\\ 0.5\left(\sigma_{x'x'}\cos^2\theta_0\sin 2\varphi_0-\sigma_{y'y'}\sin 2\varphi_0+\sigma_{z'z'}\sin^2\theta_0\sin 2\varphi_0\right)\\ 0.5\left(\sigma_{z'z'}-\sigma_{x'x'}\right)\cos\varphi_0\sin 2\theta_0\\ \sigma_{x'x'}\cos^2\theta_0\sin^2\varphi_0+\sigma_{y'y'}\cos^2\varphi_0+\sigma_{z'z'}\sin^2\theta_0\sin^2\varphi_0\\ 0.5\left(\sigma_{z'z'}-\sigma_{x'x'}\right)\sin\varphi_0\sin 2\theta\\ \sigma_{x'x'}\sin^2\theta_0+\sigma_{z'z'}\cos^2\theta_0\end{pmatrix} \tag{4.9}$$

Applying equation (4.2) to the Helmholtz equations (4.6) and (4.7) gives:

2.5-D: $$\Psi\left(\bar{G}\right)=\frac{1}{2}\left(\int_{\Omega}\left[\left(\boldsymbol{\sigma}\cdot\vec{\nabla}\bar{G}\right)\cdot\vec{\nabla}\bar{G}+k_y^2\sigma_{yy}\bar{G}^2\right]d\Omega+\int_{\Gamma}v\bar{G}^2d\Gamma-\bar{G}_s\right) \tag{4.10}$$

3-D: $$\Psi\left(G\right)=\frac{1}{2}\left(\int_{\Omega}\left[\left(\boldsymbol{\sigma}\vec{\nabla}G\right)\cdot\vec{\nabla}G\right]d\Omega+\int_{\Gamma}vG^2d\Gamma-G_s\right) \tag{4.11}$$

Here, $\bar{G}_s$ or G_s means the value of the Green's function at the source position, expressed by the interpolation formula of the neighbouring points when the functionals in (4.10) and (4.11) are discretized.

4.2 Anisotropic Mixed-Boundary Condition

In numerical modelling, a finite region has to be considered for efficiency, so special boundary conditions are used in numerical techniques. The boundary $\partial\Omega$ is integrated over when the Variational Principle is applied to the resistivity Helmholtz equation. This means that the operator B in the mixed Dirichlet / Neumann boundary condition in equation (2.21) must be designed for this case. A self-adjoint differential operator B is also desired so as to make the operator $L\left(k_y,\boldsymbol{\sigma}\right)$ self adjoint too, and to ensure that the resultant element matrix becomes symmetric.b

Normally, the boundary consists of two parts: the earth's surface Γ_s and the artificial boundary Γ_a (under the ground). On the earth's surface, because no current crosses it, the Neumann boundary should be satisfied, for the 3-D case:

$$\frac{\partial U}{\partial n} = 0, \qquad r\in\Gamma_{s,} \tag{4.12}$$

where $r=\left(x,y,z\right)$ represents the coordinates of the boundary and $n=\left(n_x,n_y,n_z\right)$ is the outward unit vector normal to the boundary. In the 2.5-D case, we have

$$\frac{\partial \bar{U}}{\partial n} = 0, \qquad r\in\Gamma_{s,} \tag{4.13}$$

For simplicity and since $n_y = 0$, we take $\vec{n} = (n_x, n_z)$ and $r = (x, z)$. $\bar{U}$ is the Fourier-cosine transform of the 3-D electric potential. On the artificial boundary (the left and right sides and the bottom of the numerical grid), Dey and Morrison (1979a,b) proposed a mixed boundary condition in their FDM. Several researchers have shown that the mixed boundary condition produces better numerical solutions than either the classical Dirichlet or Neumann boundary conditions (Zhou and Zhong, 1984).

Here we derive the expressions for the parameter v which appears in equations (4.6) - (4.7). Consider a homogeneous anisotropic medium, at least at the position of the boundaries far away from the source. The Green's function of a point source (I=1) located at (0, 0,0) may be simply written in the form (Li and Uren, 1997):

$$G = \frac{C}{\sqrt{\vec{r}^T \cdot \boldsymbol{\rho} \cdot \vec{r}}}, \tag{4.14}$$

where $\vec{r} = (x, y, z)$, constant $C = \sqrt{|\rho_{ij}|}/2\pi$ and $\rho_{ij} = [\sigma_{ij}]^{-1}$ is the resistivity tensor, the inverse matrix of the conductivity tensor. For the 2.5-D problem $(\rho_{xy} = \rho_{yz} = 0)$, the Green's function becomes (see chapter 3):

$$G = \frac{C/\sqrt{\rho_{yy}}}{\sqrt{\rho_{xx}x^2 + 2\rho_{xz}xz + \rho_{zz}z^2/\rho_{yy} + y^2}} = \frac{C'}{\sqrt{a + y^2}}, \tag{4.15}$$

where $C' = C/\sqrt{\rho_{yy}}$ and the quantity $a > 0$

$$a = \frac{1}{\rho_{yy}}\left(\rho_{xx}x^2 + 2\rho_{xz}xz + \rho_{zz}z^2\right) = \frac{1}{\rho_{yy}}\begin{pmatrix} x & z \end{pmatrix}\begin{pmatrix} \rho_{xx} & \rho_{xz} \\ \rho_{xz} & \rho_{zz} \end{pmatrix}\begin{pmatrix} x \\ z \end{pmatrix} \tag{4.16}$$

as required by the positivity of the resistivity matrix $\boldsymbol{\rho}$. According to the definition of the McDonald function:

$$\int_0^\infty \frac{\cos(k_y y)}{\sqrt{a + y^2}} dy = K_0\left(k_y\sqrt{a}\right) \tag{4.17}$$

The Fourier cosine transformed Green's function may be calculated by

$$\bar{G} = C' K_0\left(k_y \sqrt{a}\right). \tag{4.18}$$

Differentiating the above with respect to (*x*, *z*) and replacing $C' = \bar{G} \Big/ K_0\left(k_y \sqrt{a}\right)$, we have the gradient:

$$\nabla \bar{G} = -\frac{k_y}{2\sqrt{a}} \left[\frac{K_1\left(k_y \sqrt{a}\right)}{K_0\left(k_y \sqrt{a}\right)} \nabla a \right] \bar{G} \tag{4.19}$$

Here ∇a can be calculated from equation (4.16) and the coefficient v for the 2.5-D mixed boundary condition is:

$$v = \frac{k_y}{2\sqrt{a}} \left[\frac{K_1\left(k_y \sqrt{a}\right)}{K_0\left(k_y \sqrt{a}\right)} \right] \left(\sigma \vec{\nabla} a\right) \cdot \vec{n} \tag{4.20}$$

In a 3-D case, one may directly calculate the following product with equation (4.14):

$$\left(\boldsymbol{\sigma} \vec{\nabla} G\right) \cdot \vec{n} = \left[-\frac{1}{2B} \left(\boldsymbol{\sigma} \vec{\nabla} B\right) \cdot \vec{n} \right] G \ , \tag{4.21}$$

where

$$B = \vec{r}^{\,T} \cdot \boldsymbol{\rho} \cdot \vec{r} \qquad \vec{\nabla} B = 2 \boldsymbol{\rho} \vec{r} \ , \tag{4.22}$$

From equation (4.21), the coefficient is

$$v = \frac{1}{2B} \left(\boldsymbol{\sigma} \vec{\nabla} B\right) \cdot \vec{n} \ . \tag{4.23}$$

It should be noted that the operator v used in the boundary integral is dependent on the position of the source and the wavenumber k_y for 2.5-D. In a practical DC resistivity survey, different source positions (current injection points) are commonly employed to obtain the maximum information about the resistivity variation in the medium. If we directly use the

boundary operator v, it leads to redundant computations in the boundary integral due to the different source locations, and for any given k_y. An efficient way is to replace the source point in v with the average position of all the current injection points so that the boundary integral is calculated only once and for each wavenumber. This saves much computer memory and computer time. Obviously, the replacement is reasonable when the DC resistivity survey is simulated within the relatively small central area of the entire computational range.

4.3 Discretisation of a 2-D Functional

For 2.5-D resistivity modelling, the subsurface is often limited by a 2-D computational domain, i.e $(x,z)\in\left[x_1,x_{N_x}\right]\times\left[0,z_0(x)\right]$, where the function $z_0(x)$ gives the topography of the Earth's surface (see Fig. 4.1). The functional given in the previous section may be calculated by summation of successive integrals over the intervals $L_i:[x_i,x_{i+1}]$, $(i=1,2,\ldots,N_x-1;N_x\geq 2)$ in which the topography $z_0(x)$ is differentiable, i.e. $z_0(x)\in C^1(L_i)$, the integral becomes

$$\int_{\Omega} F(\boldsymbol{\sigma},\bar{G},\nabla\bar{G})d\Omega=\sum_{i=1}^{Nx-1}\left[\int_{x_i}^{x_{i+1}}\int_{0}^{z_0(x)} F(\boldsymbol{\sigma},\bar{G},\nabla\bar{G})dxdz\right], \tag{4.24}$$

where the integrand $F(\sigma,\bar{G},\nabla\bar{G})$ is a function of the conductivity tensor σ, the field quantity $\bar{G}$ and its gradient $\nabla\bar{G}$, all of which in general vary with the spatial coordinates $(x,z)\in\Omega$. In order to calculate the inner integral along the z-axis, we may divide the elevation $z_0(x)$ into N_z-1, $(N_z\geq 2)$ parts and equation (4.24) becomes

$$\sum_{i=1}^{N_x-1}\left[\int_{x_i}^{x_{i+1}}\int_{0}^{z_0(x)} F(\boldsymbol{\sigma},\bar{G},\nabla\bar{G})dxdz=\sum_{i=1}^{Nx-1}\sum_{j=1}^{Nz-1}\int_{x_i}^{x_{i+1}}\left[\int_{\frac{(j-1)z_0(x)}{Nz-1}}^{\frac{z_0(x)}{(Nz-1)}j} F(\boldsymbol{\sigma},\bar{G},\nabla\bar{G})dz\right]dx\right., \tag{4.25}$$

where $z_1(x)=0$, $z_{Nz}(x)=z_0(x)$ and $z_j(x)=(j-1)z_0(x)/(Nz-1)$ may be the sub-surfaces of the model or mathematical boundaries. Particularly, if $Nx=2$ *and* $Nz=2$, then

$x_i = x_1, z_i(x) = 0$ *and* $x_{i+1} = x_2, z_{i+1}(x) = z_0(x)$, then the sub-domain Ω_{ij} reverts to the global domain Ω. To this we apply the variable replacement in the sub-domain $\Omega_{ij} = [x_i, x_{i+1}] \times [z_j(x), z_{j+1}(x)]$ (see Fig. 4.1).

$$
\begin{aligned}
x(\xi) &= (\frac{x_{i+1} - x_i}{2})\xi + (\frac{x_i + x_{i+1}}{2}), \qquad \xi \in [-1,1], \\
z(\xi,\eta) &= [\frac{z_{j+1}(x) - z_j(x)}{2}]\eta + [\frac{z_{j+1}(x) + z_j(x)}{2}], \qquad \eta \in [-1,1],
\end{aligned}
\tag{4.26}
$$

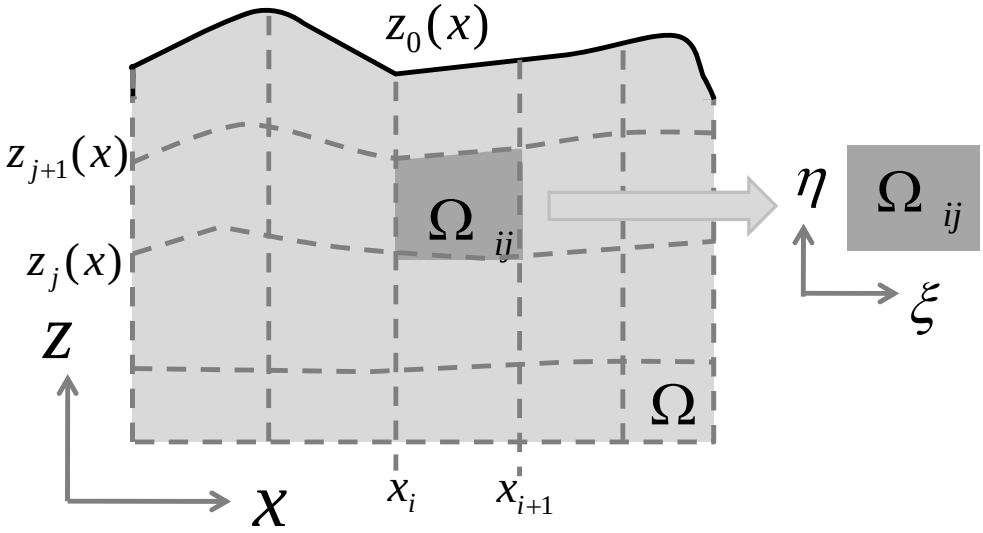

Figure 4.1 Model having topographic surface $z_0(x)$ and transformation of co-ordinates from (x, z) to new coordinates (ξ, η) in the model sub-domains.

The resulting Jacobian matrix is:

$$
\frac{\partial(x,z)}{\partial(\xi,\eta)} = \begin{vmatrix} \frac{\partial x}{\partial \xi} & \frac{\partial z}{\partial \xi} \\ \frac{\partial x}{\partial \eta} & \frac{\partial z}{\partial \eta} \end{vmatrix} = \frac{1}{4}(x_{i+1} - x_i)\left[z_{j+1}(x) - z_j(x)\right] \tag{4.27}
$$

Applying Gaussian quadrature formulae (Stroud and Secrest 1966: Abramowitz and Stegun 1965, Philip and Rabinowitz 1984) to the double intervals in equation (4.25), yields

$$
\begin{aligned}
&\int_{x_i}^{x_{i+1}} [\int_{z_j(x)}^{z_{j+1}(x)} F(\boldsymbol{\sigma}, \bar{G}, \nabla\bar{G}) dz] dx = \int_{-1}^{1}\int_{-1}^{1} F(\boldsymbol{\sigma}, \bar{G}, \nabla\bar{G}) \left|\frac{\partial(x,z)}{\partial(\xi,\eta)}\right| d\xi d\eta \\
&= \sum_{k=1}^{N_\xi^i}\sum_{l=1}^{N_\eta^j} \frac{1}{4} w_k^i w_l^j (x_{i+1} - x_i)\left[z_{j+1}(x) - z_j(x)\right] F(\boldsymbol{\sigma}, \bar{G}, \nabla\bar{G})\Big|_{(\xi_k, \eta_l)},
\end{aligned}
\tag{4.28}
$$

where (ξ_k, η_l) and $\left(w_k^i, w_l^j\right)$ are the Gaussian quadrature abscissae and weights respectively in the 2-D case, and they can be analytically calculated once the integers N_ξ^i and N_η^j are given for the sub-domains (Phillip and Rabinowitz, 1984) $\Omega_{ij} : [x_i, x_{i+1}] \times \left[z_{j+1}(x), z_j(x) \right]$. The accuracy of the numerical integration depends on the number of the abscissae N_ξ^i and N_η^j along with the Gaussian quadrature order. The Gaussian quadrature order determines the number of abscissae in a sub-domain. Gaussian quadrature grid (GQG) refers to the grid generated by the abscissae. It spans the whole domain Ω and may easily fit the topography of the Earth's surface and the sub-surfaces. The key step of computing equation (4.28) is to calculate the values of $F\left(\boldsymbol{\sigma}, \bar{G}, \nabla\bar{G}\right)$ at the Gaussian quadrature abscissae (ξ_k, η_l). This involves sampling the conductivity $\boldsymbol{\sigma}\left(x(\xi_k), z(\xi_k, \eta_l)\right)$ and the Green's function $\bar{G}\left(x(\xi_k), z(\xi_k, \eta_l)\right)$ (representing electric potential) and calculating the gradient $\nabla\bar{G}\left(x(\xi_k), z(\xi_k, \eta_l)\right)$ based on the GQG. It is apparent that such grid may give the details of a complex conductivity model $\boldsymbol{\sigma}(x, z)$ and the electric potential Green's function $\bar{G}(x, z)$.

The GQG method differs from the traditional finite element method and the spectral element methods, both of which require a powerful element generator for fitting a complex topography and the subsurface interfaces in the modelling and assume that each element has constant model parameters, i.e. conductivity tensor (Shewchuk 2002; Rucker *et al.* 2005; Kerry & Weiss 2006).

In order to calculate the gradient $\nabla\bar{G} = \left(\partial\bar{G}/\partial x, \partial\bar{G}/\partial z\right)$, we apply the differential chain rule:

$$\begin{aligned} \frac{\partial\bar{G}}{\partial\xi} &= \frac{\partial\bar{G}}{\partial x}\frac{\partial x}{\partial\xi} + \frac{\partial\bar{G}}{\partial z}\frac{\partial z}{\partial\xi} \\ &= \left(\frac{x_{i+1} - x_i}{2}\right)\left(\frac{\partial\bar{G}}{\partial x} + \frac{\partial z}{\partial\xi}\frac{\partial\bar{G}}{\partial z}\right) \end{aligned} \tag{4.29}$$

$$\frac{\partial\bar{G}}{\partial\eta} = \frac{\partial\bar{G}}{\partial x}\frac{\partial x}{\partial\eta} + \frac{\partial\bar{G}}{\partial z}\frac{\partial z}{\partial\eta} = \frac{z_{j+1}(x) - z_j(x)}{2}\frac{\partial\bar{G}}{\partial z} \tag{4.30}$$

where $\partial z / \partial \xi$ can be calculated by equation (4.26). We now want to express these equations (4.29) and (4.30) in terms of the partial derivatives of the original model coordinates

$$\begin{aligned}\frac{\partial \bar{G}}{\partial x} &= \frac{2}{x_{i+1}-x_i}\frac{\partial \bar{G}}{\partial \xi} - \frac{\left[z'_{j+1}(x)-z'_j(x)\right]\eta + \left[z'_{j+1}(x)+z'_j(x)\right]}{z_{j+1}(x)-z_j(x)}\frac{\partial \bar{G}}{\partial \eta} \\ \frac{\partial \bar{G}}{\partial z} &= \frac{2}{z_{j+1}(x)-z_j(x)}\frac{\partial \bar{G}}{\partial \eta}\end{aligned} \tag{4.31}$$

We approximate the Green's function $\bar{G}$ in the domain $(\xi_k, \eta_l) \in [-1,1]\times[-1,1]\,(\xi_k, \eta_l)$ by Lagrange interpolation:

$$\bar{G}(\xi,\eta) = \sum_{p=1}^{N_\xi^i}\sum_{q=1}^{N_\eta^j} l_p(\xi) l_q(\eta) \bar{G}_{pq} \tag{4.32}$$

This leads to the derivatives with respect to the Gaussian quadrature abscissae (ξ_k, η_l):

$$\begin{aligned}\left(\frac{\partial \bar{G}}{\partial \xi}\right)_{kl} &= \sum_{p=1}^{N_\xi^i}\sum_{q=1}^{N_\eta^j} l'_p(\xi_k) l_q(\eta_l) \bar{G}_{pq} = \sum_{p=1}^{N_\xi^i} l'_p(\xi_k)\bar{G}_{pl} \\ \left(\frac{\partial \bar{G}}{\partial \eta}\right)_{kl} &= \sum_{p=1}^{N_\xi^i}\sum_{q=1}^{N_\eta^j} l_p(\xi_k) l'_q(\eta_l) \bar{G}_{pq} = \sum_{q=1}^{N_\eta^j} l'_q(\eta_l)\bar{G}_{kq}\end{aligned} \tag{4.33}$$

It should be mentioned that the Lagrange interpolation in equation (4.32) actually has the exponential power convergence for the derivatives in equation (4.33). This is due to employing the irregular collocation points which have the Legendre polynomial zeroes' density $\mu_{clus}(x) = \frac{N}{\pi\sqrt{1-x^2}}$. The Legendre / Chebyshev points are $\frac{\pi}{2}$ times less dense in the middle than the equally space grid $\left(\mu_{reg}(x) = \frac{N}{2}\right)$ with the same number of points *N*. So that polynomial interpolation using Legendre distribution of points is $\|f - p_N\| = O\left(const^{-N}\right)$ if *f* is Lipishitz continuous. This is the principle of the spectral method (Trefethen 2000). An improved Barycentric Interpolation Spectral Differentiation matrix is also available (Berrut, Trefethen 2004).

Substituting equations (4.33) for (4.31), we obtain the derivatives with respect to the original coordinates (x, z); they are:

$$\begin{aligned}\left(\frac{\partial \bar{G}}{\partial x}\right)_{kl} &= \sum_{p=1}^{N_\xi^i}\left(\frac{2l_p'(\xi_k)}{x_{i+1}-x_i}\right)\bar{G}_{pl} + \sum_{q=1}^{N_\eta^j}\left(\frac{\left[z_{j+1}'(x)-z_j'(x)\right]\eta+\left[z_{j+1}'(x)+z_j'(x)\right]}{z_{j+1}(x)-z_j(x)}\right)l_q'(\eta_l)\bar{G}_{kq} \\ &= \vec{N}_x(\xi_k,\eta_l)^T\,\vec{\bar{G}}^{(x)}\end{aligned} \tag{4.34}$$

and

$$\begin{aligned}\left(\frac{\partial \bar{G}}{\partial z}\right)_{kl} &= \sum_{q=1}^{N_\eta^j}\left(\frac{2l_q'(\eta_l)}{z_{j+1}(x)-z_j(x)}\right)\bar{G}_{kq} \\ &= \vec{N}_z(\xi_k,\eta_l)^T\,\vec{\bar{G}}^{(z)}\end{aligned}$$

where

$$\begin{aligned}&\vec{\bar{G}}^{(x)} = \vec{\bar{G}}^{(l)} \cup \vec{\bar{G}}^{(k)}, \vec{\bar{G}}^{(z)} = \vec{\bar{G}}^{(k)} \\ &\vec{\bar{G}}^{(l)} = \{\bar{G}_{pl}, p = 1,2,...,N_\xi^i\} \\ &\vec{\bar{G}}^{(k)} = \{\bar{G}_{kq}, q = 1,2,...,N_\eta^j\}\end{aligned} \tag{4.35}$$

and the components of the vectors $\vec{N}_x(\xi_k,\eta_l)$ and $\vec{N}_z(\xi_k,\eta_l)$ are calculated as follows:

$$N_x(\xi_k,\eta_l)_p = \begin{cases}\left(\dfrac{2}{x_{i+1}-x_i}\right)l_p'(\xi_k), & \left(1 \le p \le N_\xi^i\right) \\ \dfrac{\left[z_{j+1}'(x)-z_j'(x)\right]\eta+\left[z_{j+1}'(x)-z_j'(x)\right]}{z_{j+1}(x)-z_j(x)}l_p'(\eta_l), & \left(N_\xi^i < p \le N_\xi^i + N_\eta^j\right)\end{cases}$$

and (4.36)

$$N_z(\xi_k,\eta_l)_p = \frac{2}{z_{j+1}\left(x(\xi_k)\right)-z_j\left(x(\xi_k)\right)}l_p'(\eta_l), \quad \left(1 \le p \le N_\eta^j\right)$$

From equation (4.34) one can see that the derivative $\partial\bar{G}/\partial x$ depends on $z_j'(x)$ and $z_{j+1}'(x)$, the slopes of the top and bottom boundaries of the sub-domain Ω_{ij} (see Fig. 4.1), which are defined by the topography in the interval $[x_i, x_{i+1}]$. This implies that $z_j(x)$ and $z_{j+1}(x)$ must

be differentiable in the interval $[x_i, x_{i+1}]$. In the FEM and the SEM, there is no such requirement, because they use a constant element mesh created by a mesh generator to fit the topography or interfaces. However, the requirement can be easily satisfied by appropriate arrangement of the intervals $[x_i, x_{i+1}]$ in terms of the surface topography or interfaces. Therefore, it does not need the mesh generator and can be applied to any topology or interfaces.

The integrand $F(\boldsymbol{\sigma}, \bar{G}, \nabla\bar{G})$ in the 2.5-D equation (4.10) has the following matrix-vector form upon substitution of the partial derivatives in equation (4.34):

$$\begin{aligned} F(\boldsymbol{\sigma}, \bar{G}, \nabla\bar{G})\big|_{(\xi_k,\eta_l)} = & [\vec{\bar{G}}^{(x)}]^T[\sigma_{xx}(\xi_k,\eta_l)\vec{N}_x(\xi_k,\eta_l)\vec{N}_x^T(\xi_k,\eta_l)]\vec{\bar{G}}^{(x)} \\ & + [\vec{\bar{G}}^{(z)}]^T[\sigma_{zx}(\xi_k,\eta_l)\vec{N}_z(\xi_k,\eta_l)\vec{N}_x^T(\xi_k,\eta_l)]\vec{\bar{G}}^{(x)} \\ & + [\vec{\bar{G}}^{(z)}]^T[\sigma_{zz}(\xi_k,\eta_l)\vec{N}_z(\xi_k,\eta_l)\vec{N}_z^T(\xi_k,\eta_l)]\vec{\bar{G}}^{(z)} \\ & + k_y^2\sigma_{yy}(\xi_k,\eta_l)\bar{G}_{kl}. \end{aligned} \tag{4.37}$$

Therefore, equation (4.24) becomes

$$\int_{x_i}^{x_{i+1}}\left[\int_{z_j(x)}^{z_{j+1}(x)} F(\boldsymbol{\sigma}, G, \nabla G)\,dz\right]dx = \sum_{k=1}^{N_\xi^i}\sum_{l=1}^{N_\eta^j}\left\{\sum_{\substack{p\in(x,z)\\ q\in(x,z)}}[\vec{\bar{G}}^{(p)}]^T[w_{kl}^{(pq)}\vec{N}_p(\xi_k,\eta_l)\vec{N}_q^T(\xi_k,\eta_l)]\vec{\bar{G}}^{(q)} + w_{kl}^{(yy)}k_y^2\bar{G}_{kl}^2\right\}$$

where (4.38)

$$w_{kl}^{(pq)} = \frac{1}{4}(x_{i+1}-x_i)\left[z_{j+1}(x(\xi_k)) - z_j(x(\xi_k))\right]w_k^i w_l^j(\sigma_{pq})_{(\xi_k,\eta_l)}$$

The boundary integral in equation (4.10) may be calculated in terms of the three sides: left (L), right (R) and bottom (B). They are

$$\begin{aligned}\int_L \nu\bar{G}^2 d\Gamma &= \int_0^{z(x_1)} \nu\bar{G}^2 dz = \sum_{j=1}^{N_z-1} \int_{z_j(x_1)}^{z_{j+1}(x_1)} \nu\bar{G}^2 d\eta \\ &= \sum_{j=1}^{N_z-1} \sum_{l=1}^{N_\eta^j} \frac{1}{2}\left[z_{j+1}(x_1) - z_j(x_1)\right] w_l^j \nu_l \bar{G}_{jl}^2\end{aligned} \tag{4.39}$$

$$\begin{aligned}\int_R \nu\bar{G}^2 d\Gamma &= \int_0^{z(x_{Nx})} \nu\bar{G}^2 dz = \sum_{j=1}^{N_z-1} \int_{z_j(x_{Nx})}^{z_{j+1}(x_{Nx})} \nu\bar{G}^2 d\eta \\ &= \sum_{j=1}^{N_z-1} \sum_{l=1}^{N_\eta^j} \frac{1}{2}\left[z_{j+1}(x_{Nx}) - z_j(x_{Nx})\right] w_l^j \nu_l \bar{G}_{jl}^2\end{aligned} \tag{4.40}$$

$$\begin{aligned}\int_B \nu\bar{G}^2 d\Gamma &= \int_{x_1}^{x_{Nx}} \nu\bar{G}^2 dx = \sum_{i=1}^{Nx-1} \frac{(x_{i+1} - x_i)}{2} \int_{-1}^{1} \nu\bar{G}^2 d\xi \\ &= \sum_{i=1}^{Nx-1} \sum_{k=1}^{N_\xi^i} \frac{(x_{i+1} - x_i)}{2} w_k^i \nu_k \bar{G}_{ik}^2\end{aligned} \tag{4.41}$$

Substituting equations (4.38)–(4.41) for (4.10), we arrive at the matrix form of the functional for 2.5-D resistivity modelling

$$\Psi(\vec{\bar{G}}) = \frac{1}{2}\vec{\bar{G}}^T M \vec{\bar{G}} - \vec{b}_s \vec{\bar{G}} \tag{4.42}$$

where $\vec{\bar{G}}$ is the vector consisting of the values at all points of the Gaussian quadrature grid, M is the matrix assembled by the local matrices $w_{kl}^{(pq)} \vec{N}_p(\xi_k, \eta_l) \vec{N}_q^T(\xi_k, \eta_l)$ and the coefficients in equations (4.38)–(4.41) and $\vec{b}_s$ is the source vector containing the interpolation functions so that the equation $\bar{G}_s = \vec{b}_s^T \vec{\bar{G}}$ is satisfied. Therefore, the forward modelling reduces to solving the linear equation system:

$$M\vec{\bar{G}} = \vec{b}_s . \tag{4.43}$$

4.4 Discretisation of a 3-D Functional

For 3-D resistivity modelling, the subsurface geological model may be given over the domain: $(x,y,z)\in[x_1,x_{Nx}]\times[y_1,y_{Ny}]\times[0,z_0(x,y)]$, where the function $z_0(x,y)$ specifies the 3-D topography of the Earth's surface. We divide the rectangular xy-domain $[x_1,x_{Nx}]\times[y_1,y_{Ny}]$ into sequential rectangles $\Omega_{ij}:[x_i,x_{i+1}]\times[y_j,y_{j+1}]$ $(i=1,2,\ldots,Nx-1;\ j=1,2,\ldots,Ny-1)$ $(Nx,Ny\geq 2)$ in which the topography $z_0(x,y)$ is differentiable $z_0(x,y)\in C^1(\Omega_{ij})$. When the Variational Principle is applied to the 3-D problem as in equation (4.11), the volume integral can be calculated by summing the integrals over the rectangles:

$$\int_{\Omega} F(\boldsymbol{\sigma},G,\nabla G)\,d\Omega=\sum_{i=1}^{Nx-1}\sum_{j=1}^{Ny-1}\int_{x_i}^{x_{i+1}}\int_{y_j}^{y_{j+1}}\left[\int_{0}^{z_0(x,y)}F(\boldsymbol{\sigma},G,\nabla G)\,dz\right]dxdy \tag{4.44}$$

Following the same methodology as the 2.5-D case, we split the elevation $z_0(x,y)$ into $Nz-1$ $(Nz\geq 2)$ parts and equation (4.44) becomes

$$\int_{\Omega} F(\boldsymbol{\sigma},G,\nabla G)\,d\Omega=\sum_{i=1}^{Nx-1}\sum_{j=1}^{Ny-1}\sum_{k=1}^{Nz-1}\int_{x_i}^{x_{i+1}}\int_{y_j}^{y_{j+1}}\left[\int_{z_k(x,y)}^{z_{k+1}(x,y)}F(\boldsymbol{\sigma},G,\nabla G)\,dz\right]dxdy \tag{4.45}$$

Here $z_k(x,y)=z_0(x,y)(k-1)/(Nz-1)$. Then applying the coordinate maps

$$\begin{aligned} x(\xi) &= \frac{(x_{i+1}-x_i)}{2}\xi+\frac{(x_{i+1}+x_i)}{2}\\ y(\eta) &= \frac{(y_{j+1}-y_j)}{2}\eta+\frac{(y_{j+1}+y_j)}{2}\\ z(\xi,\eta,\zeta) &= \frac{(z_{k+1}(x,y)-z_k(x,y))}{2}\zeta+\frac{(z_{k+1}(x,y)+z_k(x,y))}{2} \end{aligned} \tag{4.46}$$

we have the following expression for the volume integral

$$\int_{x_i}^{x_{i+1}}\int_{y_j}^{y_{j+1}}\int_{z_k(x,y)}^{z_{k+1}(x,y)}F(\boldsymbol{\sigma},G,\nabla G)\,dxdydz=\int_{-1}^{1}\int_{-1}^{1}\int_{-1}^{1}F(\boldsymbol{\sigma},G,\nabla G)\left|\frac{\partial(x,y,z)}{\partial(\xi,\eta,\zeta)}\right|d\xi d\eta d\zeta \tag{4.47}$$

where

$$\frac{\partial(x,y,z)}{\partial(\xi,\eta,\zeta)}=\begin{vmatrix}\frac{\partial x}{\partial\xi} & \frac{\partial y}{\partial\xi} & \frac{\partial z}{\partial\xi}\\ \frac{\partial x}{\partial\eta} & \frac{\partial y}{\partial\eta} & \frac{\partial z}{\partial\eta}\\ \frac{\partial x}{\partial\zeta} & \frac{\partial y}{\partial\zeta} & \frac{\partial z}{\partial\zeta}\end{vmatrix}=\frac{1}{8(Nz-1)}(x_{i+1}-x_i)(y_{j+1}-y_j)z_0(x,y) \tag{4.48}$$

Applying Gaussian quadrature (Stroud & Secrest, 1966; Phillip and Rabinowitz, 1984) to equation (4.47), we obtain the following form:

$$\int_{x_i}^{x_{i+1}}\int_{y_j}^{y_{j+1}}\int_{z_k(x,y)}^{z_{k+1}(x,y)}F(\boldsymbol{\sigma},G,\nabla G)\,dxdydz$$

$$=\sum_{\alpha}^{N_\xi^i}\sum_{\beta}^{N_\eta^j}\sum_{\gamma}^{N_\zeta^k}\frac{(x_{i+1}-x_i)(y_{j+1}-y_j)z_0\left(x(\xi_\alpha),y(\eta_\beta)\right)}{8(Nz-1)}w_\alpha^i w_\beta^j w_\gamma^k F(\boldsymbol{\sigma},G,\nabla G)|_{(\xi_\alpha,\eta_\beta,\zeta_\gamma)} \tag{4.49}$$

The *w* terms are the Gaussian weights in each co-ordinate direction. Now, we turn to computing the integrand $F(\boldsymbol{\sigma},G,\vec{\nabla}G)$ at the Gaussian quadrature abscissae $(\xi_\alpha,\eta_\beta,\zeta_\gamma)$. Upon inspection of equation (4.46), the electric potential represented by the Green's function *G* is now mapped to the Gaussian quadrature space, e.g. $G=G\left(x(\xi),y(\eta),z(\xi,\eta,\zeta)\right)$. The differential chain rule provides the new partial derivatives:

$$\begin{aligned}\frac{\partial G}{\partial\xi} &= \frac{(x_{i+1}-x_i)}{2}\left[\frac{\partial G}{\partial x}+\frac{(\zeta+2k-1)}{2(Nz-1)}\frac{\partial z_0(x,y)}{\partial x}\frac{\partial G}{\partial z}\right]\\ \frac{\partial G}{\partial\eta} &= \frac{(y_{j+1}-y_j)}{2}\left[\frac{\partial G}{\partial y}+\frac{(\zeta+2k-1)}{2(Nz-1)}\frac{\partial z_0(x,y)}{\partial y}\frac{\partial G}{\partial z}\right]\\ \frac{\partial G}{\partial\zeta} &= \frac{z_0\left(x(\xi),y(\eta)\right)}{2(Nz-1)}\frac{\partial G}{\partial z}\end{aligned} \tag{4.50}$$

The derivatives with respect to the original coordinates (x,y,z) are thus:

$$\begin{aligned}
\frac{\partial G}{\partial x} &= \frac{2}{\left(x_{i+1}-x_i\right)}\frac{\partial G}{\partial \xi}-\frac{\left(\zeta+2k-1\right)}{z_0\left(x\left(\xi\right),y\left(\eta\right)\right)}\frac{\partial z_0\left(x,y\right)}{\partial x}\frac{\partial G}{\partial \zeta}\\
\frac{\partial G}{\partial y} &= \frac{2}{\left(y_{j+1}-y_j\right)}\frac{\partial G}{\partial \eta}-\frac{\left(\zeta+2k-1\right)}{z_0\left(x\left(\xi\right),y\left(\eta\right)\right)}\frac{\partial z_0\left(x,y\right)}{\partial y}\frac{\partial G}{\partial \zeta}\\
\frac{\partial G}{\partial z} &= \frac{2\left(Nz-1\right)}{z_0\left(x\left(\xi\right),y\left(\eta\right)\right)}\frac{\partial G}{\partial \zeta}
\end{aligned} \tag{4.51}$$

where G may be expressed by the Lagrange interpolation formula:

$$G\left(\xi,\eta,\zeta\right)=\sum_{p=1}^{N_\xi^i}\sum_{q=1}^{N_\eta^j}\sum_{v=1}^{N_\zeta^k}l_p\left(\xi\right)l_q\left(\eta\right)l_v\left(\zeta\right)G_{pqv} \tag{4.52}$$

Therefore, we have

$$\begin{aligned}
\left.\frac{\partial G}{\partial \xi}\right|_{\left(\xi_\alpha,\eta_\beta,\zeta_\gamma\right)} &= \sum_{p=1}^{N_\xi^i}l_p'\left(\xi_\alpha\right)G_{p\beta\gamma}\\
\left.\frac{\partial G}{\partial \eta}\right|_{\left(\xi_\alpha,\eta_\beta,\zeta_\gamma\right)} &= \sum_{p=1}^{N_\eta^j}l_q'\left(\eta_\beta\right)G_{\alpha q\gamma}\\
\left.\frac{\partial G}{\partial \zeta}\right|_{\left(\xi_\alpha,\eta_\beta,\zeta_\gamma\right)} &= \sum_{p=1}^{N_\zeta^k}l_v'\left(\zeta_v\right)G_{\alpha\beta v}
\end{aligned} \tag{4.53}$$

Substituting (4.53) for (4.51), we obtain the gradients

$$\begin{aligned}
\left.\frac{\partial G}{\partial x}\right|_{\left(\xi_\alpha,\eta_\beta,\zeta_\gamma\right)} &= \sum_{p=1}^{N_\xi^i}\frac{2l_p'\left(\xi_\alpha\right)}{\left(x_{i+1}-x_i\right)}G_{p\beta\gamma}-\sum_{v=1}^{N_\zeta^k}\frac{\left(\zeta_\gamma+2k-1\right)l_v'\left(\zeta_\gamma\right)}{z_0\left(x\left(\xi_\alpha\right),y\left(\eta_\beta\right)\right)}\frac{\partial z_0\left(x\left(\xi_\alpha\right),y\left(\eta_\beta\right)\right)}{\partial x}G_{\alpha\beta v}\\
&= \vec{N}_x^T\left(\xi_\alpha,\eta_\beta,\zeta_\gamma\right)\vec{G}^{(x)}
\end{aligned} \tag{4.54}$$

$$\begin{aligned}
\left.\frac{\partial G}{\partial y}\right|_{\left(\xi_\alpha,\eta_\beta,\zeta_\gamma\right)} &= \sum_{q=1}^{N_\eta^i}\frac{2l_q'\left(\eta_\beta\right)}{\left(y_{j+1}-y_j\right)}G_{\alpha q\gamma}-\sum_{v=1}^{N_\zeta^k}\frac{\left(\zeta_\gamma+2k-1\right)l_v'\left(\zeta_\gamma\right)}{z_0\left(x\left(\xi_\alpha\right),y\left(\eta_\beta\right)\right)}\frac{\partial z_0\left(x\left(\xi_\alpha\right),y\left(\eta_\beta\right)\right)}{\partial y}G_{\alpha\beta v}\\
&= \vec{N}_y^T\left(\xi_\alpha,\eta_\beta,\zeta_\gamma\right)\vec{G}^{(y)}
\end{aligned} \tag{4.55}$$

$$\left.\frac{\partial G}{\partial z}\right|_{(\xi_\alpha,\eta_\beta,\zeta_\gamma)} = \sum_{v=1}^{N_\zeta^k} \frac{2(Nz-1)l_v'(\zeta_\gamma)}{z_0\left(x(\xi_\alpha), y(\eta_\beta)\right)} G_{\alpha\beta v} = \vec{N}_z^T(\xi_\alpha,\eta_\beta,\zeta_\gamma)\vec{G}^{(z)} \tag{4.56}$$

where the vectors $\vec{N}_x, \vec{N}_y$ and $\vec{N}_z$ consist of the following components:

$$N_x(\xi_\alpha,\eta_\beta,\zeta_\gamma)_p = \begin{cases} \dfrac{2l_p'(\xi_\alpha)}{(x_{i+1}-x_i)} & \left(1 \le p \le N_\xi^i\right) \\ \dfrac{(\zeta_\gamma+2k-1)l_p'(\zeta_\gamma)}{z_0\left(x(\xi_\alpha), y(\eta_\beta)\right)} \dfrac{\partial z_0\left(x(\xi_\alpha), y(\eta_\beta)\right)}{\partial x} & \left(N_\xi^i \le p \le N_\zeta^k\right) \end{cases} \tag{4.57}$$

$$N_y(\xi_\alpha,\eta_\beta,\zeta_\gamma)_q = \begin{cases} \dfrac{2l_q'(\eta_\beta)}{(y_{j+1}-y_j)} & \left(1 \le q \le N_\eta^j\right) \\ \dfrac{(\zeta_\gamma+2k-1)l_q'(\zeta_\gamma)}{z_0\left(x(\xi_\alpha), y(\eta_\beta)\right)} \dfrac{\partial z_0\left(x(\xi_\alpha), y(\eta_\beta)\right)}{\partial y} & \left(N_\eta^j \le p \le N_\zeta^k\right) \end{cases} \tag{4.58}$$

$$N_z(\xi_\alpha,\eta_\beta,\zeta_\gamma)_v = \frac{2(Nz-1)l_v'(\xi_\gamma)}{z_0\left(x(\xi_\alpha), y(\eta_\beta)\right)} \quad \left(1 \le v \le N_\zeta^k\right) \tag{4.59}$$

The vectors $\vec{G}^{(x)}, \vec{G}^{(y)}, \vec{G}^{(z)}$ are given by

$$\begin{aligned} \vec{G}^{(x)} &= \vec{G}^{(\alpha)} \cup \vec{G}^{(\gamma)} \\ \vec{G}^{(y)} &= \vec{G}^{(\beta)} \cup \vec{G}^{(\gamma)} \\ \vec{G}^{(z)} &= \vec{G}^{(\gamma)} = \left\langle G_{\alpha\beta\gamma}, \gamma = 1,2,\ldots,N_\gamma^k \quad \forall \alpha,\beta \right\rangle \\ \vec{G}^{(\alpha)} &= \left\langle G_{\alpha\beta\gamma}, \alpha = 1,2,\ldots,N_\xi^i \quad \forall \beta,\gamma \right\rangle \\ \vec{G}^{(\beta)} &= \left\langle G_{\alpha\beta\gamma}, \beta = 1,2,\ldots,N_\eta^j \quad \forall \alpha,\gamma \right\rangle \end{aligned} \tag{4.60}$$

Once again, equations (4.54) and (4.55) indicate that the derivatives $\partial G/\partial x$ and $\partial G/\partial y$ require the slopes of the topography $\partial z_0(x,y)/\partial x$ and $\partial z_0(x,y)/\partial y$ in the sub-domain $[x_i, x_{i+1}]\times[y_j, y_{j+1}]$. Similarly, one can appropriately arrange the sub-domains

$\left[x_i, x_{i+1}\right]\times\left[y_j, y_{j+1}\right]$ in which the slopes exist. Accordingly, the volume integrand for 3-D resistivity modelling equation (4.11) may be written as follows:

$$\begin{aligned} F\left(\boldsymbol{\sigma}, G, \vec{\nabla} G\right)\Big|_{(\xi_\alpha,\eta_\beta,\zeta_\gamma)} = & \left[\sigma_{xx}\left(\frac{\partial G}{\partial x}\right)^2+\sigma_{yy}\left(\frac{\partial G}{\partial y}\right)^2+\sigma_{zz}\left(\frac{\partial G}{\partial z}\right)^2\right. \\ & \left. + \; 2\sigma_{xy}\frac{\partial G}{\partial x}\frac{\partial G}{\partial y}+2\sigma_{xz}\frac{\partial G}{\partial x}\frac{\partial G}{\partial z}+2\sigma_{yz}\frac{\partial G}{\partial y}\frac{\partial G}{\partial z}\right]_{(\xi_\alpha,\eta_\beta,\zeta_\gamma)} \end{aligned} \tag{4.61}$$

$$\begin{aligned} F\left(\boldsymbol{\sigma}, G, \nabla G\right) = & \left[\vec{G}^{(x)}\right]^T\left[\sigma_{xx}\vec{N}_x\vec{N}_x^T\right]\left[\vec{G}^{(x)}\right]_{(\xi_\alpha,\eta_\beta,\zeta_\gamma)} \\ & + \left[\vec{G}^{(y)}\right]^T\left[\sigma_{yy}\vec{N}_y\vec{N}_y^T\right]\left[\vec{G}^{(y)}\right]_{(\xi_\alpha,\eta_\beta,\zeta_\gamma)} \\ & + \left[\vec{G}^{(z)}\right]^T\left[\sigma_{zz}\vec{N}_z\vec{N}_z^T\right]\left[\vec{G}^{(z)}\right]_{(\xi_\alpha,\eta_\beta,\zeta_\gamma)} \\ & + \left[\vec{G}^{(x)}\right]^T\left[\sigma_{xy}\left(\vec{N}_x\vec{N}_y^T+\vec{N}_y\vec{N}_x^T\right)\right]\left[\vec{G}^{(y)}\right]_{(\xi_\alpha,\eta_\beta,\zeta_\gamma)} \\ & + \left[\vec{G}^{(x)}\right]^T\left[\sigma_{xz}\left(\vec{N}_x\vec{N}_z^T+\vec{N}_z\vec{N}_x^T\right)\right]\left[\vec{G}^{(z)}\right]_{(\xi_\alpha,\eta_\beta,\zeta_\gamma)} \\ & + \left[\vec{G}^{(y)}\right]^T\left[\sigma_{yz}\left(\vec{N}_y\vec{N}_z^T+\vec{N}_z\vec{N}_y^T\right)\right]\left[\vec{G}^{(z)}\right]_{(\xi_\alpha,\eta_\beta,\zeta_\gamma)} \end{aligned} \tag{4.62}$$

The cross-term outer-product vectors have been appended with zeros at the relevant indices in the computer code to make the derivative shape function vectors and Green's function value vectors commute and symmetric.

Substituting equation (4.62) into equation (4.49) yields

$$\int_{x_i}^{x_{i+1}}\int_{y_j}^{y_{j+1}}\int_{\frac{z_0(x,y)}{Nz-1}(k-1)}^{\frac{z_0(x,y)}{Nz-1}k} F\left(\boldsymbol{\sigma}, G, \nabla G\right)dxdydz = \sum_{\alpha=1}^{N_\xi^i}\sum_{\beta=1}^{N_\eta^j}\sum_{\gamma=1}^{N_\zeta^k}\left[\sum_{p,q=x,y,z}\left[\vec{G}^{(p)}\right]^T\left[w_{\alpha\beta\gamma}^{(pq)}\vec{N}_p\vec{N}_q^T\right]\left[\vec{G}^{(q)}\right]\right] \tag{4.63}$$

where

$$w_{\alpha\beta\gamma}^{(pq)} = \frac{\left(x_{i+1}-x_i\right)\left(y_{j+1}-y_j\right)z_0\left(x\left(\xi_\alpha\right), y\left(\eta_\beta\right)\right)}{8\left(Nz-1\right)}w_\alpha^i w_\beta^j w_\gamma^k\left(\sigma_{pq}\right)_{(\xi_\alpha,\eta_\beta,\zeta_\gamma)}$$

The boundary integral in equation (4.11) consists of the following five parts:

$$\int_{\Gamma} vG^2 d\Gamma = \left(\int_{x_1}^{x_{Nx}} \int_{0}^{z_0(x,y_1)} + \int_{x_1}^{x_{Nx}} \int_{0}^{z_0(x,y_{Ny})} + \int_{y_1}^{y_{Ny}} \int_{0}^{z_0(x_1,y)} + \int_{y_1}^{y_{Ny}} \int_{0}^{z_0(x_{Nx},y)} + \int_{x_1}^{x_{Nx}} \int_{y_1}^{y_{Ny}} vG^2 \right) d\Gamma \tag{4.64}$$

The surface integrals using the same (GQG) are:

$$\int_{x_1}^{x_{Nx}} \int_{0}^{z_0(x,y_1)} vG^2 dxdz = \sum_{i=1}^{Nx-1} \sum_{k=1}^{Nz-1} \left[\sum_{\substack{1\le\alpha\le N_\xi^i \\ 1\le\gamma\le N_\zeta^k}} \frac{\left(x_{i+1}-x_i\right) z_0\left(x\left(\xi_\alpha\right), y_1\right)}{4\left(Nz-1\right)} w_\alpha^i w_\gamma^k v_{\left(\xi_\alpha,\zeta_\gamma\right)} G_{\alpha 1\gamma}^2 \right] \tag{4.65}$$

$$\int_{x_1}^{x_{Nx}} \int_{0}^{z_0(x,y_{Ny})} vG^2 dxdz = \sum_{i=1}^{Nx-1} \sum_{k=1}^{Nz-1} \left[\sum_{\substack{1\le\alpha\le N_\xi^i \\ 1\le\gamma\le N_\zeta^k}} \frac{\left(x_{i+1}-x_i\right) z_0\left(x\left(\xi_\alpha\right), y_{Ny}\right)}{4\left(Nz-1\right)} w_\alpha^i w_\gamma^k v_{\left(\xi_\alpha,\zeta_\gamma\right)} G_{\alpha 1\gamma}^2 \right] \tag{4.66}$$

$$\int_{y_1}^{y_{Ny}} \int_{0}^{z_0(x_1,y)} vG^2 dzdy = \sum_{j=1}^{Ny-1} \sum_{k=1}^{Nz-1} \left[\sum_{\substack{1\le\beta\le N_\eta^j \\ 1\le\gamma\le N_\zeta^k}} \frac{\left(y_{j+1}-y_j\right) z_0\left(x_1, y\left(\eta_\beta\right)\right)}{4\left(Nz-1\right)} w_\beta^j w_\gamma^k v_{\left(\eta_\beta,\zeta_\gamma\right)} G_{1\beta\gamma}^2 \right] \tag{4.67}$$

$$\int_{y_1}^{y_{Ny}} \int_{0}^{z_0(x_{Nx},y)} vG^2 dzdy = \sum_{j=1}^{Ny-1} \sum_{k=1}^{Nz-1} \left[\sum_{\substack{1\le\beta\le N_\eta^j \\ 1\le\gamma\le N_\zeta^k}} \frac{\left(y_{j+1}-y_j\right) z_0\left(x_{Nx}, y\left(\eta_\beta\right)\right)}{4\left(Nz-1\right)} w_\beta^j w_\gamma^k v_{\left(\eta_\beta,\zeta_\gamma\right)} G_{1\beta\gamma}^2 \right] \tag{4.68}$$

$$\int_{x_1}^{x_{Nx}} \int_{y_1}^{y_{Ny}} vG^2 dydx = \sum_{i=1}^{Nx-1} \sum_{j=1}^{Ny-1} \left[\sum_{\substack{1\le\alpha\le N_\xi^i \\ 1\le\beta\le N_\eta^j}} \frac{\left(x_{i+1}-x_i\right)\left(y_{j+1}-y_j\right)}{4} w_\alpha^i w_\beta^j v_{\left(\eta_\beta,\zeta_\gamma\right)} G_{\alpha\beta 1}^2 \right] \tag{4.69}$$

Now all terms in the governing 3-D modelling problem, have been explicitly derived and defined and it is clear that upon substituting into equation (4.11), it reduces to the same quadratic form as in the 2.5-D modelling problem, i.e.

$$\Psi(\vec{G}) = \frac{1}{2}\vec{G}^T M\vec{G} - \vec{b}_s\vec{G} \tag{4.70}$$

According to the Variational Principle, $\delta\Psi = \langle \delta u, Du - f \rangle = 0$ and taking the differential of equation (4.70):

$$\begin{aligned} \delta\Psi(\vec{G}) &= \delta\left(\frac{1}{2}\vec{G}^T M\vec{G} - \vec{b}_s\vec{G}\right) \\ &= \frac{1}{2}\left(M\vec{G} + \vec{G}^T M\right) - b_s \\ &= M\vec{G} - b_s = 0 \end{aligned} \tag{4.71}$$

So again it reduces to solving the linear equation system

$$M\vec{G} = \vec{b}_s \tag{4.72}$$

4.5 The Partial Derivative Approximation Accuracy

The discretizations of 2-D and 3-D functionals described above required the gradient of the Green's functions $\vec{\nabla}\bar{G} = \left(\partial\bar{G}/\partial x, \partial\bar{G}/\partial z\right)$ and $\vec{\nabla}G = \left(\partial G/\partial x, \partial G/\partial y, \partial G/\partial z\right)$ to be discretised. These are crucial quantities for the numerical modelling. We may employ global or local Gaussian quadrature abscissae to calculate the functionals (2-D/3-D integrations) and the gradients.

Two examples of the two abscissae schemes in which we include an undulating surface topography in the model to take account of the skew are displayed (figure 4.2). In the spectral method, the global abscissae in each direction are employed in an orthogonal function series, such as Chebyshev or Fourier series, so as to achieve high accuracy of the derivatives, but it results in a full system matrix (Trefethen 2000) and is very expensive in terms of computer memory and time for large 3-D modelling.

In order to obtain a sparse matrix, we apply the global abscissae (figure 4.2a) to the integrations but calculate the gradient with the local cardinal functions obtained by the certain neighbouring points rather than the orthogonal function series. We still name it 'global scheme' to discriminate the 'local scheme' (figure 4.2b), which applies the Gaussian quadrature abscissae to both the integrations and gradients in the sub-domains that cover the

whole model and whose conductivity tensors are variable at point by point rather than being constant.

To assess the validity of the approximations made, we use a simple 2-D analytic example for the function $f(x, y) = A\cos(2\pi x / L_x)\sin(2\pi y / L_y)$. We include an undulating surface topography in the model to take account of the mis-alignment in the grid. Obviously the vertical derivatives $\partial f / \partial z$ should be easier to deal with because all GQG points align in a vertical direction at each horizontal position (figure 4.2). But the horizontal derivatives $\partial f / \partial x$ are more challenging because there is no horizontal alignment of grid points at any given depth. For the particular function in question, exact analytic solutions are available for the derivatives, which we can compare with the numerical derivatives.

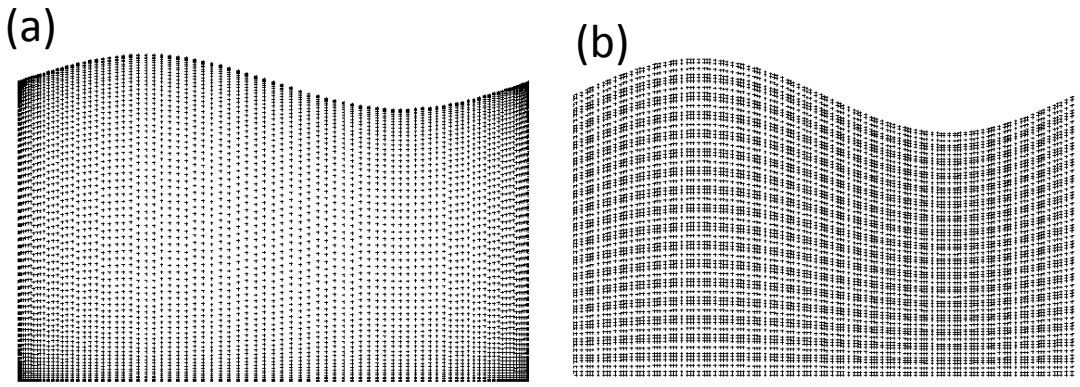

Figure 4.2. Gaussian quadrature grids for an undulating surface topography: (a) global scheme ($N_x = N_z = 2$, 151 and 76 abscissae in the *x*- and *z*-directions, 5 neighbouring points for the local cardinal function) and (b) local scheme ($N_x = 31$, $N_z = 17$, 5 abscissae in each direction in a sub-domain).

The upper panel in figure 4.3 shows the derivatives using the global scheme ($N_x = 2$, $N_z = 2$, the abscissae are equal to 151 and 76 in the *x*- and *z*-directions respectively, and the local cardinal functions of 5 neighbouring points to compute the derivatives). The bottom panel shows the absolute errors $|\varepsilon|$, which indicates at some points the relative error may be as large as 40%. They are worse for the *x* derivatives because of the staggering or misalignment associated with the surface topography and resultant co-ordinate stretching.

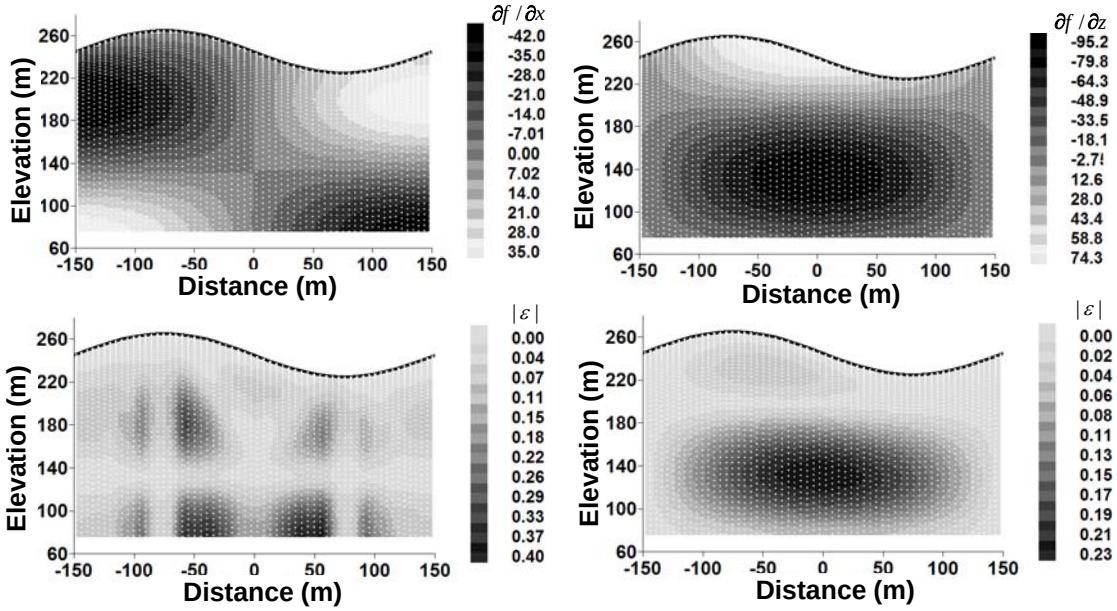

Figure 4.3. Approximations to the partial derivatives on the Gaussian quadrature grid using the global abscissae shown in Fig. 4.2a for a simple analytic case $f(x,z) = A\cos(2\pi x/L_x)\sin(2\pi z/L_z)$. The upper two diagrams show the numerical derivatives $\partial f/\partial x, \partial f/\partial z$ and the lower diagrams give the absolute errors |ε|. These errors are unacceptably large and so a global scheme is not satisfactory.

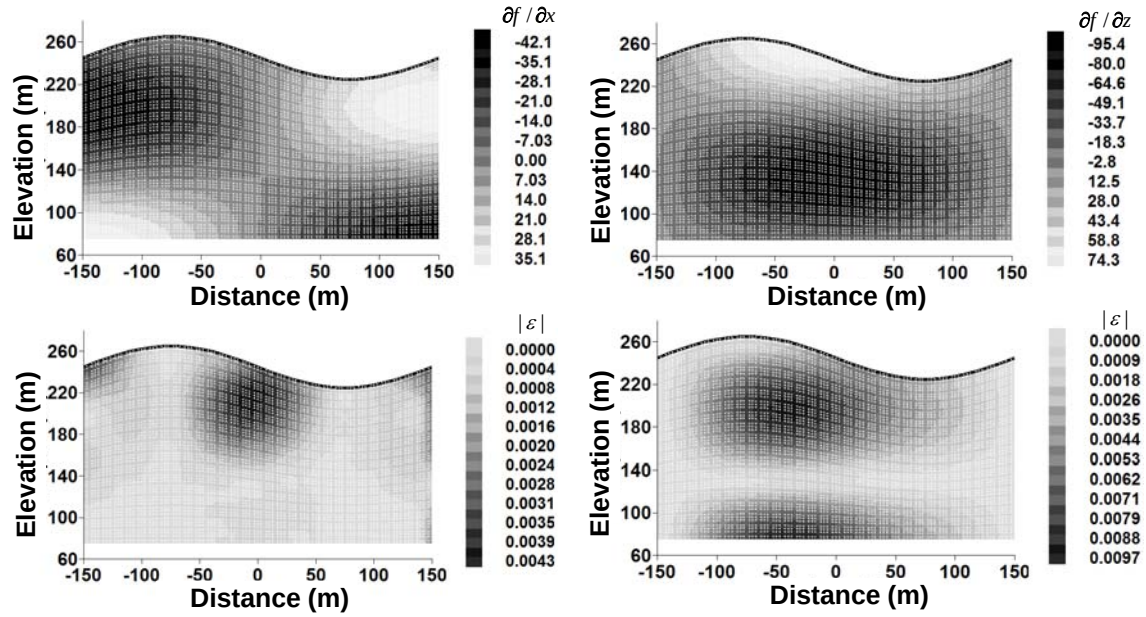

Figure 4.4 Approximations to the partial derivatives on the Gaussian quadrature grid using local scheme shown in Fig.2b for the same analytic example given in Fig 3. The errors (lower diagrams) in the numerical derivatives are now generally less than 0.5%.

We see from figure (4.4) the results using the local scheme (N_x = 30, N_z = 15 and 5 abscissae per 10 m). Again, both the actual computed derivatives and the absolute errors to the true solution are shown. The errors in this case are much reduced, and generally less than 1%. We have conducted tests for other topographies including a flat surface, a sloping interface and a trench using the same analytic expression. We find that the local scheme does quite a

good job (errors less than 1%) in all cases. From the spectral method theory (Trefethen 2000), it is not difficult to understand why the 'global scheme' is worse than the local scheme, because the neighbouring points for computing the derivatives in the global scheme are actually not the collocation points of the spectral method, but the Gaussian abscissae in the sub-domains.

4.6 Computational Aspects

We showed above that the GQG method gives rise to a system of linear equations:

$$\begin{aligned} 3-D: &\qquad M(\boldsymbol{\sigma})\vec{G} = \vec{b}_s \\ 2.5-D: &\qquad M(\boldsymbol{\sigma}, k_y)\vec{\vec{G}} = \vec{b}_s \end{aligned} \tag{4.73}$$

where $M(\boldsymbol{\sigma})$ or $M(\boldsymbol{\sigma}, k_y)$ is an $N \times N$ banded symmetric matrix depending on the conductivity tensor $\boldsymbol{\sigma}$ and the wavenumber k_y, $\vec{G}$ or $\vec{\vec{G}}$ is the N-component vector which gives the values of the Green's functions or the wavenumber version (Fourier transformed) of the Green's functions at all grid nodes, and $\vec{b}_s$ is the source vector which has zero components except for the current magnitude 1 at the current injection location(s). The potential U is simply related to the Green's function G through the relation $U = IG$, where I is the actual current magnitude. Here N is the dimension of the discrete model (total number of the Gaussian quadrature abscissae), and it may be as large as several hundred when tackling a 3-D problem.

Upon solving the linear equation system, one can obtain the potential values corresponding to a current injection point. Normally, electrical resistivity imaging surveys involve a large number of current electrode positions so that equation (4.73) may have to be solved hundreds of times.

In 3-D applications, an efficient and accurate linear equation solver is required. Zhou and Greenhalgh (2001) compared four iterative solvers based on the pre-conditioned conjugate gradient method and one matrix method (banded Cholesky decomposition) in terms of accuracy and efficiency and concluded that the two iterative solvers (symmetric successive over-relaxation algorithm, see Axelsson 1984; Spitzer 1995) and the incomplete Cholesky

decomposition algorithm, see David 1978; Ajiz and Jennings 1984; Manolis and Michael 1991; Zhang *et al*. 1995) are suitable options for 3-D modelling.

It has been shown (Zhou & Greenhalgh 2001) that in the 3-D FEM, if the tetrahedron elements are employed the non-zero elements in each row of the matrix **M** is 8, but from the previous formulation one can see that the GQG method (similar to the spectral element method) has in general more than 8 non-zero elements. This is because the minimum number of Gaussian quadrature abscissae is 2 (see equation 4.44). It means that if the dimension (*N*) is the same, the GQG method costs more computer memory and time, regardless of which solver is applied.

In 2.5-D applications, the banded Cholesky decomposition method $\left(M = \vec{L}\vec{L}^T\right)$ is commonly applied to the linear equation system. The advantage of the matrix method is that the decomposition is carried out only once for all the current electrodes. The cost of computer memory and time depend on the dimension (*N*) of the matrix **M** and its band-width $\left(N_{bw}\right)$. The smaller the band-width, the faster is the solving procedure. It is not difficult to show that the maximum band-widths of the FEM (triangular or rectangular elements) and the GQG method (similar to the spectral element method) can be estimated by $N_{bw}^{FEM} = \left[\max\left\{N_z\right\}+1\right]$ (Zhou & Greenhalgh 2000) and $N_{bw}^{GQG} = \left(N_\xi - 1\right)\left[\max\left\{N_z\right\}+1\right]$ (see equation 4.34), where N_z is the total number of nodes in the vertical direction and N_ξ is the number of the Gaussian quadrature abscissae in the x-direction of a sub-domain. Obviously, the 2.5-D GQG modelling costs more computer memory and time than the FEM because $N_\xi \geq 2$.

In addition, for efficiency and accuracy, limited wavenumbers are often employed and the choice of the limited wavenumbers includes determining the total number and the distribution in the range $k_y \in (0,\infty)$, as well as an appropriate interpolation of $\vec{\vec{G}}\left(k_y\right)$ for the inverse Fourier cosine transform. Theoretically, the more wavenumbers that are used, the more accurate the solution. From examinations of the analytic solutions for some simple models, i.e. half space, two layered model, or a vertical contact, the range of the wavenumber depends on the conductivity model and the spacing of the current and potential electrodes. In general, a small spacing requires a relatively large range of k_y and a large spacing needs a small range of k_y. Several schemes for choosing k_y and the interpolation for $\vec{\vec{G}}\left(k_y\right)$ have been

developed (Dey and Morrison 1979a; Queralt *et al*. 1991; LaBrecque *et al.* 1996; Xu *et al*. 2000). Actually, these schemes are all based on analytic solutions for the simple models due to the non-existence of any universal scheme to choose the wavenumbers for a general inhomogeneous model. Consequently, the computation errors for 2.5-D modelling are mainly contributed by using a limited set of wavenumbers, the discretization of the model, and the validity of the artificial mixed boundary condition. The analogous problem for 2.5-D acoustic modeling was recently investigated by Zhou and Greenhalgh (2006), who developed an adaptive wavenumber sampling scheme. Numerical experiments show that this approach can yield satisfactory results for even complex models.

After obtaining the Green's function *G***,** one can easily compute the apparent resistivity ρ_a for different electrode configurations by the following formula:

$$\rho_a = K\Delta G_{MN} \tag{4.74}$$

where K is the geometry factor for the specific electrode configuration, which only depends on the positions of the electrodes, and ΔG_{MN} is the potential difference between the two measuring electrodes. This normalised quantity is employed to indicate variation of the resistivity of the subsurface, i.e. departures from uniformity.

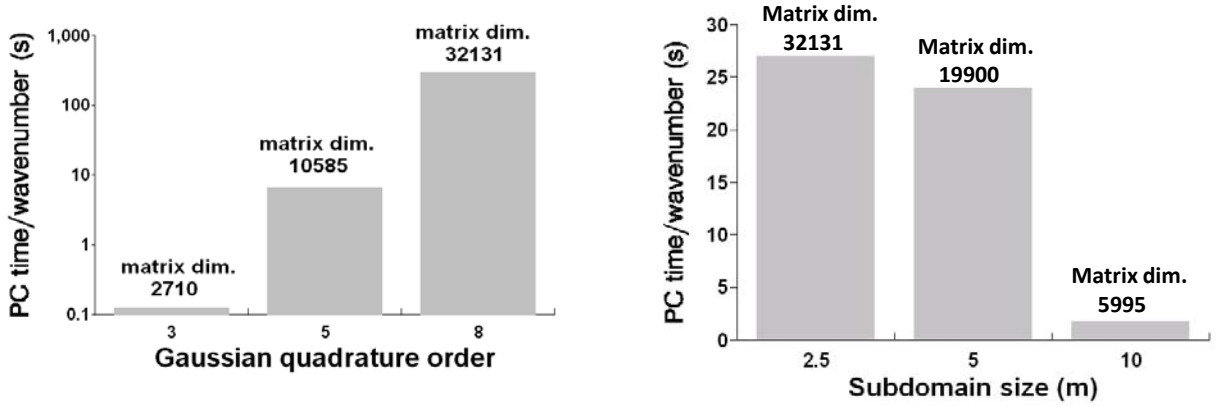

Figure 4.5. PC time costs of the linear equation solver (LL^T) per wavenumber (Pentium (R) M, 2GHz, 2GB RAM) for three Gaussian quadrature order and three sub-domain sizes applied to homogenous anisotropic modelling. Here the dimension of the system matrix is given for each case.

Experiments showing computer resources show that as the number of Gaussian quadrature abscissae increases, or the sub-domain size deceases, the computer time significantly increase, because the dimension of the matrix in the linear equation system (equation 4.43) and the

non-zero elements in each row of the matrix increase accordingly. Figure 4.5 shows the PC time (Pentium (R) M, 2GHz, 2GB RAM) costs for one wavenumber in these cases. Note the dramatic increase in the diagram from matrix dimension 2,710 (order 3) to dimension 32,131 (order 8) and over three orders of magnitude increase in the computation time. Also note that the size of 2.5m with order 3 has the same matrix dimension (32,131) as the size of 10m with order 8 and both give satisfactory results (see figure 4.5), but the former cost about 1/5 computer time of the latter, due to reducing the band width of the matrix with the low order. Therefore, there is a balance between the sub-domain size and the GQG order for the accuracy and efficiency. One must reach a compromise between them in any modelling.

Chapter 5
GQG Modelling Results

In this chapter I present results of numerical modelling for a variety of simplified geological models using the new GQG approach. The purpose is not only to validate the procedure but also to demonstrate its versatility in being able to handle complex surface topography and anisotropic structures. Both 2.5-D and 3-D models are considered. I begin by examining isotropic homogeneous models with and without variable topography. The former has a simple analytic solution for comparing with the numerical method in order to check accuracy. I then move on to consider 2.5-D heterogeneous isotropic models with both resistive and conductive anomalies. These solutions are compared against finite element results. Next I study an anisotropic homogeneous model without surface topography, for which an analytic solution exists for comparison. The next step is to consider heterogeneous 2.5-D models involving an anisotropic background medium with embedded resistive and conductive isotropic blocks. These models are extended to incorporate variable surface topography. Finally I present results of 3-D numerical modelling for both isotropic and anisotropic structures with variable topography. The former is compared against FE solutions. The chapter also includes an analysis of computational accuracy using different Gaussian orders and sub-domain sizes.

5.1 2.5-D Isotropic Homogeneous Models with Variable Topography

First we consider four homogeneous, isotropic models having a fixed resistivity of 10 Ω-m, but variable surface topographies. Figure 5.1 shows the actual models and the results obtained. The model domains of the GQGs are plotted as the backgrounds to the diagrams. The entire GQGs include the extended margins on both sides and the deeper part of the model to reduce the artificial boundary effects. The marginal parts are not depicted in all of the diagrams. The plots show the equipotential contours in the subsurface as vertical sections for each model, as well as the computed profiles of voltage versus distance along the ground surface. The diagram in the upper left is for a flat topography, which has an analytical solution. It is plotted against the GQG solution (figure 5.1). The error in the numerical solution is less than 0.85%. This occurs in the vicinity of the current source position. Next we show the results for a sloping surface topography (upper right). The GQG solution along the surface is compared with that obtained using a finite element algorithm (Zhou and

Greenhalgh 2000), where the sloping surface is approximated by a series of small vertical steps. Agreement between the two results is very good. The equipotential contours are quasi-circular but affected by the topography. The bottom two diagrams are for an undulating surface topography and a prominent trench or valley. The slight deviations between the FEM solutions and the GQGs' in the vicinity of the source are due to the errors in matching of the topography in the FEM code (Zhou, 1998). In each case one can see that the contours are roughly circular and all contours meet the surface topography at 90 degrees, implying tangential current flow here (the Neumann boundary condition $J_n = 0$).

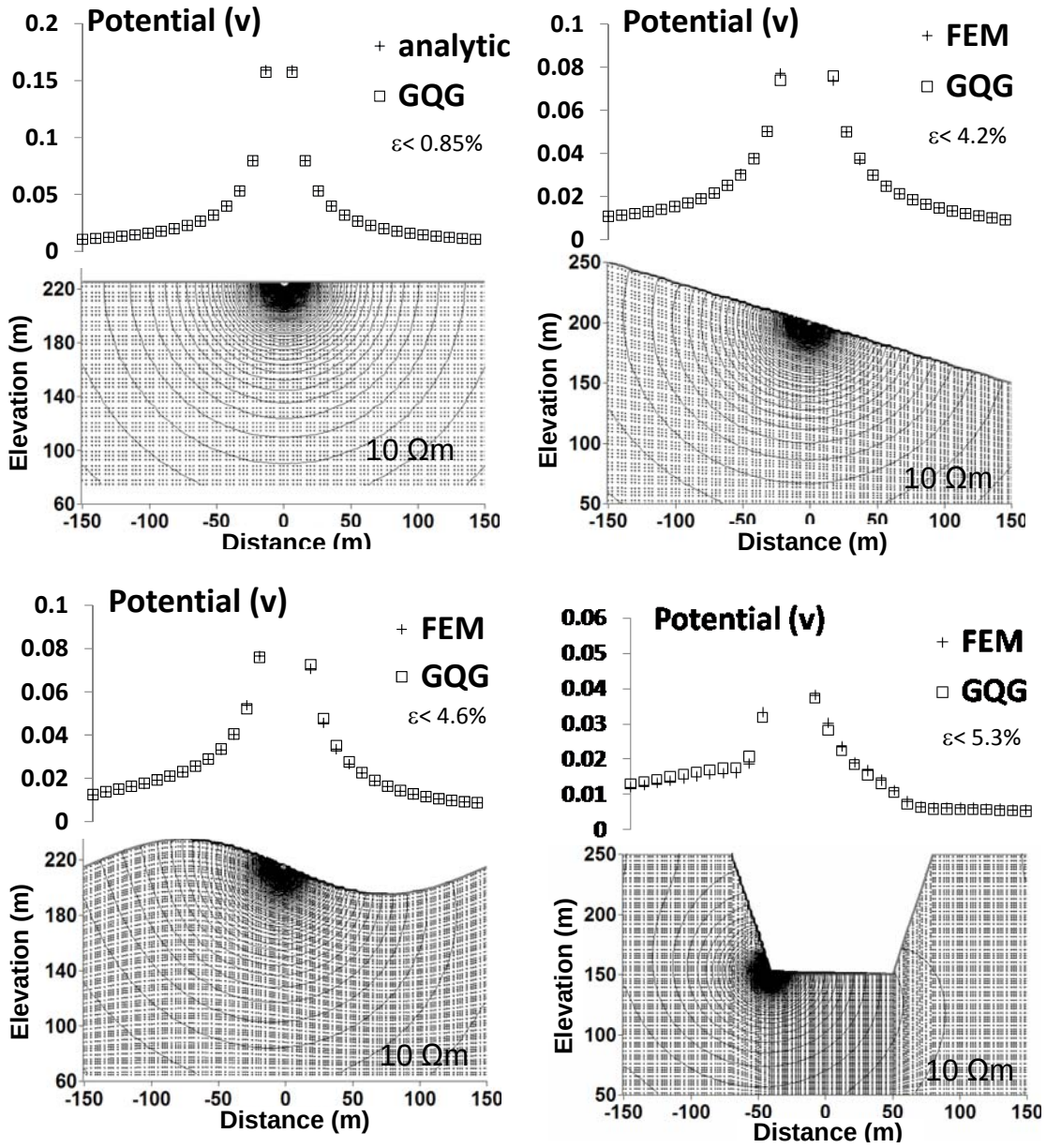

Figure 5.1. Results of GQG modelling of the electric response for four homogeneous, isotropic models (ρ = 10 Ω-m) but incorporating surface topography. Equipotential diagrams are shown in cross-section form along with surface voltage profiles. The surface profiles are compared against the analytic solution (flat topography case) and the finite element solutions (FEM) with the fine rectangular mesh. The slight deviations in vicinity of the source between the FEM solutions and the GQGs are due to the errors in matching of the topography in the FEM. The source is horizontally located at the origin for all but the trench model at x = - 40.

5.2 2.5-D Isotropic Heterogeneous Models with Variable Topography

The next set of GQG results are four inhomogeneous isotropic models (figure 5.2). The same topographic surfaces as before are used (flat, inclined, undulating valley) but now there are low and high resistivity anomalous bodies of 1 Ω-m and 500 Ω-m embedded within the background medium. The rectangular bodies are of approximate dimension 40 m. There is a clear distortion in the equipotential contours compared to the homogeneous case, with the equipotential lines being deflected away from the conductive body (current lines drawn in) and attracted towards the resistor (current lines deflected away).

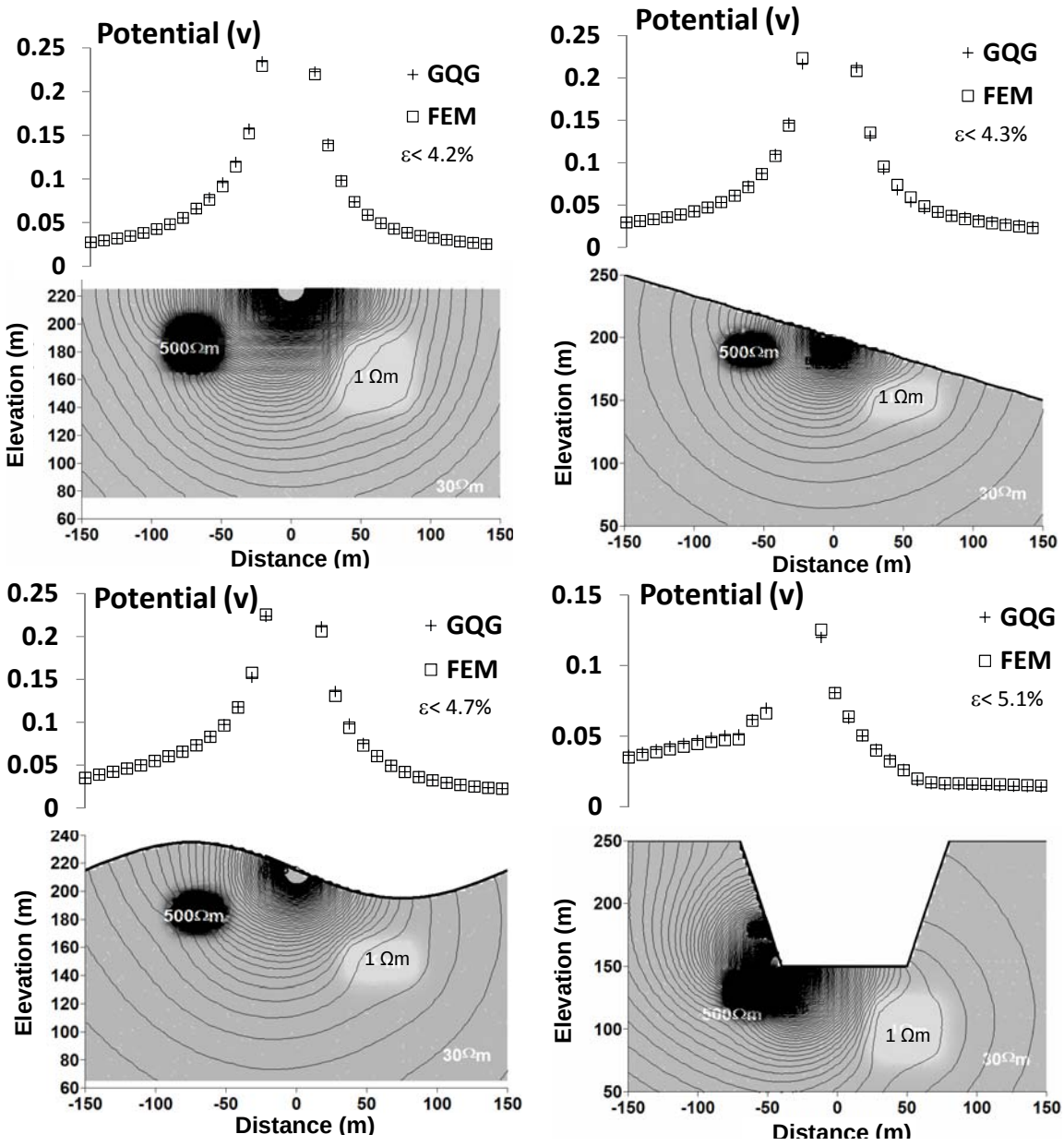

Figure 5.2. GQG modelling results for four heterogeneous, isotropic models, having the same topography as in previous models (Fig. 5) but now incorporating embedded low and high resistivity blocks(1 Ω-m and 500 Ω-m) in a background resistivity of 30 Ω-m. Note the distortion of the equipotentials around the anomalous bodies. The surface voltage profiles are compared against the finite element modelling results and found to be comparable. The source is horizontally located at the origin for all but the trench model at x = - 40.

Figure 5.2 also shows the surface voltage profiles obtained with each model. A comparison of the results obtained is made using a FEM program that uses very small steps which match the surface topography. There is good agreement in each case, as can be clearly seen.

5.3 2.5-D Anisotropic Homogeneous Models with Flat Surface Topography

Analytic solutions exist for the potential at the surface of a uniform, tilted transversely isotropic half space having a flat surface (Bhattacharya & Patra 1968; eq. 2.35). Analytic solutions also exist for the potential in the subsurface of a uniform tilted transversely isotropic half space having a flat surface (Li & Spitzer 2005). The next six figures display the electric potential obtained for a uniform TTI flat surface model with three different dips of the symmetry axis: 30°, 45° and 60° (measured from the horizontal). The coefficient of anisotropy is $\lambda = 3.16$. This is really quite a large value and therefore represents a fairly severe case. The current injection point is at the origin.

The following three even numbered figures (figures 5.4, 5.6, 5.8) have the analytic solutions superimposed on the horizontal and vertical profiles. The surface potential is compared and displayed in the top panel, extracted out of the numerical solution at 10m intervals. The subsurface potentials are compared at the GQG points with the analytical solution at three fictitious boreholes horizontally offset by 25m either side of the source and directly below the source.

The following three odd numbered figures (figures 5.5, 5.7, 5.9) display the GQG potential colour image and corresponding contours for these models. For the GQG solution, the subdomain Ω_{ij} size is $5m^2$ with a quadrature order of 5, such that there are 25 nodes in each inner element subdomain Ω_{ij}. The bi-variate Shepard interpolant (Shepard, 1968) with a search window size of $4m^2$ is used to generate a regular mesh with a cell dimension of 1.003345m x 1.006711m in the x and z directions respectively. A further mesh refinement to 0.2m x 0.2m with a bi-linear interpolant is then invoked to increase the resolution of the following images. The following Matlab images and contours require a regular grid and are just a guide as to the general shape of the situation being investigated. The surface potentials are exact as they coincide with the GQG solution mesh. The image colour is scaled to display

potential (0.04:1.0) [V] in the wavenumber~offset confidence range $k_y^R = (\pm 10m, \pm 150m]$. The potentials are calculated and displayed in the plane normal to strike, i.e. y = 0.

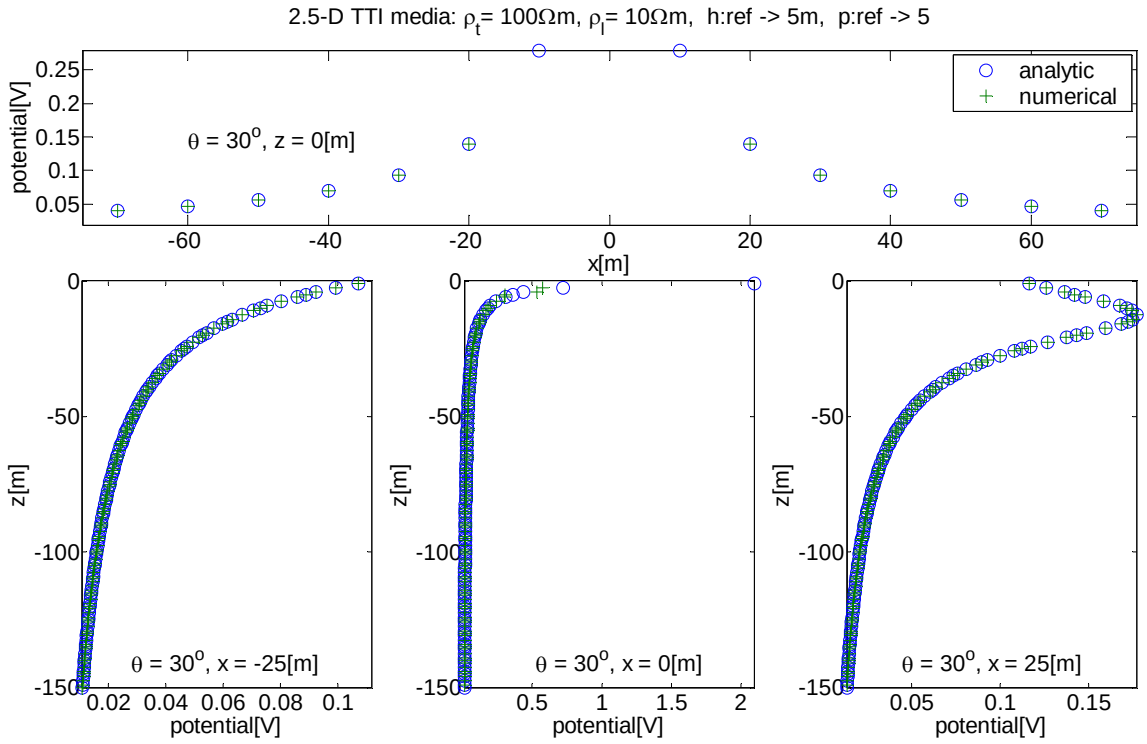

Figure 5.4 The electric potential in a uniform TTI medium with a flat surface and dip 30^0.

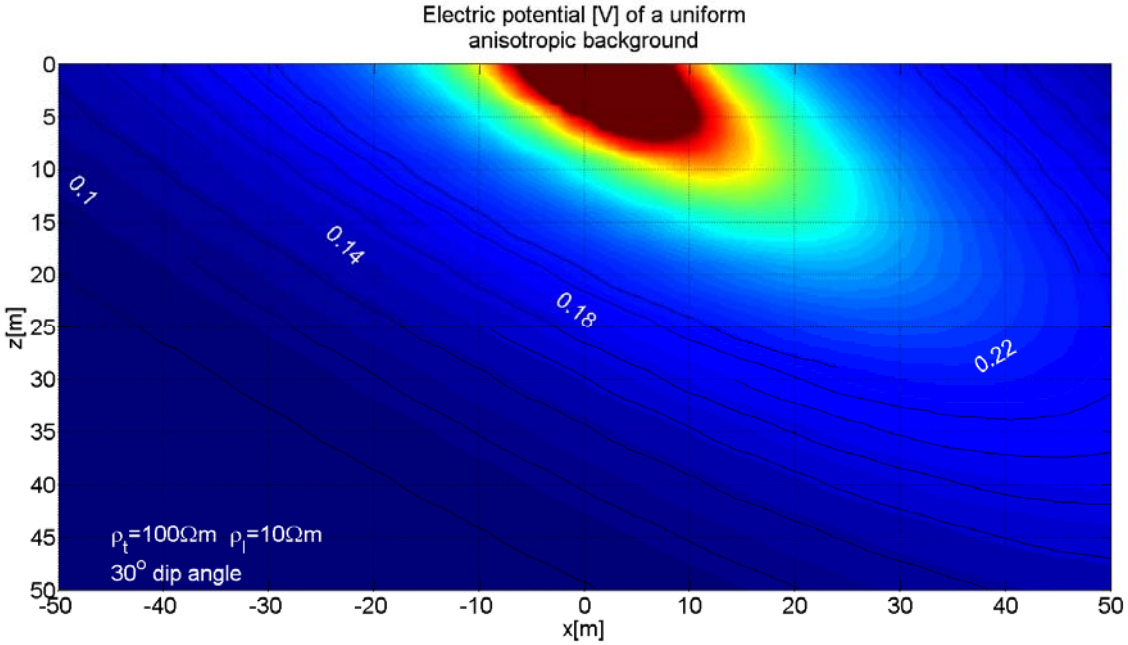

Figure 5.5 The GQG numerical solution for the subsurface potential in a uniform TTI medium with a flat surface and dip 30^0.

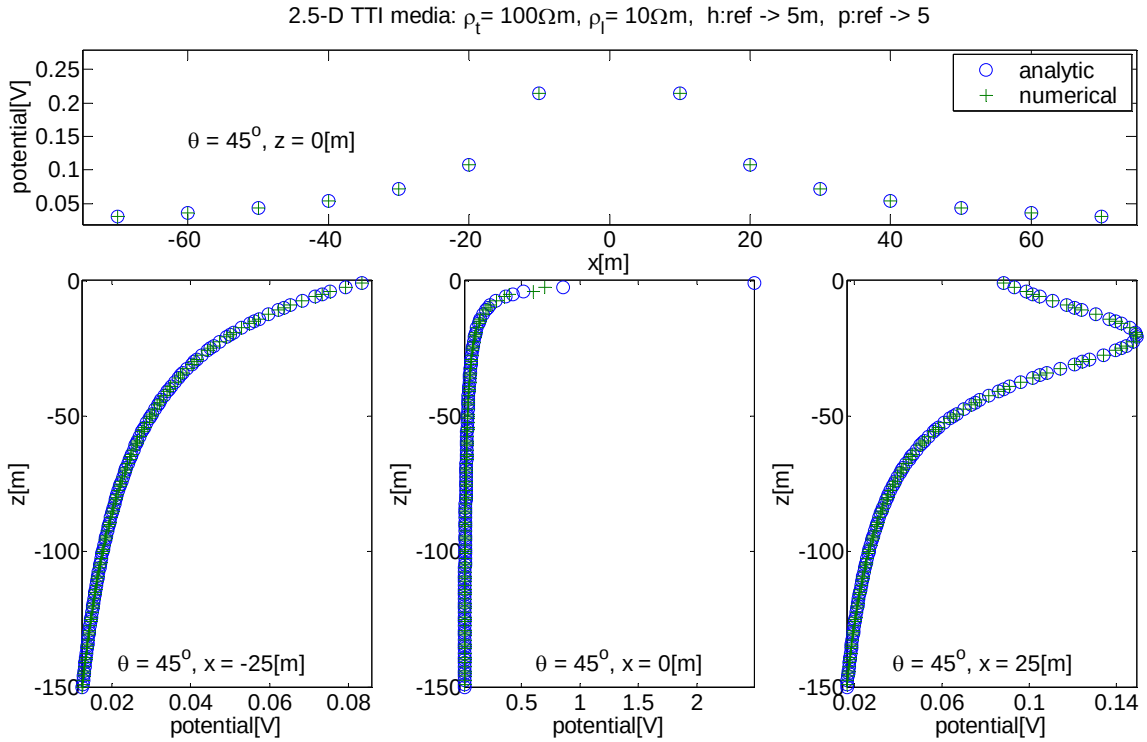

Figure 5.6 The electric potential in a uniform TTI medium with flat surface and dip 45^0.

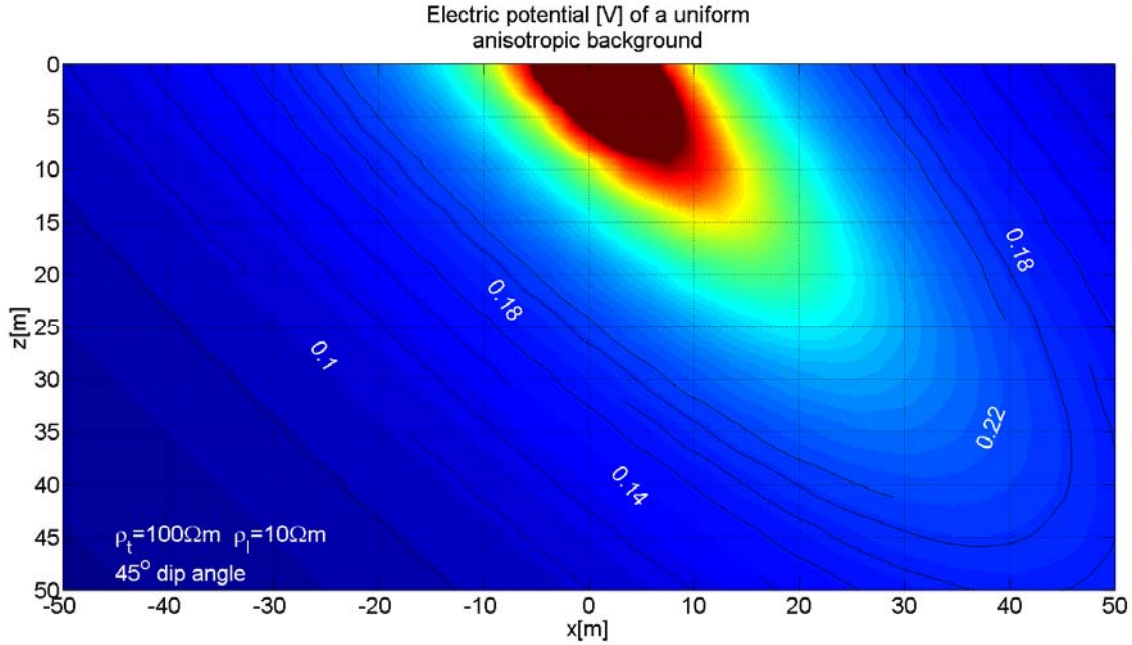

Figure 5.7 The GQG numerical solution for the subsurface potential in a uniform TTI medium with a flat surface and dip 45^0.

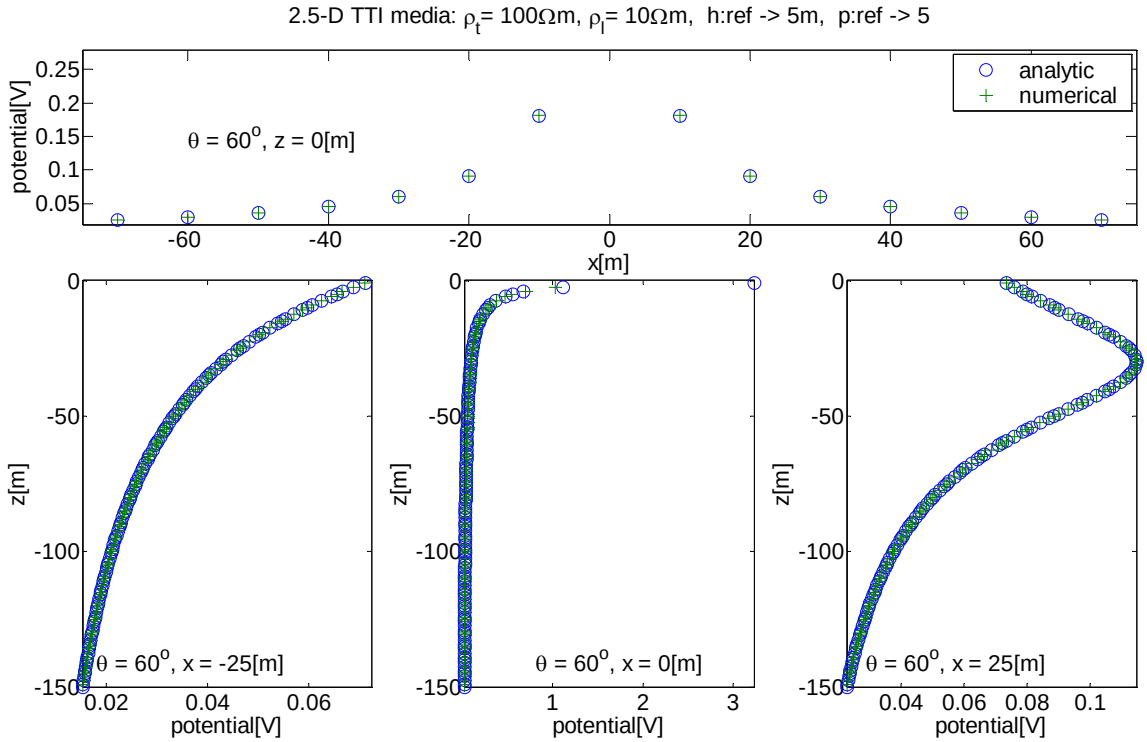

Figure 5.8 The electric potential in a uniform TTI medium with a flat surface and dip 60^0.

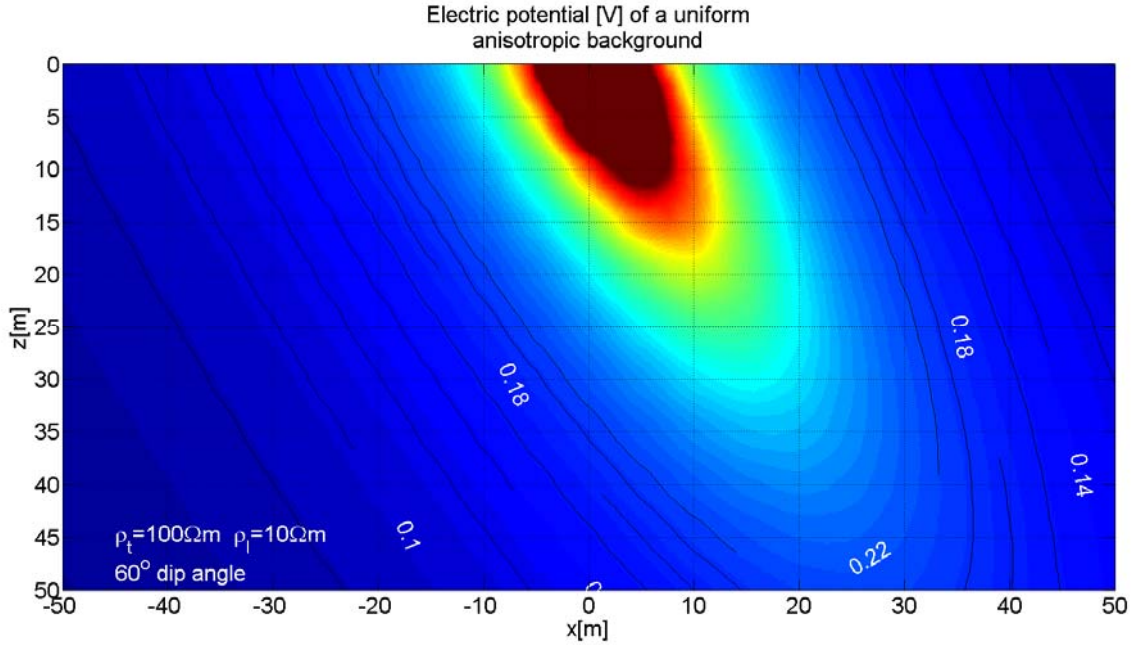

Figure 5.9 The GQG numerical solution for the subsurface potential in a uniform TTI medium with a flat surface and dip 60^0.

The potential contour sections in figures 5.5, 5.7, 5.9 clearly show the elliptic patterns with the long axis pointing in the direction of the bedding plane (or longitudinal direction). Note how the elliptical patterns steepen as the dip of the plane of stratification (measured from the horizontal) increases.

The next three figures (5.10, 5.11 and 5.12) show the results of experimenting with different sub-domain sizes and different orders of the GQG method for the same uniform TTI models for the three dip angles. The horizontal and vertical profiles now display the absolute relative error against the exact analytic solution. There are two sub-domain sizes: 5m x 5m and 10m x 10m. For these two sub-domain sizes, there are two orders: 3 and 5 quadrature points in each dimension so that a sub-domain contains either 9 or 25 nodes. Clearly, except near the source, the errors are within acceptable limits (< 1%) in all cases, and even near the source the errors significantly decrease when the model domain discretization is denser.

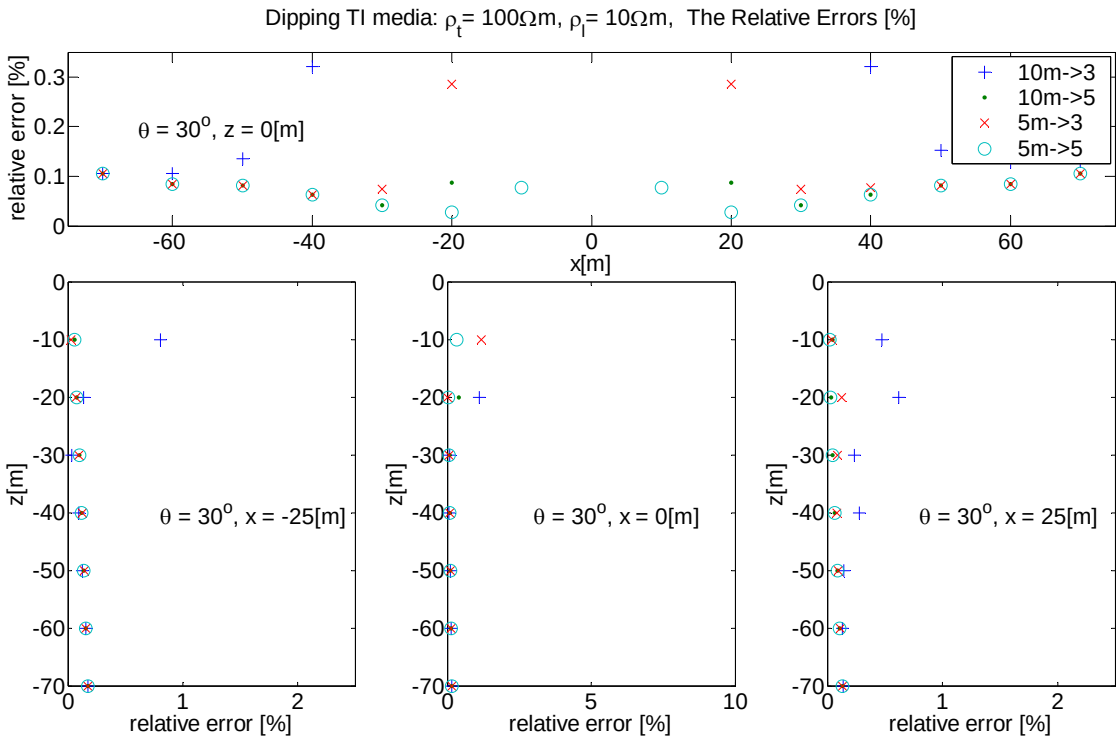

Figure 5.10 The relative errors for the GQG numerical solutions in a uniform TTI medium with a regular boundary, at 10m intervals for different p- and h- refinements. The 5m x 5m patches with 5x5 quadrature points, has the best accuracy nearest the source.

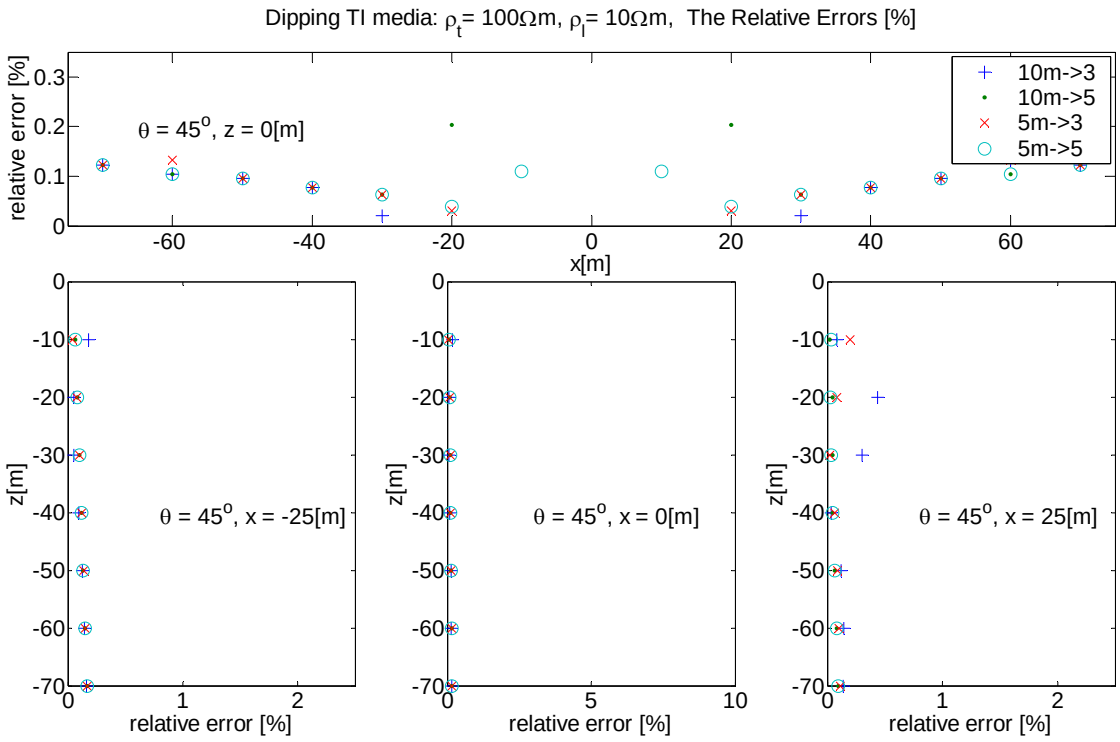

Figure 5.12 The relative errors for the GQG numerical solutions in a uniform TTI medium with a regular boundary, at 10m intervals for different p- and h- refinements. The 5m x5m patches with 5x5 quadrature points, has the best accuracy nearest the source.

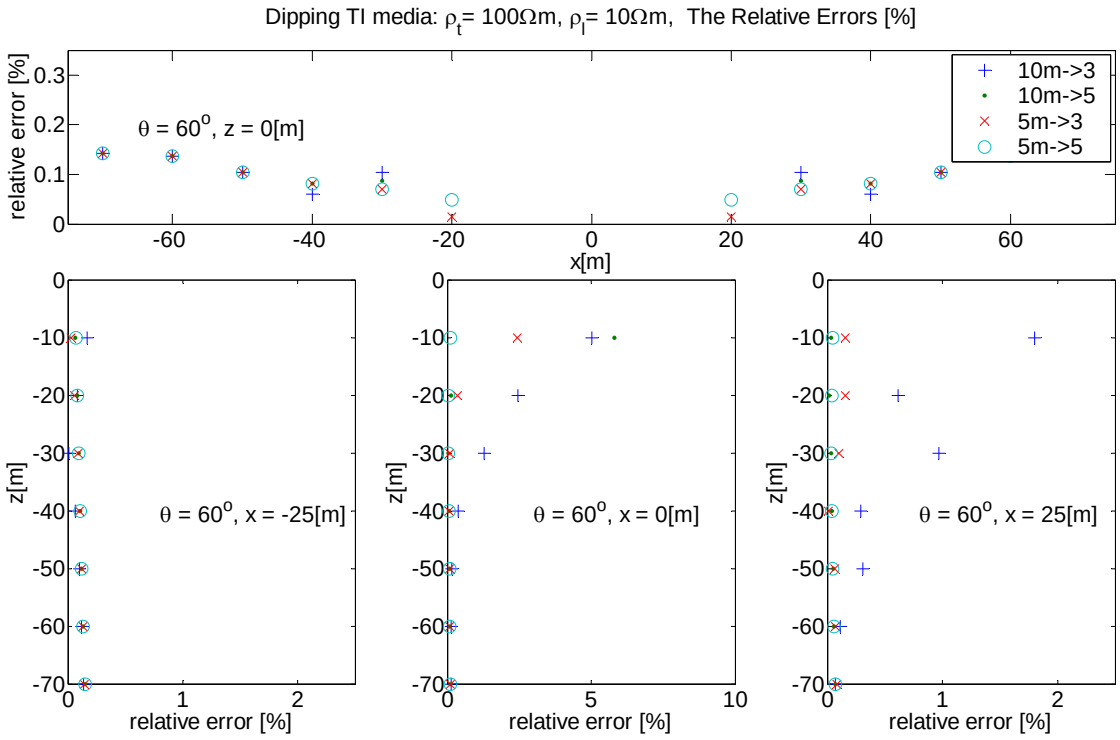

Figure 5.14 The relative errors for the GQG numerical solutions in a uniform TTI medium with a regular boundary, at 10m intervals for different p- and h- refinements. The 5m x 5m patches with 5x5 quadrature points, has the best accuracy nearest the source.

The next issue addressed is how the accuracy is affected by the choice of sub-domain size and the choice of quadrature order. This problem is known as that of h-refinement and p-refinement respectively in the finite element literature. The spectral method tells us that the clustered set of points described by the zeros of the Legendre polynomial results in the optimal configuration of nodes at which to evaluate the derivative. Intuitively, by the reasoning of spectral theory and Gaussian quadrature theory, it would seem that a more accurate solution could be achieved by increasing the size of the subdomains and allowing the abscissae to have a better clustering.

By using approximately the same number of nodes in two different configurations, i.e. with 10m sub-domains and 9 Gaussian pts and 5m subdomains and 5 Gaussian pts per dimension, (see figure (5.15) a comparison of mesh accuracy was investigated. The resulting relative errors are plotted in figure (5.16) for a uniform TTI model having a dip of 30^0. As seen in figure 5.16, the 5m – 5pts achieves a better accuracy near the source.

The derivative of the solution should be smooth in spectral element theory. It was shown before in equation (4.14) that for a uniform TTI medium, the analytic solution for the DC electric problem is a scaled McDonald function. So, for this electrostatic problem, it appears that the smaller subdomain size helps in damping the source singularity potential artefact since the neighbouring subdomains (that cover the same area as the larger subdomain size), have partial derivative Lagrangian interpolants that are independent of the source node that is present in the larger subdomain size, i.e. 10m – 9pts (see figure 5.15).

Besides this and the choice of wavenumer sampling range (Zhou 2006) another reason why the 5m – 5 pts achieves better accuracy is that there are fewer nodes near the singularity than for the 10m – 9 pts. In general, a boundary value problem should have the source inside the boundary, but for surface surveys in DC resistivity, this is not the case. Also the source is described by a Dirac delta distribution which is not mathematically satisfactory for the Poisson equation. One additional reason for error besides round-off is that the coordinate transformation used to map the physical coordinates to a quadrature space is not conformal and the preservation of derivatives under the described mapping can not be guaranteed. But since the weak form of solution is found with the Variational Principle or Galerkin solution, this is of limited value. The Lagrange polynomials used as the shape functions could be modified for the boundary elements to satisfy the boundary conditions. This could be achieved using Hermite polynomials (Weideman, Reddy, 2001), but since the potential is very small on the extended subsurface boundaries, this does not seem necessary. The only argument is that the boundary nodes are located on the diagonal of the system matrix which is the dominant influence when inverting.

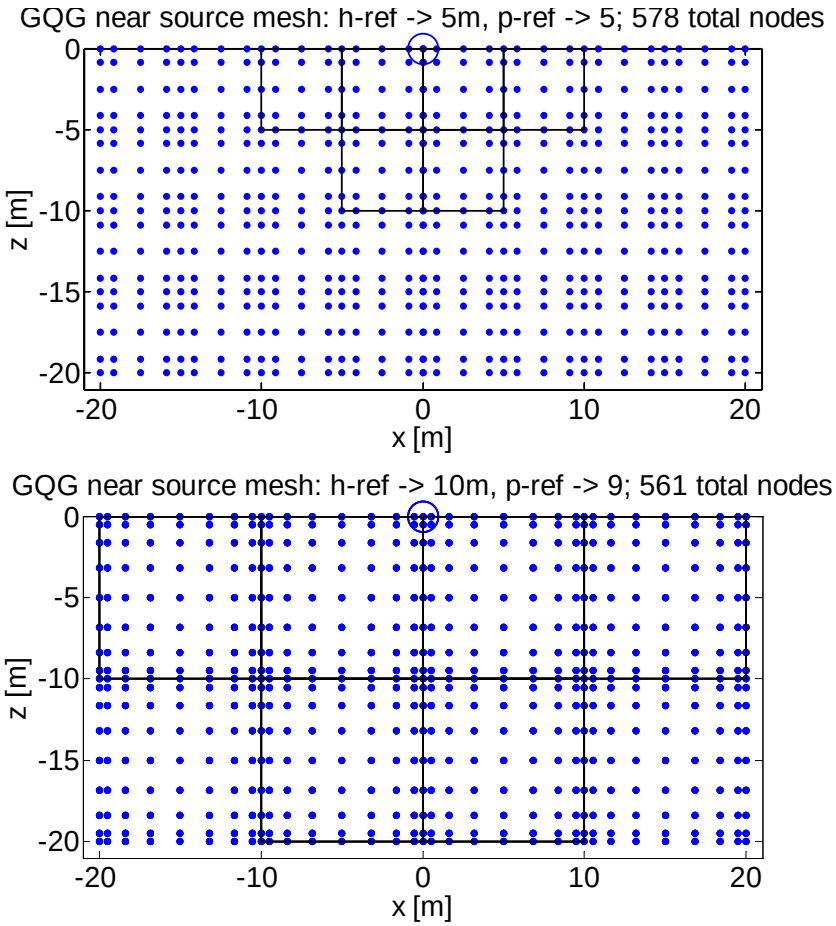

Figure 5.15 The two different p- and h- refinements. The 5m x 5m patches with 5x5 quadrature points, has the best accuracy nearest the source since the smaller patches help reduce the source singularity influence on the partial derivative approximations.

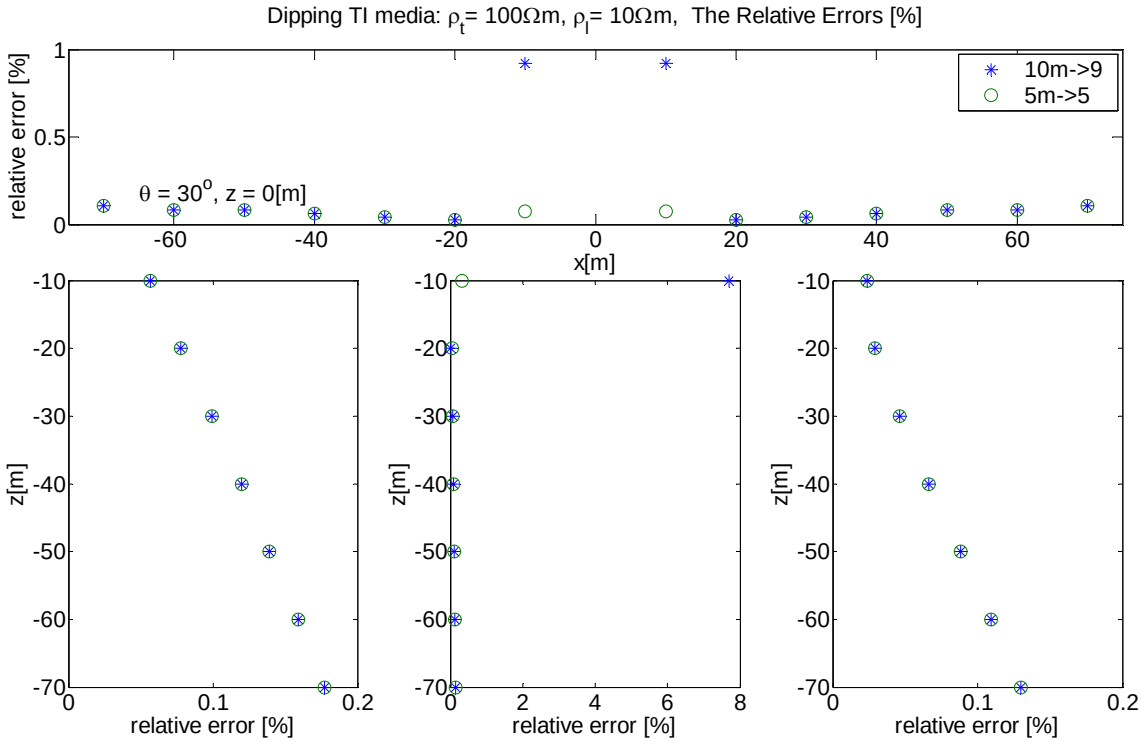

Figure 5.16 The relative errors sifted out of the GQG numerical solutions in a uniform TTI medium with a regular boundary, at 10m intervals for the two different p- and h- refinements. The 5m x 5m patches with 5x5 quadrature points, has the best accuracy nearest the source.

5.4 2.5 D Anisotropic Heterogeneous Models with Flat Surface Topography

The next class of model investigated was that of a TTI background medium, but this time with a dominant inhomogeneity present. The surface topography is flat. Figures 5.17 and 5.18 illustrate the subsurface electric potential for a TTI medium with a dip angle of 30^0 with the same coefficient of anisotropy as the previous uniform models, i.e. $\lambda = 3.16$. However this time there is a conductive (figure 5.17) and resistive (figure 5.18) anomaly buried 10m below the source and having dimensions 10m x 10m. Comparison with figure 5.5 (same anisotropic model but homogeneous) shows that the current penetrates deeper in the conductor model and the current remains in the shallower region in the resistor model. This is also evident in the surface potential profiles in figure 5.19.

Bhattacharya & Patra (1968) show that the surface potential in the x – z plane (y = 0) of a uniform TTI medium is symmetric about the source point. Figure 5.19 illustrates the asymmetry of the surface potential for the TTI heterogeneous model. Figure 5.20 shows the differences in potential for these heterogeneous models with respect to the uniform TTI model. Such voltage differences are in the detectable range, and so we conclude that these two highly artificial anomalous bodies are resolvable in a TTI medium.

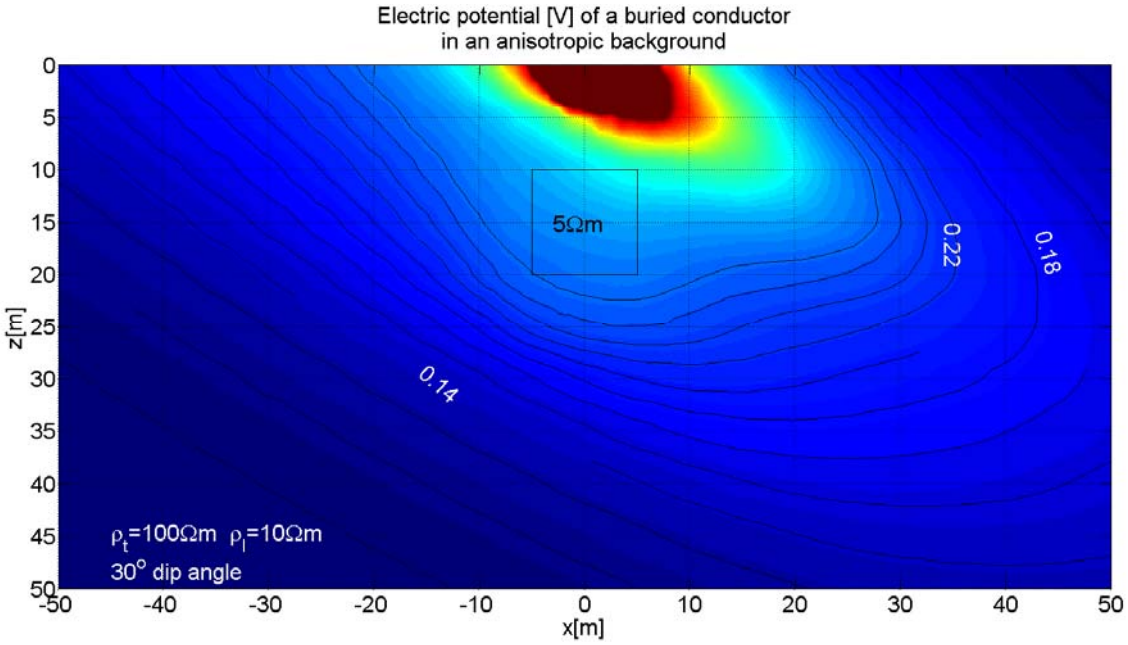

Figure 5.17 The GQG numerical solution for the subsurface potential in an inhomogeneous (buried conductor), TTI medium with a flat surface.

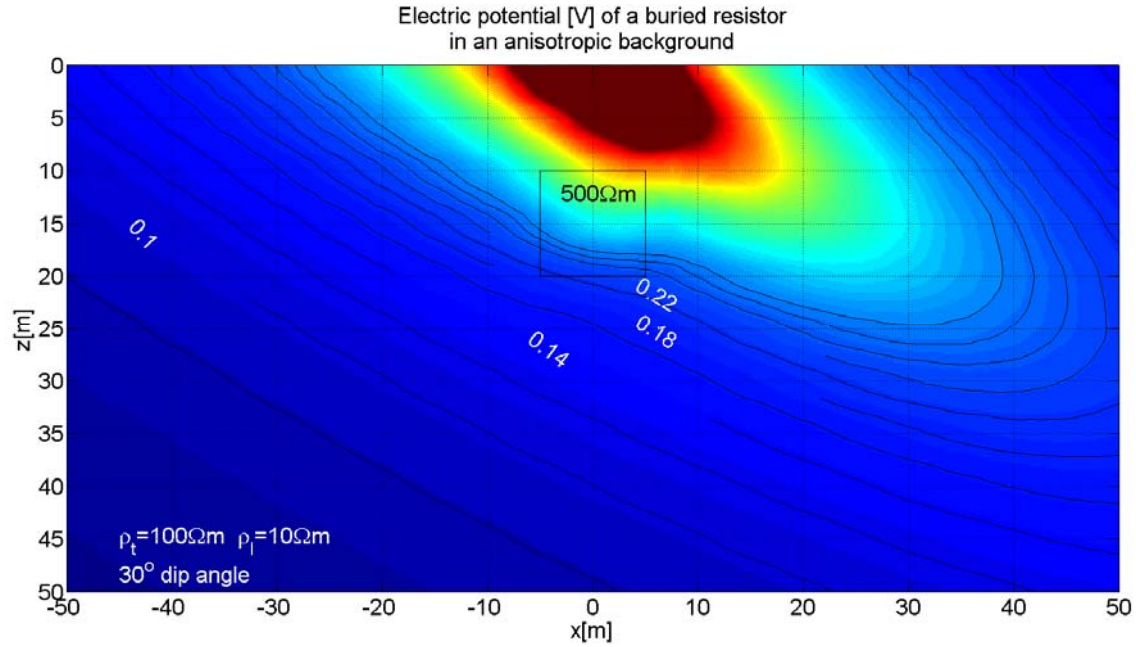

Figure 5.18 The GQG numerical solution for the subsurface potential in an inhomogeneous (buried resistor), TTI medium with a flat surface.

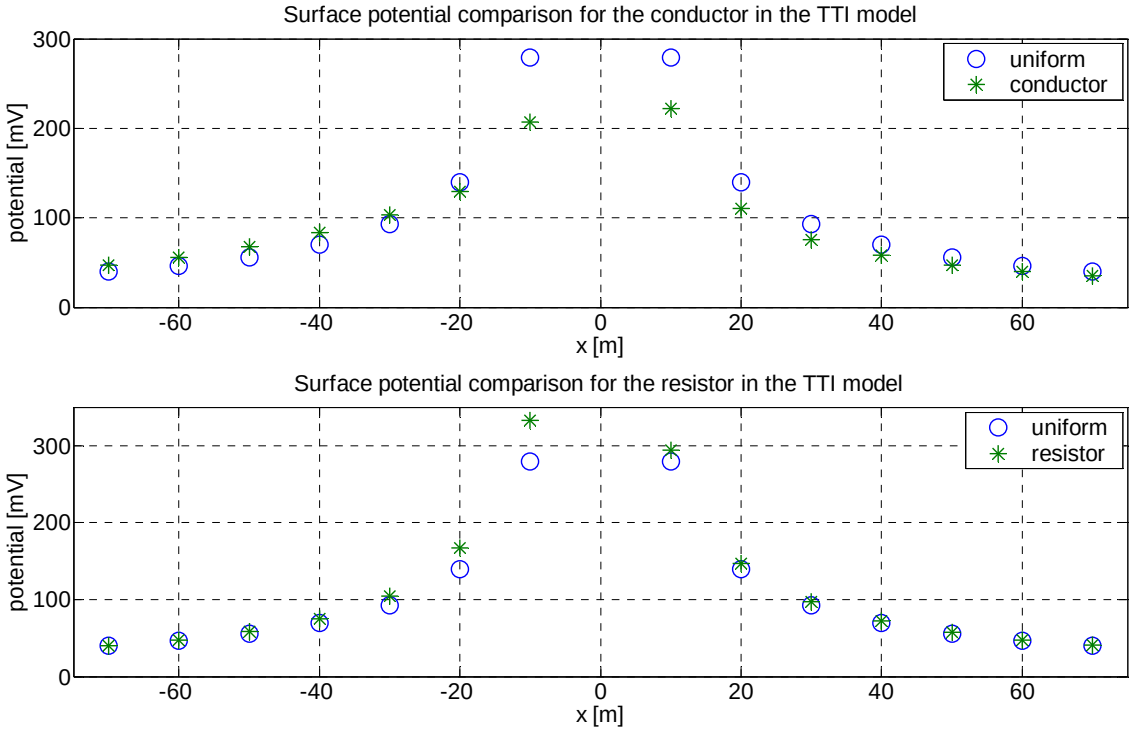

Figure 5.19 A comparison of the GQG surface potentials for the conductor and resistor models in a TTI medium with a flat surface.

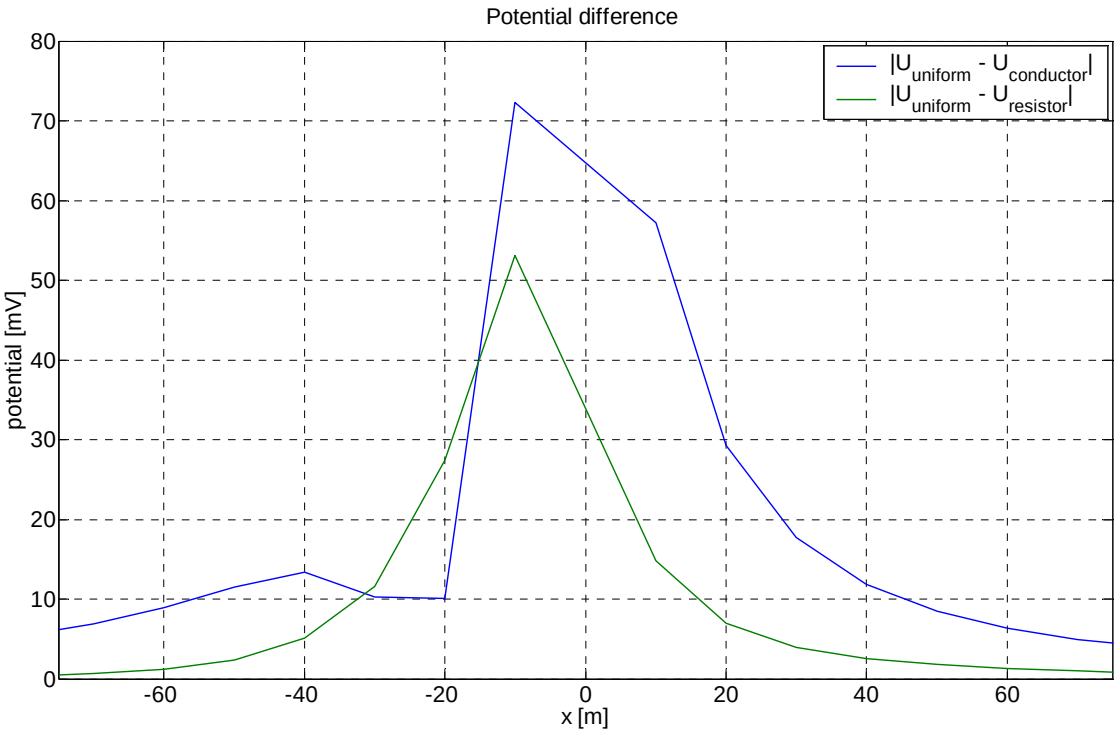

Figure 5.20 A comparison of the GQG surface potential differences for the conductor and resistor models in a TTI medium with a flat surface.

5.5 2.5-D Anisotropic Heterogeneous Models with Variable Topography

In this section, the two topographies investigated are the sinusoidal type (valley and hill feature, or undulating topography) and trench (cliff) type. Both topographic types have the same underlying TTI medium as for the previous flat surface models, i.e. $\rho_t = 100\Omega m$, $\rho_l = 10\Omega m$ and a dip angle of 30^0. Also, the same heterogeneities are incorporated, i.e. the shallow buried conductor and resistor. Before progressing it should be noted that it is not possible to compare the models in this section with results from FE modelling because our FEM code does not at the time of writing include electrical anisotropy. Li and Spitzer (2006) have performed 3D azimuthal electrical anisotropic modelling with the FEM.

First the undulating topographic models are considered. The source is located at the surface with position $(x, z) = (0, -20)$, which corresponds with the inflection point of the sinusoidal surface. Figure 5.21 displays the uniform TTI media described above. This is a good reference model to compare the more complicated potential contours of the conductor and resistor models against, at least qualitatively (as shown above). It is interesting to compare this model with that of the flat surface model, viz. figure 5.5. There is no longer a surface potential symmetry evident. For example, it is observed in figure 5.21 that the 0.22V and 0.14V equipotential contours are shallower than the flat surface equivalent contours. They

are also stretched laterally to the left (top of hill) by approximately twice that to the right (bottom of valley). This asymmetry is also seen in the surface potential plot in figure 5.24 for the uniform plot denoted 'o'. The potentials to the right of the source are less than their equivalent x direction offset counterparts to the left.

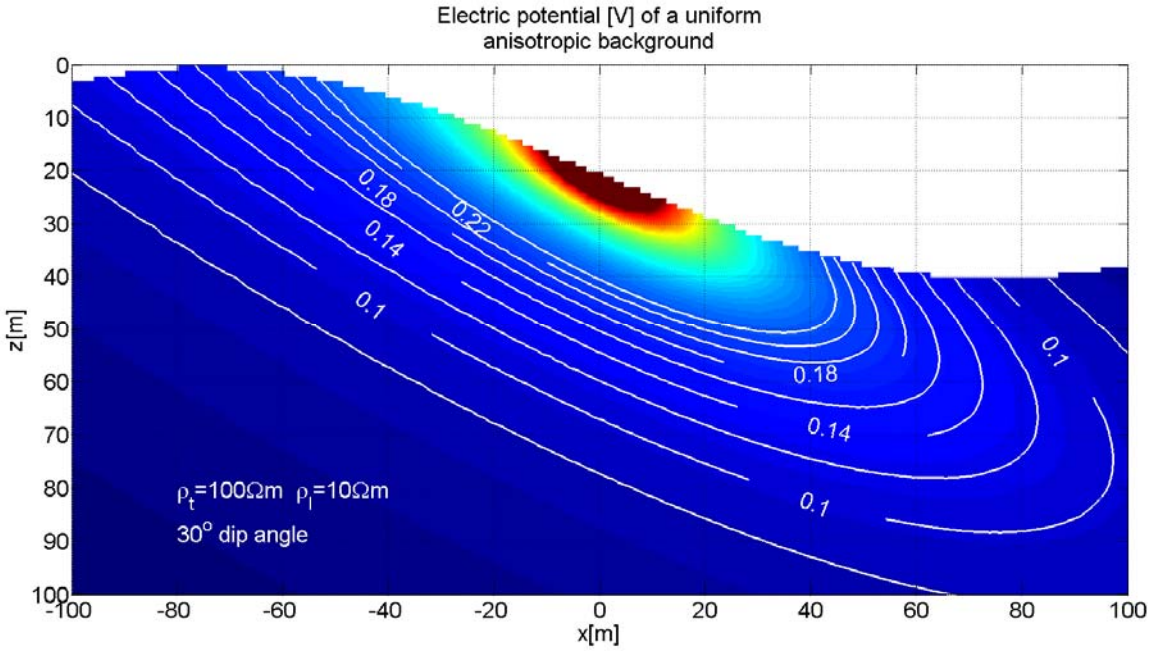

Figure 5.21 The GQG numerical solution for the subsurface potential in a uniform TTI medium with a sinusoidal surface topography.

Figure 5.22 is the conductor model $(\rho = 5\Omega m)$ embedded in the TTI background and having a sinusoidal topography. The image shows similar effects as those observed for the flat surface TTI conductor model (deeper current penetration below source), except we now see the topographic distortion like that seen in figure 5.21 for the homogeneous model. The surface plot comparison given in the top panel of figure 5.24 shows an increased asymmetry pattern with larger potentials to the left of the source for the conductor model and denoted by the symbol '*'. The computed voltage contours for the companion buried resistor model are displayed in figure 5.23. The diagram shows a shallower depth of current penetration and distortion of the contours in vicinity of the body from the otherwise parallel trend to the 30^0 dipping longitudinal resistivity axis. It is seen that in the resistor model however, the surface potentials are higher than the corresponding uniform model, and also higher to the left of the source. Finally, a graph of the potential difference between the uniform and conductor (blue) / resistor (green) TTI models is displayed in figure 5.24. Qualitatively, the embedded conductor TTI model potential difference has a positive skew while the embedded resistor TTI model potential difference has a negative skew. There is much less difference in

potential values between the resistor - uniform TTI valley model than the conductor – uniform TTI valley model.

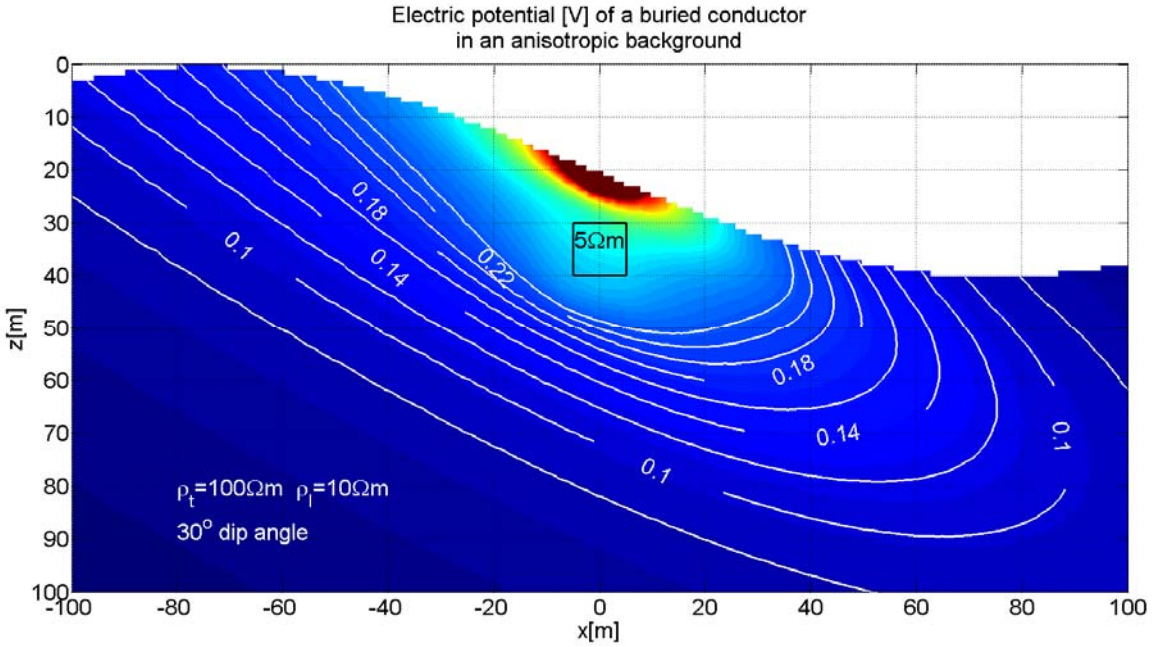

Figure 5.22 The GQG numerical solution for the subsurface potential in an inhomogeneous (buried conductor), TTI medium with a sinusoidal surface topography.

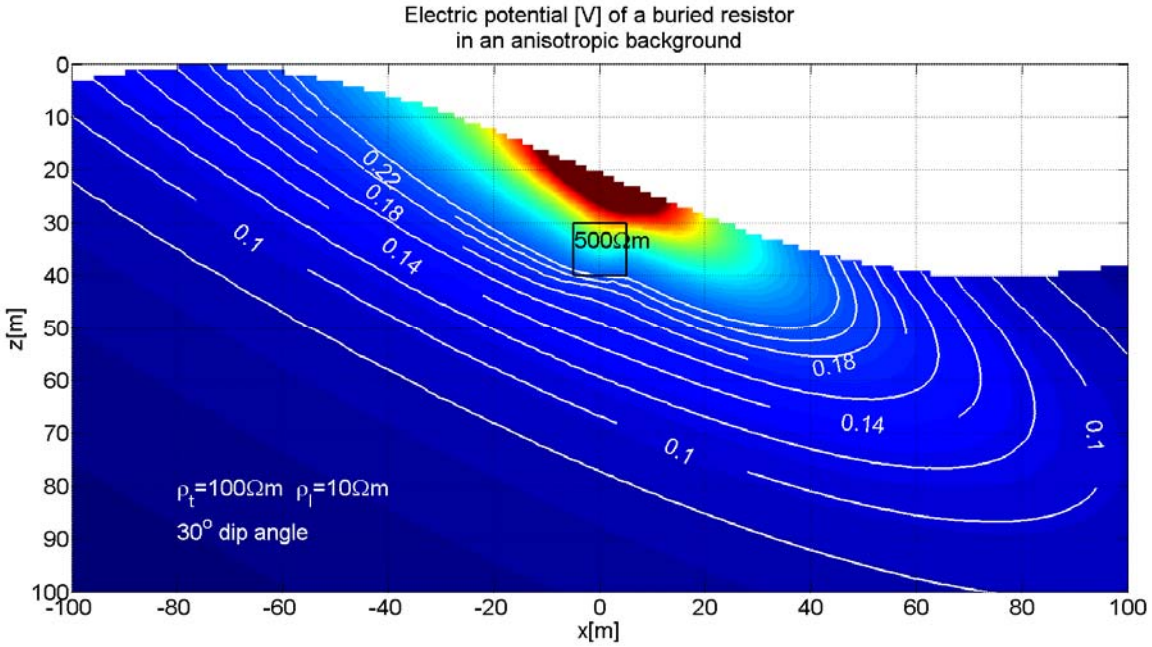

Figure 5.23 The GQG numerical solution for the subsurface potential in an inhomogeneous (buried resistor), TTI medium with a sinusoidal surface topography.

Also, the valley and hill topography appears to reduce the resistor - uniform TTI model difference in potential relative to the flat model significantly, whilst the topography appears to increase the difference in potential relative to the flat surface for the conductor – uniform TTI valley model.

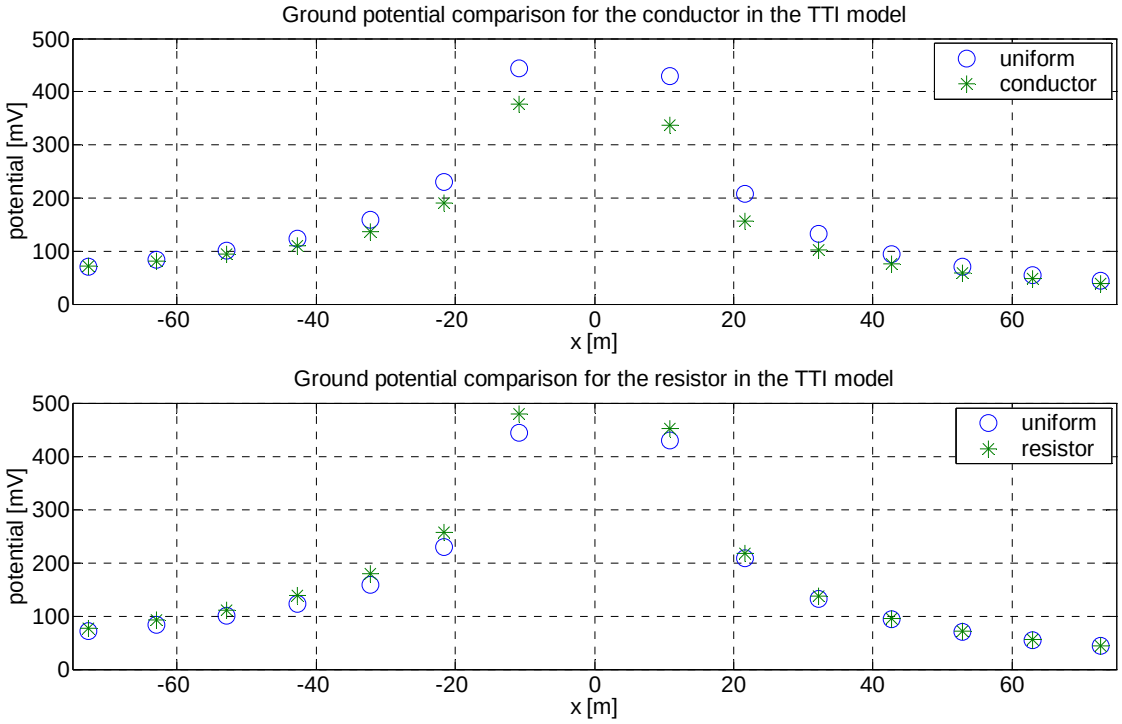

Figure 5.24 A comparison of the GQG surface potentials for the conductor and resistor models in a TTI medium with a sinusoidal surface (equivalent flat surface spacings denoted by 'x').

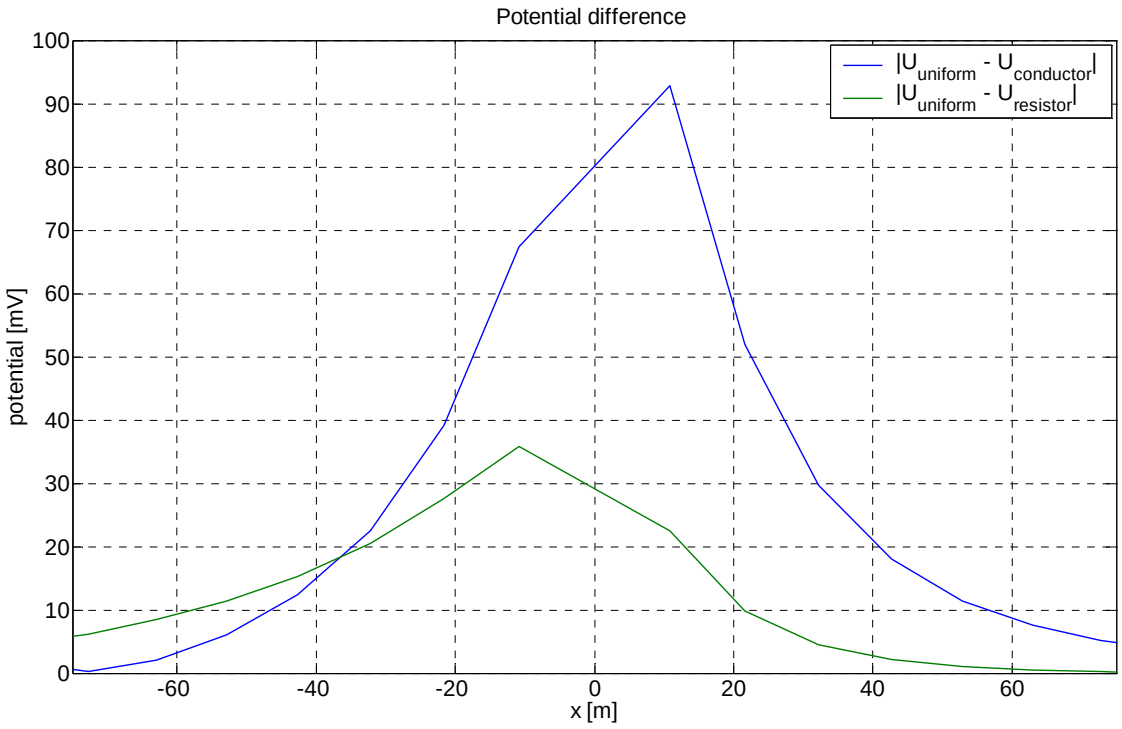

Figure 5.25 A comparison of the GQG surface potential differences for the conductor and resistor models in a TTI medium with a sinusoidal surface (equivalent flat surface spacings denoted 'x').

This kind of analysis is fairly empirical. In theory, the resistivity inversion problem is ill-posed and so by increasing the number of model parameters by incorporating topography and anisotropy (in addition to inhomogenieties) with fixed observables, (i.e. surface potential measurements and electrode geometric factors based on a flat surface assumption) it would be

extremely difficult to reconstruct any of the models presented thus far with present day recording procedures and smooth inversion techniques (see Herwanger *et al.*, 2004). In chapter 6, a theoretical framework for computing the Frechét derivatives and sensitivity patterns for TTI media is developed as an initial attack on this difficult problem.

Before introducing the 3-D modelling results, it is instructive to examine the capabilities of the GQG modelling approach for an extreme topography. Below in figures 5.26, 5.27 and 5.28 the same TTI medium as used previously, and incorporating the conductive and resistive anomalies, but now the current source is located at a surface boundary discontinuity. The topography is a sharp trench or cliff having a very steep side. The uniform TTI model image in figure 5.26 shows the correct elliptic equi-potential shape dipping at 30^0 parallel to the plane of isotropy (stratification). In the boundary region of $x \in [-45, 50]$ $z \in [70, 90]$ the contouring algorithm is unable to interpolate this region effectively. Apart from this artefact, the image looks satisfactory.

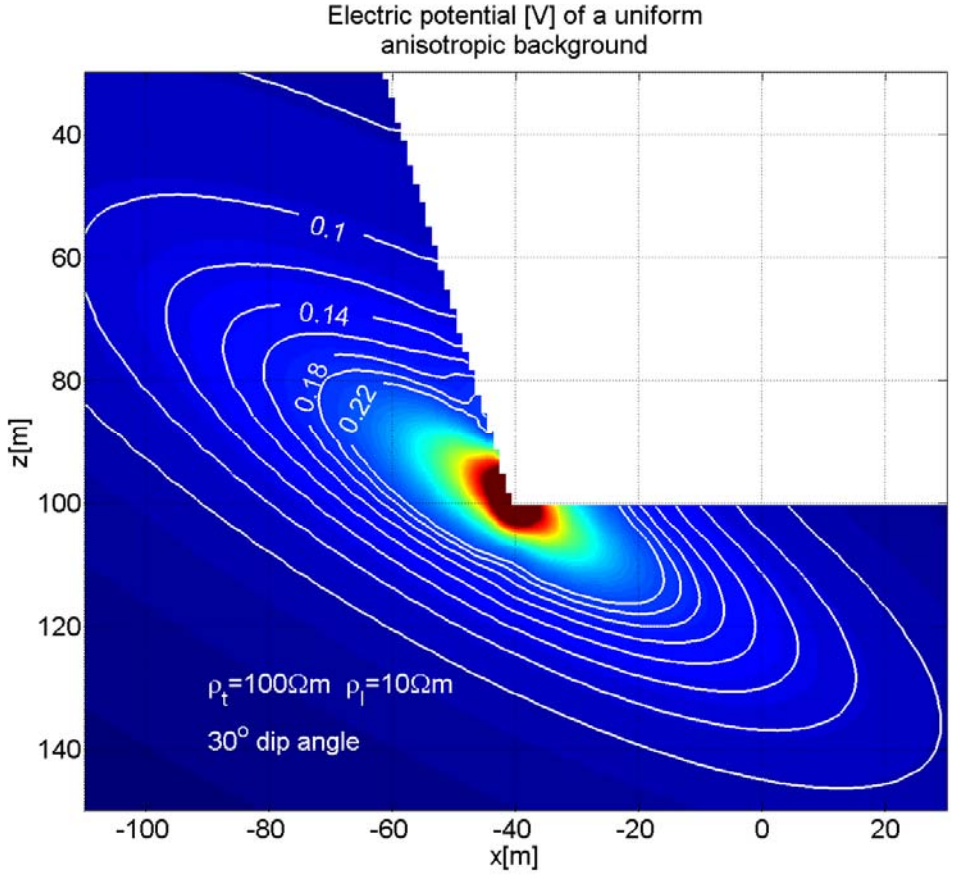

Figure 5.26 The GQG numerical solution for the subsurface potential in a uniform TTI medium for the trench topographic model.

The conductor and resistor models that follow in figure 5.27 and figure 5.28 respectively, have the anomalous body displaced 10 m deeper and 20 m to the right, i.e. at an angle of 20.55^0 from the source to the centre of the anomaly. The angle of the cliff from the horizontal is 15.95^0. The angle of dip of the anisotropy axis is again 30^0. Within the resistive anomaly (figure 5.28), the equipotentials are denser and much closer together which is due to the larger voltage drop in a resistor. Conversely, the equipotentials are much further apart in the conductive anomaly (figure 5.27) reflecting the lower voltage drop over a comparable distance in a conductor.

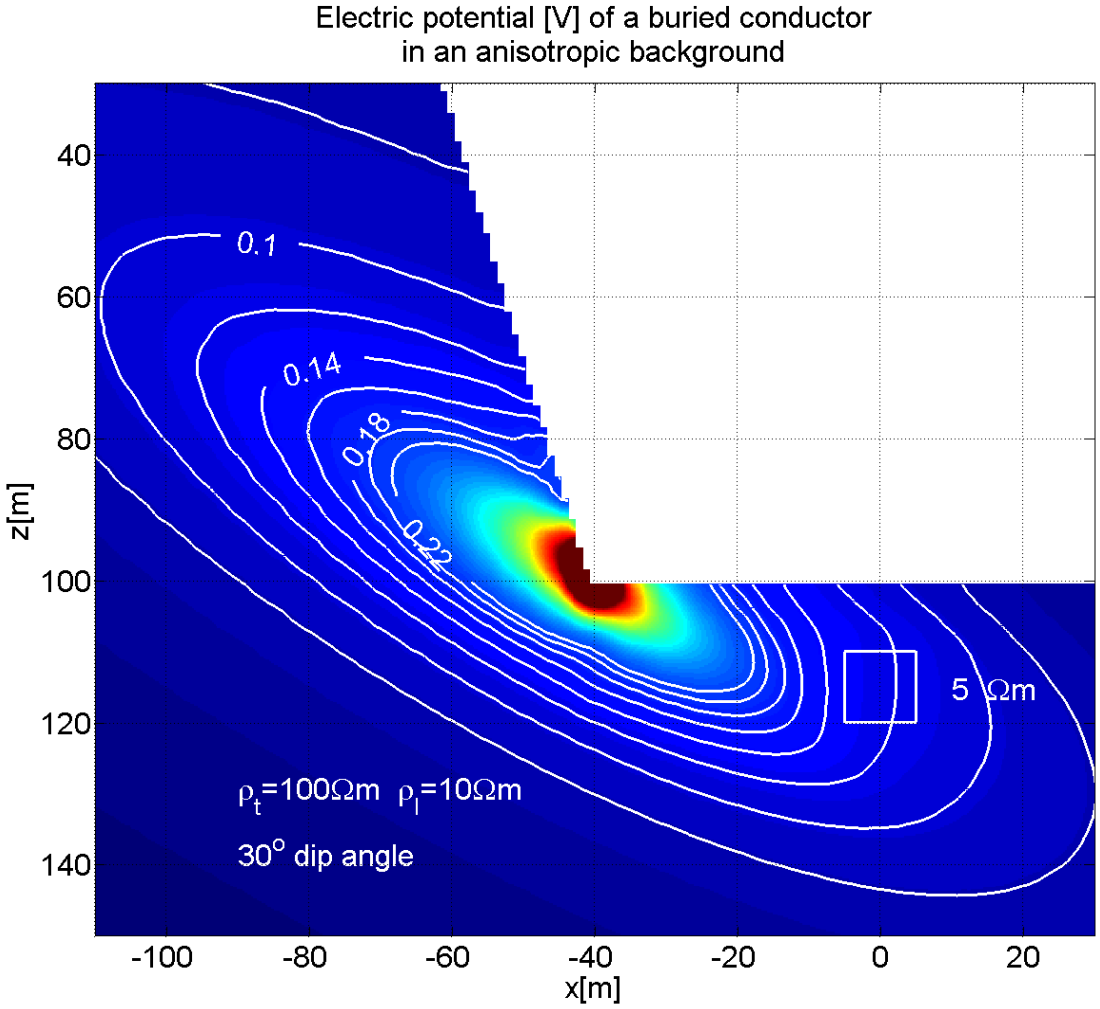

Figure 5.27 The GQG numerical solution for the subsurface potential in an inhomogeneous (buried conductor in the middle of the trench model longitude), TTI medium.

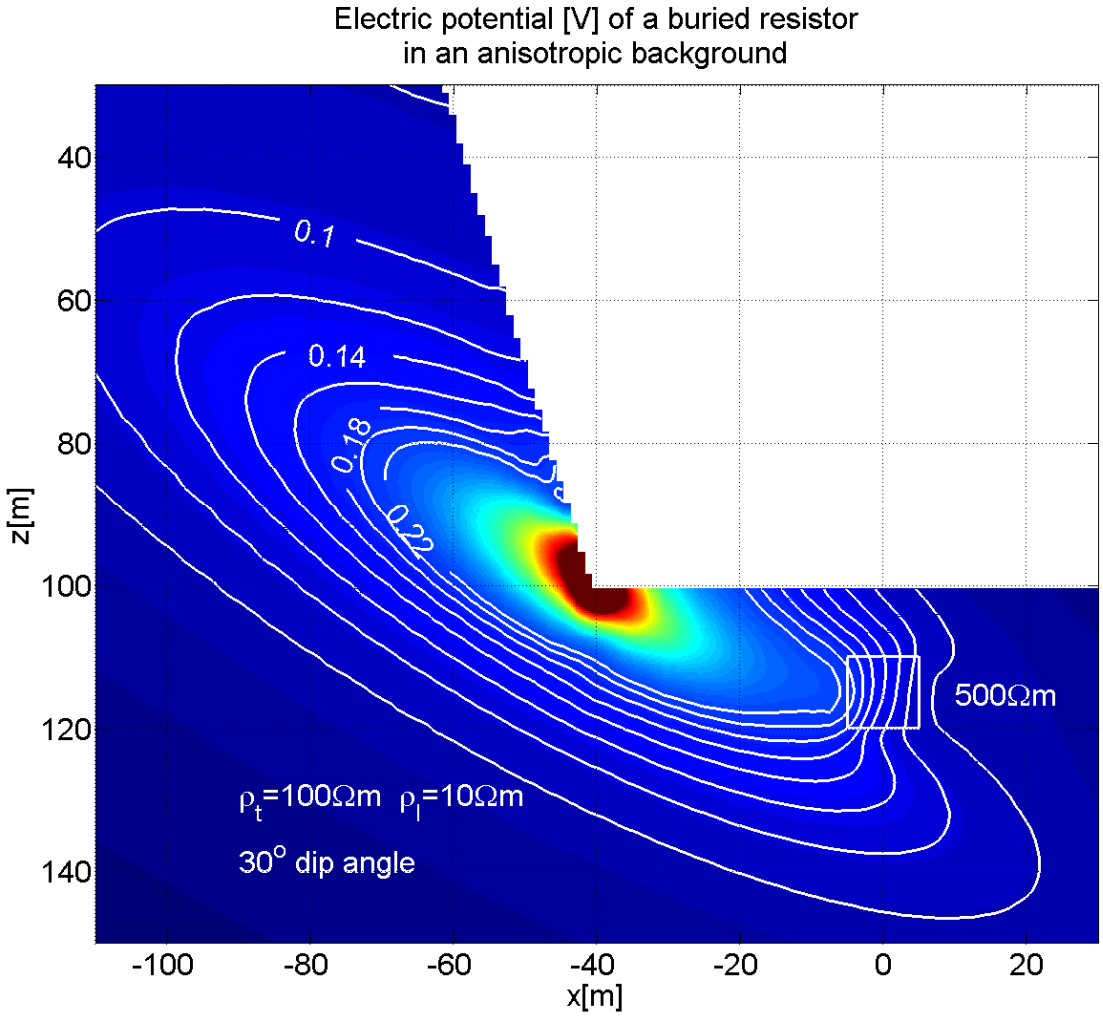

Figure 5.28 The GQG numerical solution for the subsurface potential in an inhomogeneous (buried resistor in the middle of the trench model longitude), TTI medium.

5.6 3-D Isotropic Homogeneous Model with Topography

The 3-D resistivity modelling over an irregular topographic boundary will now be investigated. The topography chosen features two hills and adjacent low lying areas or valleys (see figure 5.30). Firstly an isotropic homogeneous subsurface having resistivity $\rho = 10\Omega m$ and with a current source of unit strength at the origin (centre) was modelled with

the GQG method. This yielded voltage values at all points within and on the surface of the 3-D model. Two orthogonal lines of potential electrodes, denoted A and B and situated along the inflection (saddle point) lines, are shown in figure 5.31. For comparison purposes the same 3-D model was also investigated at my request by Mark Blome of ETH Zurich (Swiss Federal Institute of Technology), who has developed some powerful and flexible numerical resistivity modelling code. He generated results using the boundary element method (BEM) using the mesh in figure 5.30, and the two FEMs using the mesh shown in figure 5.29. The calculated surface potential solution is displayed in figure 5.31. The two FEMs are linear and quadratic shape functions, i.e. 10 instead of 4 nodes per tetrahedron. A Robin (mixed) type boundary condition was used in the FEM models. He also used a local refinement in the triangulation about these electrodes.

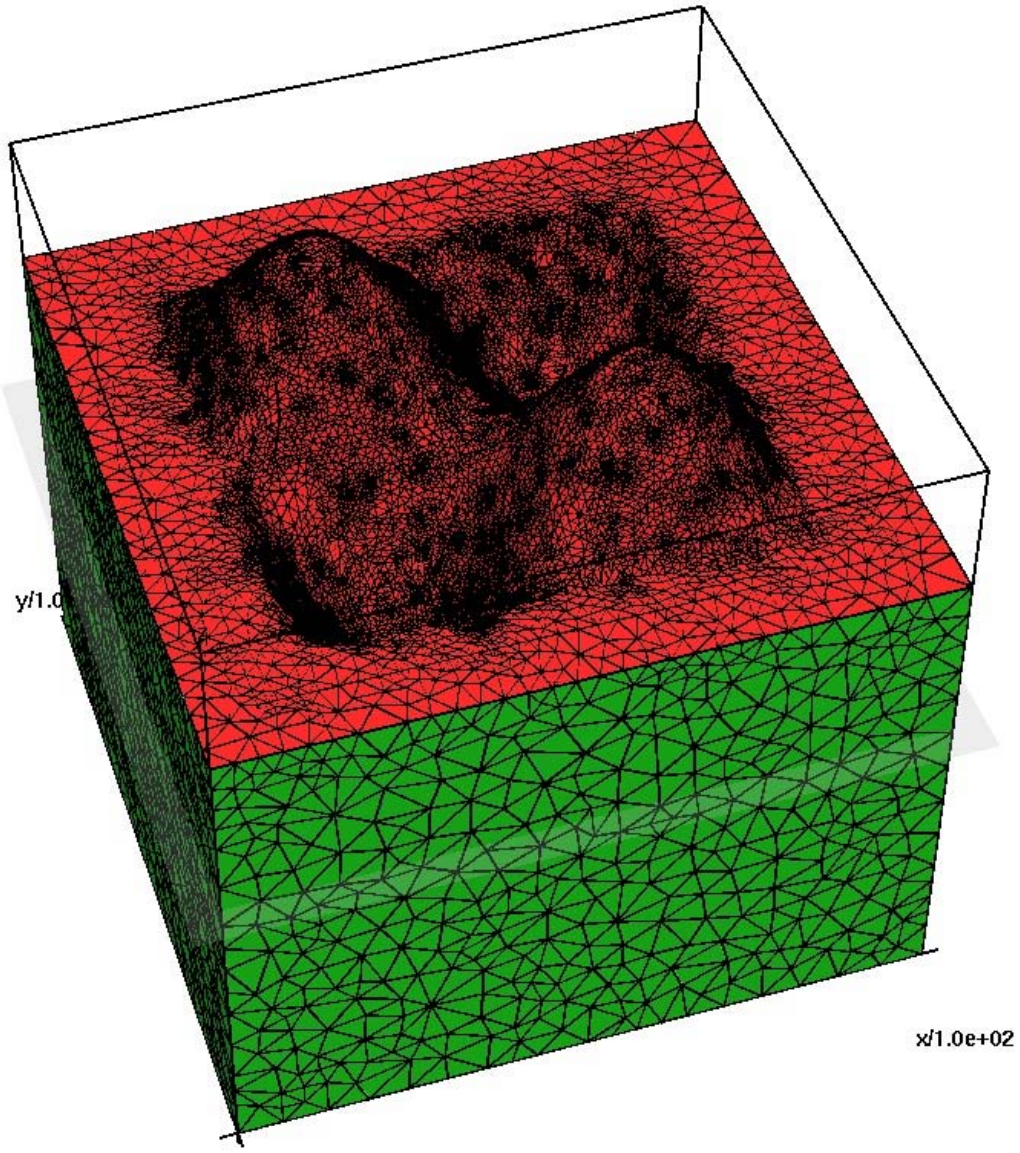

Figure 5.29 The FEM mesh with local refinement around the current electrode, used for comparison with the 3-D GQG. (Courtesy of Mark Blome, ETH Zurich)

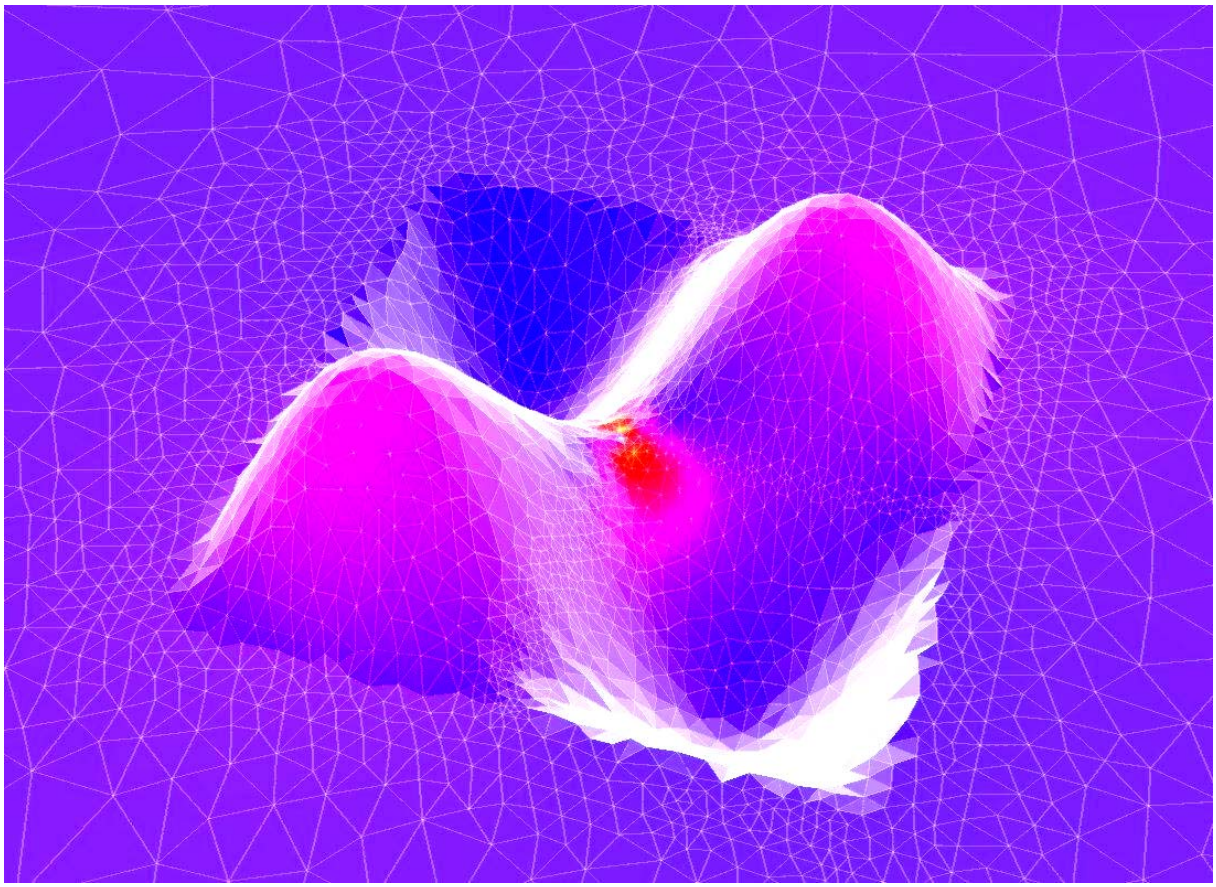

Figure 5.30 The BEM surface mesh and potential image for the 3-D uniform isotropic media with topography. (Courtesy of Mark Blome, ETH Zurich)

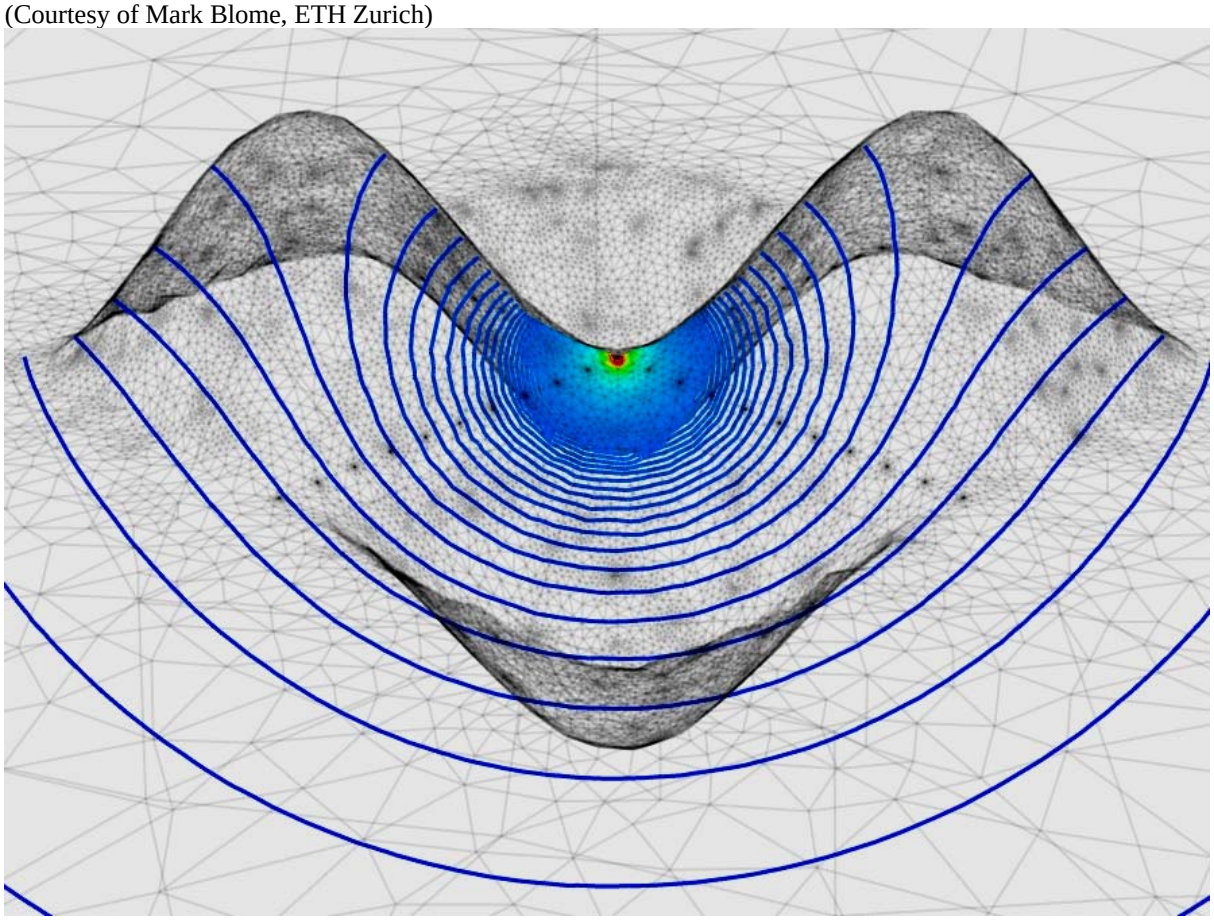

Figure 5.31 The FEM surface mesh and potential image for the 3-D uniform isotropic media with topography. (Courtesy of Mark Blome, ETH Zurich)

This specific topography is quite unique and good for testing the GQG code. The current electrode and the potential electrodes are strategically placed to nullify the topographic effect. The assertion is that the surface potential measured along these profiles should be symmetric about the source. Additionally, it is also evident that the potential should be exactly the same regardless of which orientation it is measured, i.e. lines A and B should yield the same electric potential profile. This is true for the GQG, so the surface potentials are displayed in figure 5.32 for only line A to show the GQG performance against the BEM and two FEMs. The GQG solution matches the other well established methods considerably well. In addition, the GQG is the only method of these four that has a symmetric potential profile for this specific topography.

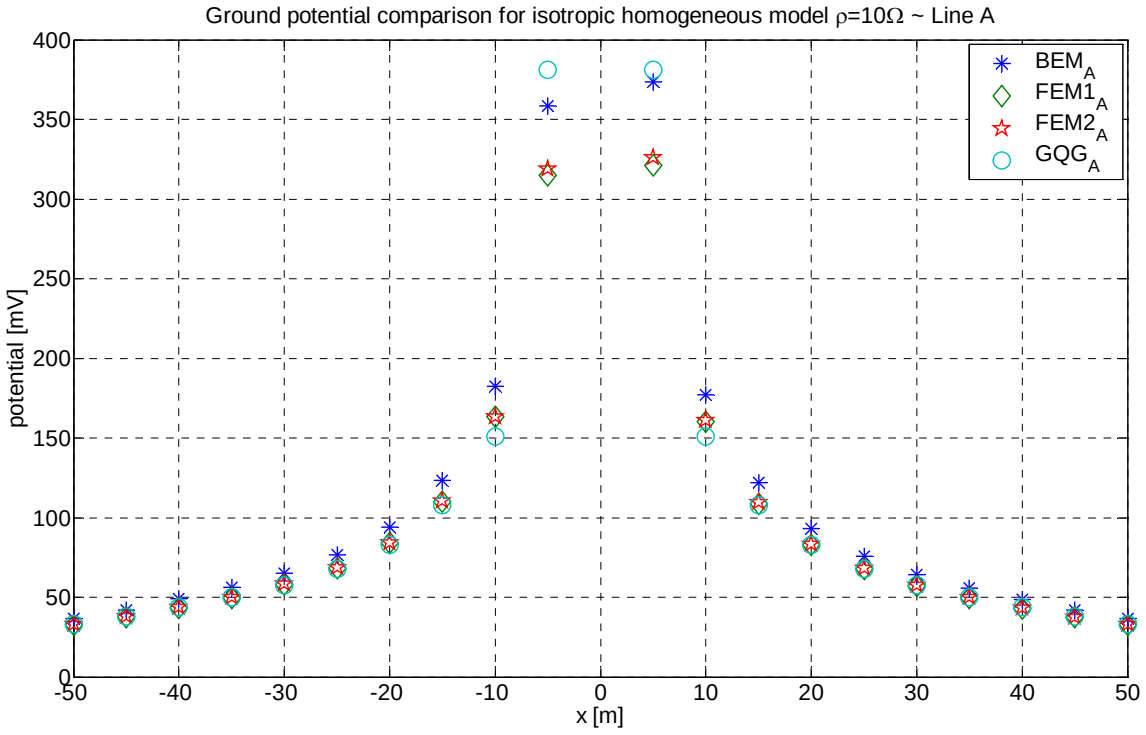

Figure 5.32 The FEM solution for surface potential overlayed on the mesh (tetgen), used for comparison with the 3-D GQG.

Observe in figure 5.30 how the tetrahedrons approximate the square surface boundary. The four horizontal / vertical plane interfaces at the surface have dissimilar approximations as a result of the triangulation. This could explain the slight asymmetry of BEMs' and FEM(s)' potential curves. Figure 5.33 shows the individual comparisons. For completeness, the BEM and FEMs transpose survey lines A and B are plotted in figure 5.34 to show the other slight asymmetry for this special topography.

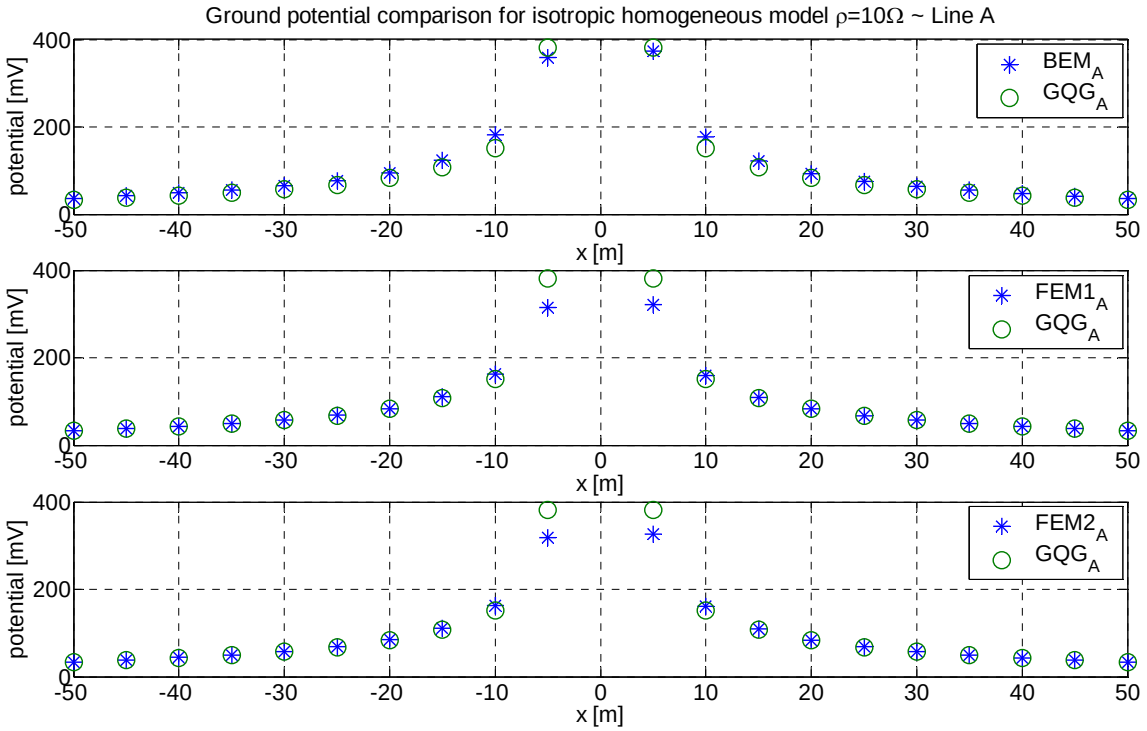

Figure 5.33 Individual survey line A potential curve comparisons.

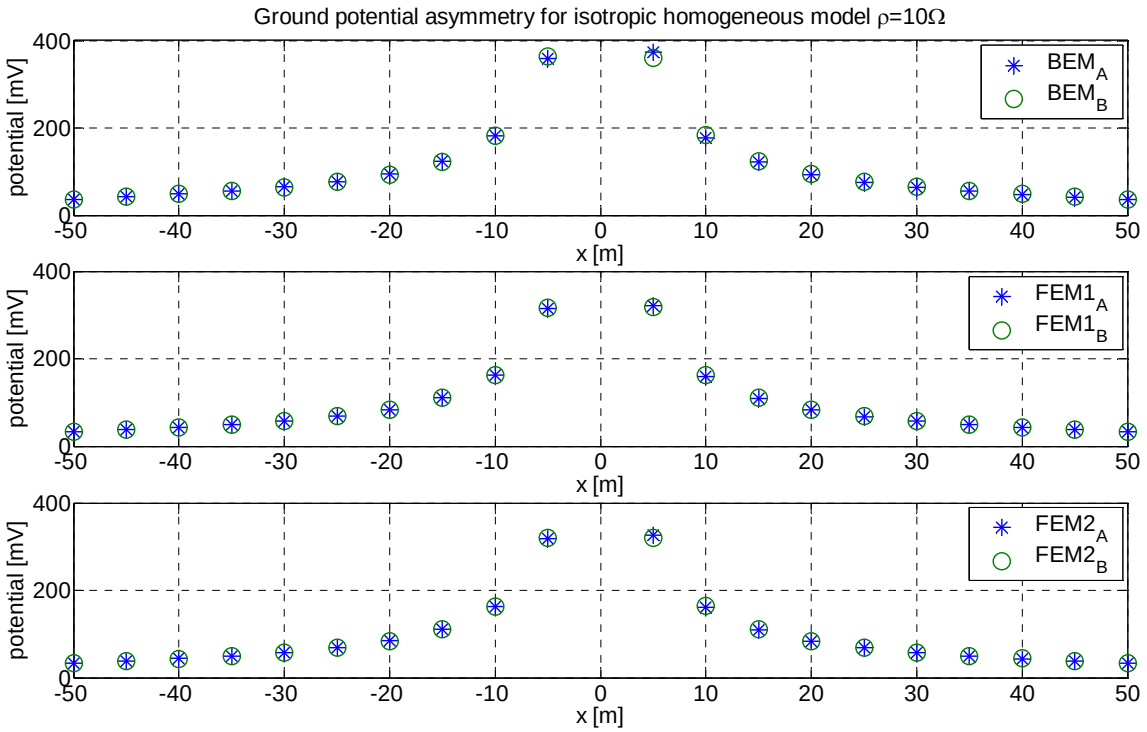

Figure 5.34 Survey lines A and B of BEM, FEM1 and FEM2 are compared for equivalence.

5.7 3D Anisotropic Homogeneous Model with Topography

Figure 5.35 shows two examples of 3-D homogenous anisotropic modelling ($\rho_{x'x'} = \rho_{y'y'} = 5$ Ωm, $\rho_{z'z'} = 10$ Ωm, $\theta_0 = 45^\circ$, $\varphi_0 = 0^\circ$). One has a flat surface so that it has an analytic solution for comparison. The other is the same as the previous example i.e. two hills and adjacent low lying areas. We have plotted in figure 5.35 the electric potential contour sections in the subsurface obtained from GQG modelling and the voltage profiles obtained for the two orthogonal surface lines shown in the model and labelled A and B.

For the flat surface model the potential curves on the surface are symmetric to the source point in terms of the analytic solution (equation 4.14). From the left panel of figure 5.35, we observe excellent agreement between the GQG modelling and the analytic solutions. From the 3-D topographic result (right panel in figure 5.35), one can see the potential curves are no longer symmetric. This change implies a coupled anisotropy - topography effect. The potential profiles are no longer symmetric and equal when both complexities are included. **The results in this chapter demonstrate the versatility and accuracy of the GQG method.**

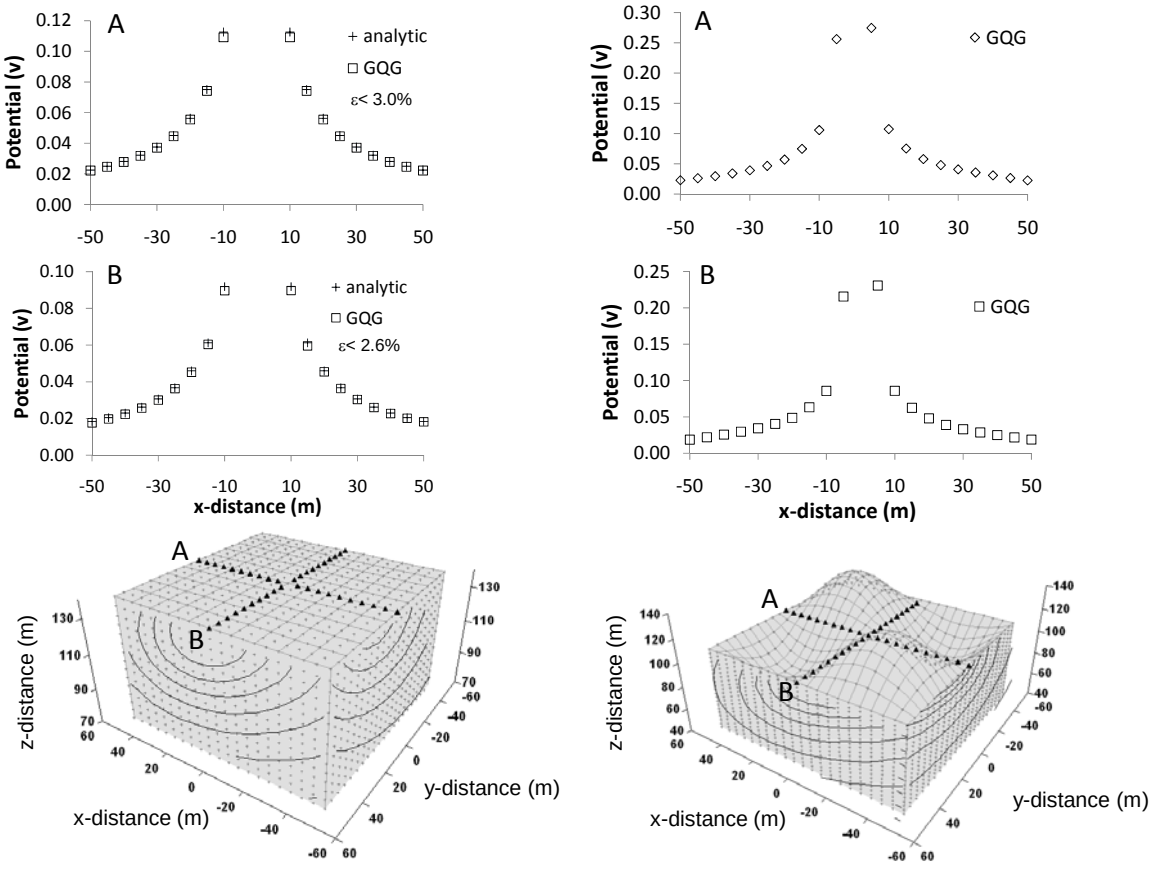

Figure 5.35 The analytic and GQG solutions for surface potential on exotic topography for uniform TTI media.